Dynamic Stress Wave Propagation

by

Dustin Pearson

Submitted in partial fulfilment of the requirements
for the degree of Master of Applied Science

at

Dalhousie University
Halifax, Nova Scotia
August 2016

DEDICATION PAGE

I would like to dedicate this thesis to my wife, Taylor Comeau for her love and support.

TABLE OF CONTENTS

LIST OF FIGURES

LIST OF TABLES

ABSTRACT

In an effort to provide an analyst with the fundamental knowledge required to successfully predict dynamic structural response, a detailed summary of dynamic stresses, review of dynamic pulse buckling and verified numerical examples are provided. The dynamic stress wave characteristics described herein, including strain-rate sensitivity, are reviewed within the literature with respect to dynamic pulse buckling. Many numerical studies within the literature utilize experimental studies to verify their approach to the dynamic pulse buckling problem. Several of the experimental studies utilized in the literature, were numerically analyzed herein and post-processed to provide a detailed investigation of stress wave propagation characteristics in impact problems of simple structures. The characteristics of stress wave propagation within a complex (ship double bottom) structure were investigated numerically. Several variations were observed between stress wave propagation within simple and complex plated structures.

LIST OF ABBREVIATIONS AND SYMBOLS USED

3D	Three dimensional
DLF	Dynamic Load Factor
EOS	Equation of State
FE	Finite element
a	Acceleration
A	Area
C_0	Longitudinal stress/sound wave speed
C_s	Shear stress/sound wave speed
E	Young's modulus
E_h	Hardening modulus
E_n	Energy
F	Force
L	Length
m	Mass
P	Pressure
P_0	Initial pressure
R	Radius
t	Time
T_s	Load pulse duration
T_p	Fundamental period of vibration
U_s	Shock front velocity
U_p	Particle velocity
ρ	Density
ρ_0	Initial density
ε	Strain
σ	Stress
σ_y	Static yield stress
σ_{yd}	Dynamic yield stress
ν	Poisson's ratio
μ	Lamé constant
$\dot{\varepsilon}$	Strain rate

ACKNOWLEDGEMENTS

I would like to thank my supervisor, Farid Taheri for his technical, professional and personal guidance throughout the years as a professor, mentor and friend.

CHAPTER 1 INTRODUCTION

Marine and offshore structures are complex systems subject to dynamic and extreme loading environments. The level of dynamic or extreme loading is specific to the platform or ship type, as a design requirement or accidental limit state. Some examples of extreme loads include: wave slamming, ship-platform impact, ice impact, air blast and underwater explosions, as well as hurricane force wind and wave loads. Although operational safety procedures and international design requirements are implemented to reduce the level of damage, and increase the likelihood of surviving such events, accidents occur causing structural damage. The level of damage is a function of the ship or platform type, structural configuration and loading event. Predicting the dynamic response of marine and offshore structures under dynamic loading events requires a broad knowledge specific to each structure type and loading environment. A common factor shared by structures is the behavior and response of the material undergoing the dynamic loading event.

Some dynamic structural problems are commonly analyzed as an equivalent static problem. This is an adequate simplification when considering the modal response of the structure and quasi-static material characteristics. For dynamic structural problems governed by the stress wave propagation behavior and strain-rate sensitivity, the structural dynamics cannot be simplified. Accordingly, an understanding of dynamic stress and its application to structural stability, particularly under dynamic pulse buckling conditions are essential for analysts to properly determine structural response.

A detailed summary of dynamic stresses, together with a review of dynamic pulse buckling and few verified numerical examples are provided in an effort to provide an analyst with the fundamental knowledge required to predict dynamic structural response. Stress wave propagation and its influence on structural response of simple examples are discussed in Chapters 2 and 3. The numerical examples in Chapter 4 provide a review of stress wave propagation to better explain the concepts discussed in the theory and literature.

The dynamic behavior of ductile materials was reviewed to investigate the influence it may have on material dynamic stress, how stresses propagate, and how to empirically predict the behavior of a particular material under dynamic loading conditions.

Dynamic structural response governed by the dynamic material behaviour cannot be simplified as an equivalent static problem. The analyst is required to understand the dynamic stress characteristics and their influence on structural stability. This includes the understanding and proper representation of dynamic stress wave propagation behaviour, strain rate sensitivity, geometric and loading imperfections, stability criteria and physical mechanics (momentum and kinetic energy) of the problem.

CHAPTER 2 BACKGROUND

Evaluating the response of a structure subject to dynamic loading events is a complex problem with additional challenges specific to the loading environment. A commonality amongst dynamic problems is the material stress wave behavior. Stress wave propagation characteristics are directly related to the medium material properties. The following sections discuss stress wave propagation in detail in addition to the material testing methodology required to determine the material characteristics.

The ability of a material to resist dynamic loads is shown to be characterized by the dynamic yield strength of the material. The dynamic yield strength is a function of the material strain rate sensitivity. Materials that exhibit a high sensitivity to strain rate have correspondingly higher dynamic yield strengths than the quasi-static yield strength. The strain rate sensitivity of a material can be determined at various loading rates can be studied using a number of techniques that include: the Split Hopkinson Bar [42], Taylor [79] and Flyer Plate [25] tests.

Elastic stress wave mechanics are implemented during the Split Hopkinson Bar test to extract the stress, strain and strain rate time functions for strain rates between 10^2-10^4 s^{-1}. For strain rate sensitivities at rates above 10^4 s^{-1} and high plastic strain levels, the Taylor test is implemented. To determine the equation of state (EOS) of a material in a shocked state and the spallation stress, the Flyer Plate test is used. Such experimental tests may be used to determine the material characteristics at high strain rates and based on the resulting material characteristics, the suitability of a tested material may be determined for a particular application.

Once its characteristics are known, the dynamic yield strength of the material at various strain rates may then be approximated using a constitutive equation. The Cowper-Symonds [19] and Johnson-Cook [33] constitutive equations are presented to provide examples of simple (Cowper-Symonds) and relatively complicated (Johnson-Cook) equations. The application of either equation depends on the available material

parameters and analysis requirements. The Johnson-Cook equation requires more material parameters than Cowper-Symonds; however, it accounts for and is sensitive to the instantaneous stress, strain rate and temperature. The Cowper-Symonds equation requires two material parameters and does not account for temperature.

The response of an unknown material to dynamic loads may be empirically estimated by determining the dynamic yield strength experimentally or by approximating the stress-strain behavior using a constitutive equation. The experimental test must be chosen to reflect the strain rates expected during the dynamic loading application. The experimental testing procedure, stress wave mechanics and post processing calculations have been presented for strain rates above $10^2\ s^{-1}$.

2.1 Stress Wave Propagation

A review of ductile material dynamic behavior has been conducted to investigate the influencing factors on material dynamic strength, stress propagation behavior and empirical prediction methods for a particular material under dynamic loading conditions. To understand the dynamic stress propagation within a material, the general characteristics of elastic, plastic and shock waves are discussed. Specifically, the stress wave interaction and specific material properties that govern the elastic, plastic and shock stress wave propagation are investigated. More specifically, the material sonic impedance, strain rate sensitivity, dynamic yield strength, Hugoniot [69], shock impedance, spallation and Equation of State (EOS) are presented.

Experimental tests were developed to characterize the material response to each dynamic stress wave type. The material response to elastic stress waves is evaluated using the Split Hopkinson Bar test, and for the plastic stress wave response, the experimental Taylor test is applied. To evaluate the material shock impedance, Hugoniot and EOS of shock waves, the Flyer Plate Test is used.

The stress wave, corresponding material characteristics and experimental tests are presented in order of stress wave magnitude, following a brief description of dynamic stress. The elastic stress wave propagation and interaction characteristics, strain rate sensitivity, dynamic yield strength and Split Hopkinson Bar test are presented first. Constitutive equations follow the elastic stress waves to expand on strain rate effects. Thirdly, the plastic stress wave propagation characteristics, Taylor test and its corresponding calculations are discussed and finally shock stress wave propagation and interaction as well as shock wave material characteristics are explained.

2.2 DYNAMIC STRESS

The response of a material to a particular loading is a function of the material characteristics and the specific loading application. In general, a structure may be loaded statically or dynamically. The characteristics of the stress state developed from a static load are different from a dynamic load. If the loading is considered static, the unit cube in static equilibrium in Figure 1 is used to present the stresses on each face. For each stress σ_{ij}, i is the axis of stress, and j is the direction of stress normal to i. For the unit cube under directional forces F_1, F_2 and F_3 in static equilibrium, the three-dimensional stress state is expressed as:

$$\frac{\partial \sigma_{x_1}}{\partial x_1} + \frac{\partial \tau_{x_{12}}}{\partial x_2} + \frac{\partial \tau_{x_{13}}}{\partial x_3} + F_{x_1} = 0$$
$$\frac{\partial \sigma_{x_2}}{\partial x_2} + \frac{\partial \tau_{x_{12}}}{\partial x_1} + \frac{\partial \tau_{x_{23}}}{\partial x_3} + F_{x_2} = 0$$
$$\frac{\partial \sigma_{x_3}}{\partial x_3} + \frac{\partial \tau_{x_{13}}}{\partial x_1} + \frac{\partial \tau_{x_{12}}}{\partial x_2} + F_{x_3} = 0 \qquad [1]$$

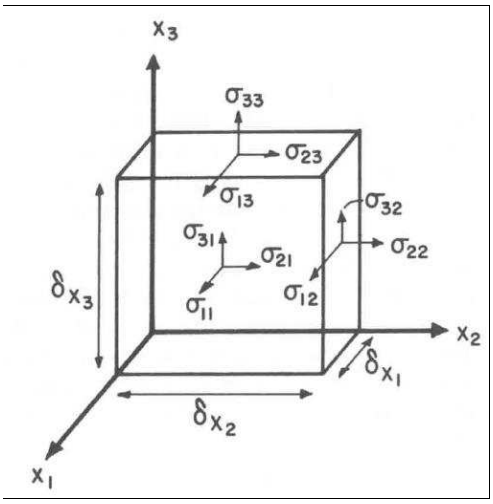

Figure 1 Unit stress cube at static equilibrium (reproduced from [57]).

The details of elastic, plastic and shock wave dynamic stress wave propagation characteristics are explained in the sections to follow. A detailed derivation of the dynamic unit stress equations are provided in Meyers [57]. For the general dynamic stress discussion, it is important to understand that a dynamic stress has a direction and velocity with varying stress amplitude with time. The unit cube of a dynamic stress state in Figure 2 presents the stresses propagating from the origin along X_1. The cube is in a dynamic state. The stresses acting on opposite faces are not equal and one must account for the variation in stresses across a small parallelepiped with the sides parallel with coordinate system displayed in Figure 2. The normal stresses in Figure 2, similar to Figure 1 are presented as σ_{11} and shear stresses σ_{12} and σ_{13}. The stress components on each face, expressed in tensorial notation, of the dynamic unit stress cube are:

$$\sigma_{ij} \pm \frac{\partial \sigma_{ij}}{\partial x_j} \cdot \tfrac{1}{2}\delta x_j \qquad [2]$$

where $\pm \frac{\partial \sigma_{ij}}{\partial x_j} \cdot \tfrac{1}{2}\delta x_j$ is the change in σ_{ij} as one moves from the cube origin O, to a face perpendicular to $OX1$. From Newton's second law, the force on each face of the unit cube can be expressed as a function of cube mass (m) and directional acceleration (a_i):

$$F_{x1} = ma_1 \quad F_{x2} = ma_2 \quad F_{x3} = ma_3 \qquad [3]$$

Or if we consider a single direction along X_1:

$$\sum F_{x1} = (\rho \, dx_1 dx_2 dx_3) \frac{\partial^2 u_1}{\partial t^2} \qquad [4]$$

where $\frac{\partial^2 u_1}{\partial t^2} = \frac{E}{\rho}\frac{\partial^2 u_1}{\partial x^2}$, is the differential equation for the stress wave; a function of strain, $\frac{\partial u}{\partial x}$.

If one considers the resultant forces acting on the faces in the direction of X1 as the stress acting on a face multiplied by the area of the face, the expressions to calculate the forces on each face of the dynamic cube are:

$$\frac{\partial \sigma_{11}}{\partial x_1} + \frac{\partial \sigma_{12}}{\partial x_2} + \frac{\partial \sigma_{13}}{\partial x_3} = \rho \frac{\partial^2 u_1}{\partial t^2}$$

$$\frac{\partial \sigma_{21}}{\partial x_1} + \frac{\partial \sigma_{22}}{\partial x_2} + \frac{\partial \sigma_{23}}{\partial x_3} = \rho \frac{\partial^2 u_2}{\partial t^2}$$

$$\frac{\partial \sigma_{31}}{\partial x_1} + \frac{\partial \sigma_{32}}{\partial x_2} + \frac{\partial \sigma_{33}}{\partial x_3} = \rho \frac{\partial^2 u_3}{\partial t^2} \qquad [5]$$

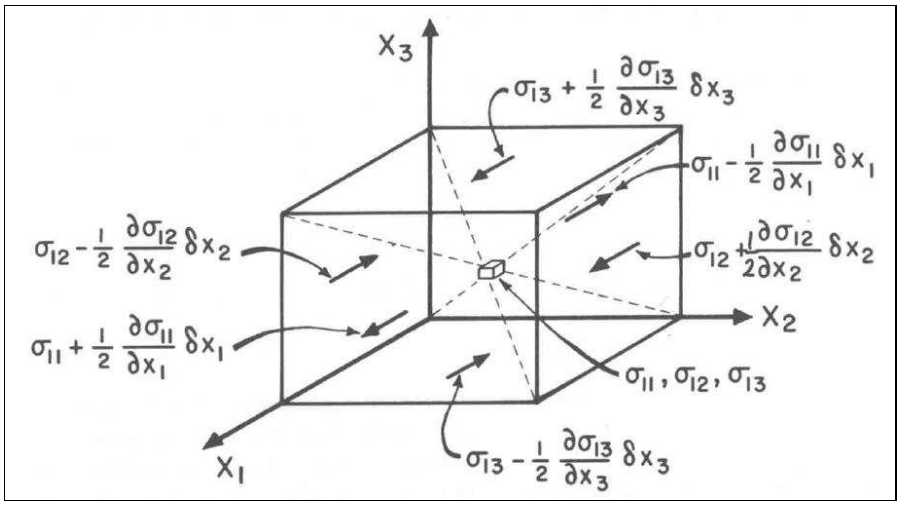

Figure 2 Unit dynamic stress cube (reproduced from [57]).

When a structure is loaded dynamically, the induced stresses travel through the structural material in the form of a wave, analogous to the transfer of momentum and kinetic energy between colliding billiard balls. An example of a dynamic load is an explosive shock wave hitting a vessel or a hammer striking a plate or bar. The induced stress wave propagation can be broken down and illustrated atomically. The stress wave propagates through an atom interaction by transferring the stress amplitude to the neighbouring atoms and then onto the next and so forth as the stress wave propagates throughout the continuum. From mechanics of materials, one understands that depending on the stress

level and the material characteristics, a material may deform elastically or plastically. Once the amplitude of a stress wave exceeds the elastic limit, the wave will decompose into an elastic and plastic wave. At high loading rates, shock or projectile impact loading for example, stress shock waves propagate through the material. The stress wave characteristics, material properties that govern the stress wave propagation, and experimental tests to determine material behaviour at specific loading rates are discussed in the following sections.

2.3 Elastic Stress Wave

The behaviour of dynamic stress waves propagating through a continuum are a function of the stress amplitude and may be elastic or plastic. An elastic stress wave is developed when the induced stress amplitude is below the dynamic yield stress. The dynamic yield stress, similar to the static yield stress, is material dependent. In order to predict the dynamic response of a structure, it is important to determine the dynamic yield strength of a material for a given loading application. Commonly, the Split Hopkinson Bar test is used to determine the dynamic yield strength of materials. In order to understand the mechanics of the Split Hopkinson Bar test, one must first understand the mechanics of an elastic stress wave; more specifically, the elastic wave types, wave velocity, wave interaction and strain rate sensitivity. To conclude this section, the Split Hopkinson Bar test and the test post-processing calculations will be presented.

2.3.1 Elastic Stress Wave Types

There are different elastic wave types. The type of wave depends on the solid particle motion relative to the stress wave propagation direction and associated boundary conditions. The different types of elastic waves include [57]:

1. Longitudinal or dilatational waves.
2. Distortional or shear/transverse waves.
3. Surface or Rayleigh waves.
4. Interfacial or Stoneley waves.
5. Bending or flexural waves.

Each wave type is characterized by the particle motion in the solid with respect to the direction of the propagating stress wave. Longitudinal stress wave particle motion is in the direction of wave propagation with particle velocity (U_p) parallel to the wave velocity (U). The compressive or tensile particle velocity directionality is a function of the stress amplitude in the material. That is if the stress wave is compressive the particle velocity is in the direction of the stress. If the stress wave is tensile, the particle velocity opposes the direction of the tensile stress wave. This effect will be revisited during the stress wave interaction discussion. An example of a longitudinal stress wave is provided in Figure 3. The slender bar is struck with a hammer and the compressive longitudinal stress wave travels from left to right as the particle momentum and energy is transferred from left to right as well.

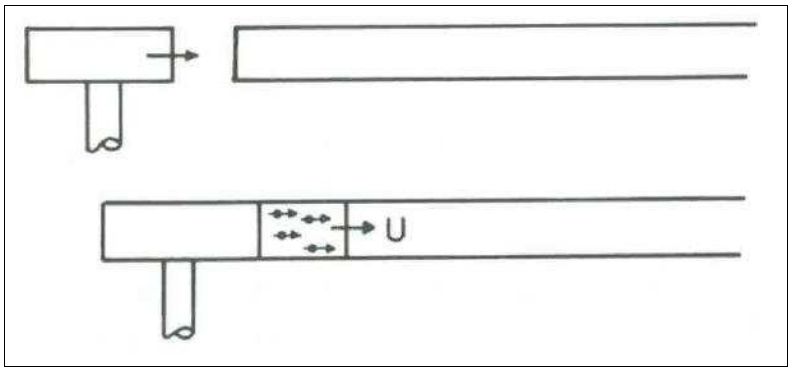

Figure 3 Hammer striking bar (top), longitudinal stress wave with velocity (U) (bottom) (reproduced from [57]).

The example of a hammer striking an infinitely thick plate in Figure 4 illustrates the different dynamic stress waves propagating from an impact load. The particle motions of a distortional/shear wave are perpendicular to the stress wave direction of travel. The density of the material does not change and the longitudinal or normal strains (ε_{11}, ε_{22}, ε_{33}) are zero for distortional/shear stress waves. The particle motion of surface/Rayleigh waves is similar to the motion of a small object floating on a water surface. As the wave propagates past the object, the object/particle moves in an elliptical pattern (up and down, back and forth). The Rayleigh wave shown in Figure 4 is in the surface region close to the struck area with an exponentially decaying particle velocity. Rayleigh waves are the slowest of the three waves and decay exponentially as they

propagate away from the source. Interfacial or Stoneley waves are unique waves that form at the interface of two semi-infinite media with different material properties during contact. The propagation of a flexural wave normally occurs in bars or plates.

The longitudinal waves are the fastest of the three waves with a varying decay rate similar to shear waves. At the plate surface, the longitudinal and distortional waves decay at a rate of $\frac{1}{r^2}$ and $\frac{1}{r}$, respectively, away from the free surface. The radial distance *r* from the impact is the distance to the stress wave peak amplitude.

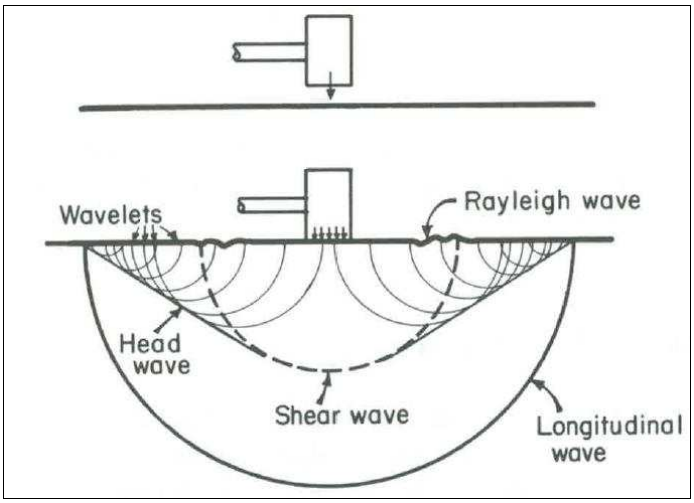

Figure 4 Hammer striking infinitely thick plate with wave formations displayed (reproduced from [57]).

The velocity of the elastic stress wave is a function of the material characteristics and the shape of impacted media. For elastic waves propagating in a continuum, the longitudinal wave velocity C_l is expressed as:

$$C_l = \left[\frac{\lambda+2\mu}{\rho}\right]^{\frac{1}{2}} \quad [6]$$

where ρ is the continuum density and from elastic theory, λ and μ are the Lamé constants, expanded as:

$$\lambda = \frac{\nu E}{[(1+\nu)(1-2\nu)]} \text{ and } \mu = \frac{E}{[2(1+\nu)]} \quad [7]$$

where E and ν are the Young's modulus and Poisson's ratio, respectively.

For an elastic wave traveling through a thin bar with uniaxial stress, analogous to the Split Hopkinson Bar, the longitudinal wave velocity C_0 is expressed as:

$$C_0 = \sqrt{\frac{E}{\rho}} \quad [8]$$

For an elastic distortional or shear wave through a continuous media, the wave velocity C_s is:

$$C_s = \sqrt{\frac{\mu}{\rho}} \quad [9]$$

2.3.2 Elastic Wave Interaction

The elastic stress waves propagating through a media reflect and refract at the interface between two different media. The stress wave reflection and refraction is explained with the aid of Figure 5. The longitudinal stress wave (marked with an arrow) is initially propagating through media A at velocity, C_1. The longitudinal wave reaches the interface between media A and B, where each media has different sonic impedances (product of media density and wave velocity). At the media interface, the longitudinal wave is reflected back into media A as a longitudinal wave and transverse wave as well as refracted into media B. The longitudinal stress wave is refracted into media B as longitudinal and transverse waves with velocities C_1' and C_2' respectively. The refraction and reflection angles in Figure 5 are calculated by the relationship:

$$\frac{\sin\theta_1}{C_1} = \frac{\sin\theta_2}{C_2} = \frac{\sin\theta_3}{C_3} = \frac{\sin\theta_4}{C_1'} = \frac{\sin\theta_5}{C_2'} \quad [10]$$

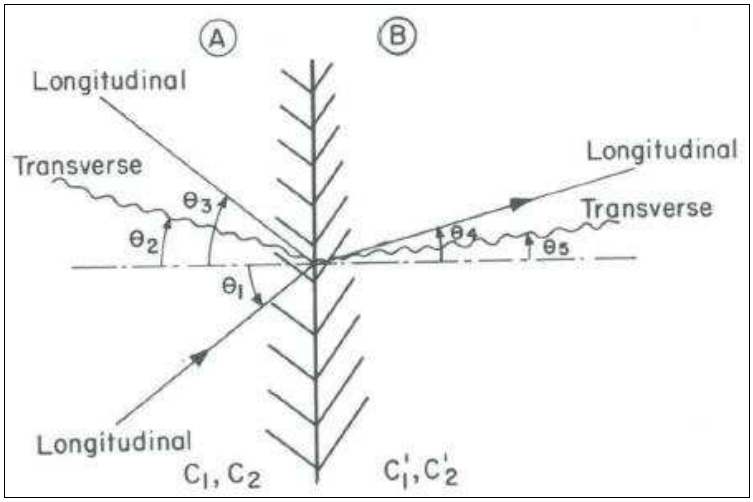

Figure 5 Interface between medium A (wave speeds C_1 and C_2) and medium B (with wave speeds C_1' and C_2') (reproduce from [57]).

The slender bar in Figure 6 is composed of two different materials A and B. The bar is struck by a hammer, which generates an incident uniaxial longitudinal stress wave in the bar. At the interface of the two materials, the incident longitudinal stress wave (σ_I) is transmitted (σ_T) and reflected (σ_R). The relative amplitudes of the transmitted and reflected stress waves developed at the interface are a function of material A and B's sonic impedance expressed as:

$$\frac{\sigma_T}{\sigma_I} = \frac{2\rho_B C_B}{\rho_B C_B + \rho_A C_A}$$

$$\frac{\sigma_R}{\sigma_I} = \frac{\rho_B C_B - \rho_A C_A}{\rho_B C_B + \rho_A C_A} \qquad [11]$$

where ρ_A and ρ_B are the densities for material *A* and *B*, respectively, and C_A and C_B are the longitudinal stress wave velocities for material *A* and *B*, respectively.

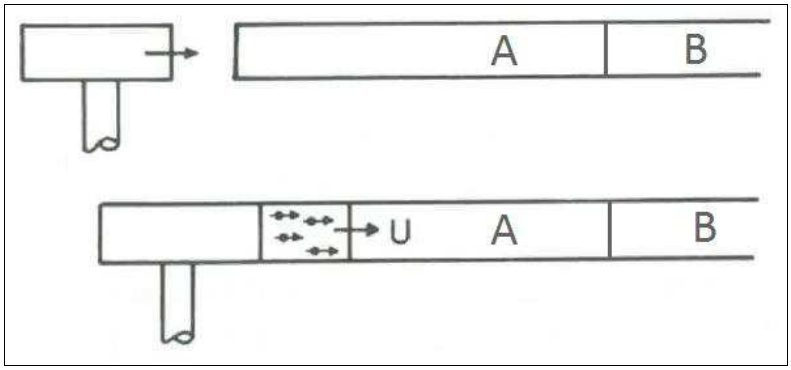

Figure 6 Hammer striking bar composed of materials A and B (reproduced and modified from [57]).

If the cylindrical bar's cross-sectional area, A_A and A_B changes at the interface between material A and B, the relative transmitted and reflected longitudinal stresses are expressed as:

$$\frac{\sigma_T}{\sigma_I} = \frac{2A_A\rho_B C_B}{A_B\rho_B C_B + A_A\rho_A C_A}$$

$$\frac{\sigma_R}{\sigma_I} = \frac{A_B\rho_B C_B - A_A\rho_A C_A}{A_B\rho_B C_B + A_A\rho_A C_A} \qquad [12]$$

The relative incident, reflected and transmitted particle velocities (U_{pI}, U_{pR}, and U_{pT} respectively) are expressed as:

$$\frac{U_{pT}}{U_{pI}} = \frac{2\rho_A C_A}{\rho_B C_B + \rho_A C_A}$$

$$\frac{U_{pR}}{U_{pI}} = \frac{\rho_A C_A - \rho_B C_B}{\rho_B C_B + \rho_A C_A} \quad [13]$$

From the above sets of equations, the relative transmitted and reflected stress wave amplitudes and particle velocities are directly related to the sonic impedance of the two materials. To illustrate the effect of impedance on the transmitted and reflected stress wave and particle velocity amplitudes, the extreme impedance values ($\rho_B C_B = \infty$, for a rigid surface and $\rho_B C_B = 0$, for a free surface) are considered for materials A and B. For an incident stress wave propagating in A toward a free surface where $\rho_B C_B = 0$, the $\frac{\sigma_T}{\sigma_I} = 0$ and $\frac{\sigma_R}{\sigma_I} = -1$. The incident stress wave is reflected opposite the incident stress wave tense and no stress is transmitted. For the particle velocity at the free surface interface, the $\frac{U_{pT}}{U_{pI}} = 2$ and $\frac{U_{pR}}{U_{pI}} = 1$. The transmitted particle velocity is double the incident particle velocity and the reflected particle velocity is the same tense and magnitude as the incident particle velocity. When the incident stress wave approaches a rigid interface such that $\rho_B C_B = \infty$, the $\frac{\sigma_T}{\sigma_I} = 2$ and $\frac{\sigma_R}{\sigma_I} = 1$, the transmitted wave is doubled and reflected wave is the same tense and magnitude as the incident stress wave. The particle velocity of the transmitted wave is effectively eliminated ($\frac{U_{pT}}{U_{pI}} = 0$) and the reflected wave particle velocity has the opposite sign ($\frac{U_{pR}}{U_{pI}} = -1$) as when the incident wave approaches a rigid surface. The magnitude of the uniaxial incident stress wave (σ_I) developed in a thin bar is derived from the conservation of momentum and presented as:

$$\sigma_I = \rho C U_p \quad [14]$$

The particle velocity corresponding to the incident stress wave is a function of the striker impact velocity V. Through the conservation of momentum, the particle velocity is expressed as:

$$U_p = \frac{V}{2} \quad [15]$$

For the impacted slender bar in Figure 3, one may calculate the theoretical incident, transmitted, and reflected uniaxial longitudinal stress wave magnitudes from the known impacted bar geometric and material parameters and the striker velocity. The slender bar elastic wave propagation theory is used by the Split Hopkinson bar experimental test to establish the strain rate characteristics of a particular material. Material strain rate is

briefly explained in the following section and the experimental setup, mechanical processes and results processing of the Split Hopkinson bar test are discussed as well.

2.4 Strain Rate

An important factor on the yield strength of material during dynamic loading, or the dynamic yield strength, is strain rate. The strain rate is the rate of change of strain with respect to time:

$$\dot{\varepsilon} = \frac{d\varepsilon}{dt} s^{-1} \qquad [16]$$

The strain rate experienced by a material is a function of the loading rate, such as the shock or projectile velocity at impact. A graph of strain rates, loading methods and dynamic testing considerations is presented in Figure 7. The lower strain rates between 10^{-5} and 0 s^{-1} result from constant static loads or creep. The quasi-static strain rates between 0.1 and 10^{-5} s^{-1} are typical of strain rates experienced during a classical material coupon test used to determine the quasi-static stress-strain behavior of the material free of strain rate effects. The experimental testing and material data presented in the following sections will focus on the material behavior at high and very high strain rates.

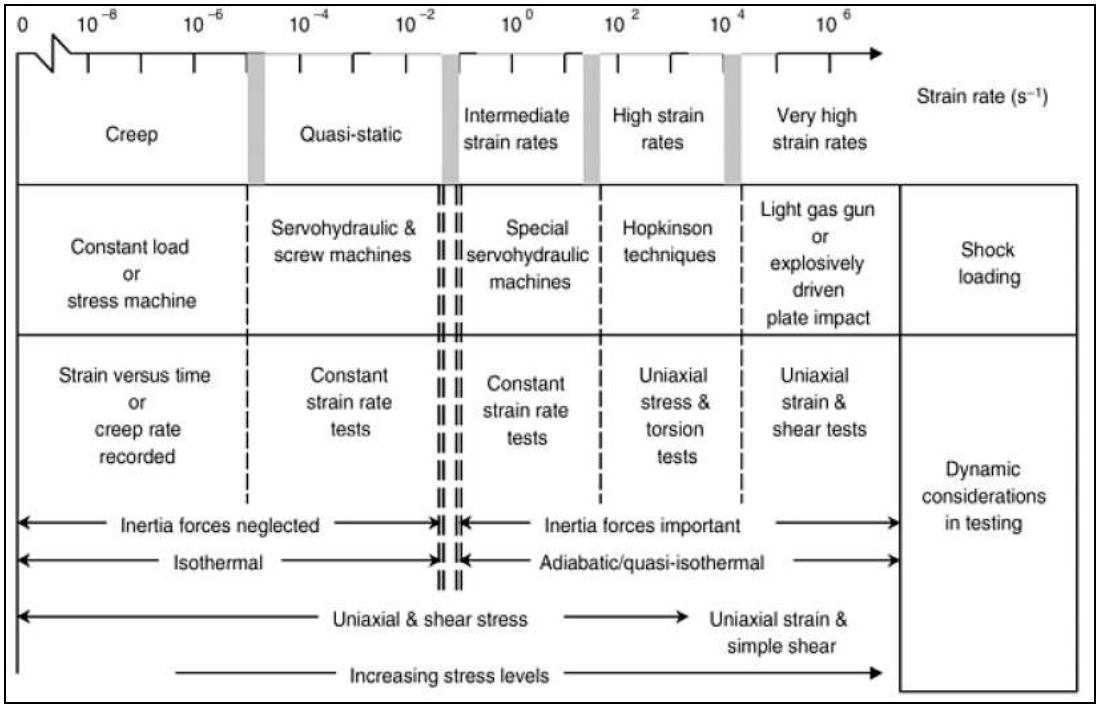

Figure 7 Tabulated strain rates with corresponding loading method and dynamic test considerations (reproduced from [12]).

The influence of strain rate on the dynamic yield strength of a material varies. This variation is referred to as strain rate sensitivity. The stress-strain curves in Figure 8 present the strain rate sensitivities of 7075-T6 aluminum (left) and titanium-aluminum alloy (right). The yield stress of 7075-T6 aluminum remains constant with increasing strain rate and is considered insensitive to strain rate. The contrary to aluminum is the titanium-aluminum alloy, which is strain rate sensitive and experiences an increase in yield strength with increased strain rate. This increase in yield strength with strain rate is the dynamic yield strength at a given strain rate. The dynamic yield strength at a particular strain rate is an important aspect to consider when predicting the structural response to dynamic loads. At very large strain rates the loaded material may deform elastically although the stresses may be beyond the quasi-static elastic limit.

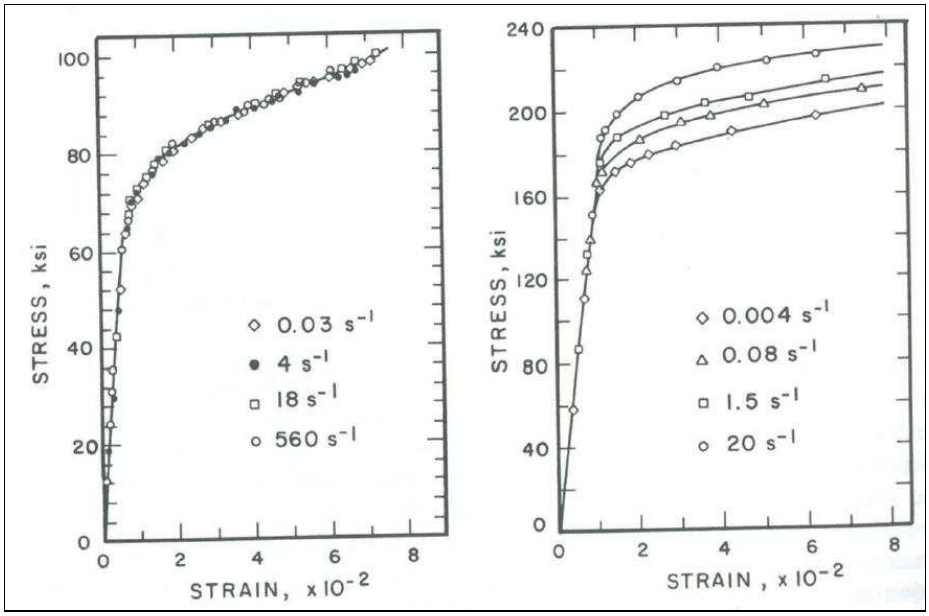

Figure 8 Stress-strain curves at multiple strain rates for 7075-T6 aluminum (left) and titanium-aluminum alloy (right) (reproduced from [57]).

2.4.1 Split Hopkinson Bar Test

In order to establish the dynamic yield strength of a material and the strain rate sensitivity, one must test the material experimentally. One such test is the Split Hopkinson bar test, which applies the elastic stress wave principles to calculate the strain rate sensitivity and dynamic yield strength of a material for strain rates between 10^2-10^4 s^{-1}. The experimental test in Figure 9 uses the measured incident, reflected and transmitted

strain time histories to calculate the specimen stress, strain and strain rate as a function of time.

A compressive wave is generated by the striker bar colliding with the incident bar. The axial compressive wave travels through the incident bar to the specimen and into the transmitter bar. The incident, reflected and transmitted elastic compressive stress waves are measured by the strain gauges fixed to the incident and transmitter bars.

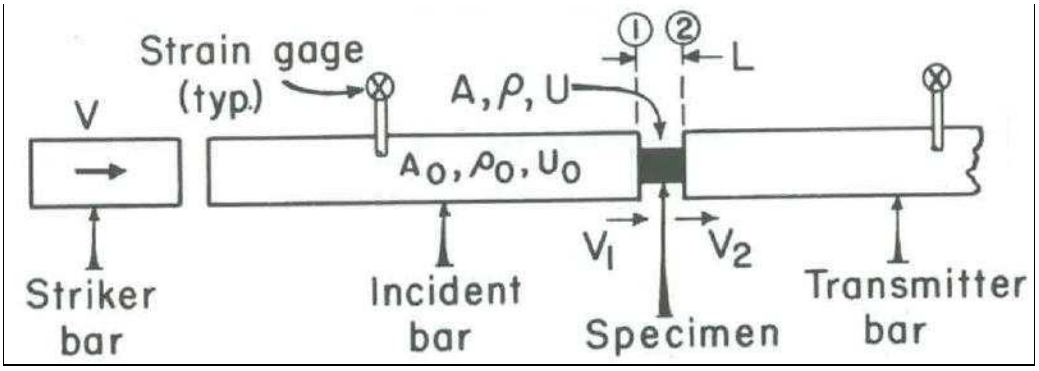

Figure 9 Split Hopkinson bar experimental setup (reproduced from [57]).

The stress, strain and strain rate in the specimen can be calculated from the recorded strain gauge data. The procedure to calculate the specimen stress, strain and strain rate follows. The strain rate as a function of time is presented as:

$$\dot{\varepsilon} = \frac{d\varepsilon}{dt} = \frac{(V_1(t) - V_2(t))}{L} \quad [17]$$

where, V_1 and V_2 are the velocities measured at the specimen interfaces between the incident and transmitted bars, respectively, and L is the length of the specimen. The interface velocities are computed from the measured strains in the incident and transmitter bars. The stress is expressed as a function of density ρ, elastic stress wave velocity C and particle velocity U_p:

$$\sigma = \rho C U_p \quad [18]$$

Since:

$$\frac{\sigma}{E} = \varepsilon \quad [19]$$

The particle velocity, as per the derivation in [57], can be expressed as:

$$C\varepsilon = U_p \quad [20]$$

So generally, the velocity interfaces are:

$$V_1 = C_0\varepsilon_I \quad \text{and} \quad V_2 = C_0\varepsilon_T \qquad [21]$$

where ε_I and ε_T are the incident and transmitted strains respectively. Since the incident bar cross section is greater than the specimen cross section and a change in impedance occurs, some of the stress wave is transmitted to the transmitter bar and the rest is reflected back into the incident bar. The interface velocity must be expressed as:

$$V_1 = C_0(\varepsilon_I - \varepsilon_R) \qquad [22]$$

The strain rate equation becomes:

$$\frac{d\varepsilon}{dt} = \frac{C_0(\varepsilon_I - \varepsilon_R) - C_0\varepsilon_T}{L} \qquad [23]$$

where ε_R, ε_I and ε_T are the reflected, incident and transmitted strain amplitudes, respectively.

The strain rate in the specimen is expressed as:

$$\dot{\varepsilon}(t) = \frac{C_0}{L}(\varepsilon_I - \varepsilon_R - \varepsilon_T) \qquad [24]$$

The strain in the specimen is calculated by integrating the strain rate from 0 s to time *t,* where *t* corresponds to the instantaneous strain of interest.

$$\varepsilon(t) = \frac{C_0}{L}\int_0^t [\varepsilon_I(t) - \varepsilon_R(t) - \varepsilon_T(t)]\, dt \qquad [25]$$

If equilibrium is assumed, the stress in the specimen is a function of the interface forces at 1 and 2 (P_1 and P_2, respectively):

$$\sigma = \frac{P_1(t) + P_2(t)}{2A} \qquad [26]$$

Since stress is a function of strain and the stress waves propagating through the bars is elastic, the forces at interfaces 1 and 2 are:

$$P_1(t) = A_0E_0(\varepsilon_I + \varepsilon_R)$$

$$P_2(t) = A_0E_0\varepsilon_T \qquad [27]$$

So, the stress in the specimen/bar interface, as a function of time, can be presented by:

$$\sigma(t) = \frac{A_0E_0}{2A}[\varepsilon_I(t) + \varepsilon_R(t) + \varepsilon_T(t)] \qquad [28]$$

An example of the strain gauge measurement from a Split Hopkinson bar test is in Figure 10. The strain gauge voltage will be converted to strain or micro-strain and used to calculate the specimen stress, strain and strain rate during the test. The transmitted and reflected strain time histories are offset to display the shape of the reflected and

transmitted strains. One may notice that the strain in the incident and reflected waves are not constant, but oscillate. The oscillations are caused by the longitudinal stress wave reflection off of the free surface of the incident bar. Since the strain gauge is fixed to the surface of the incident bar, the reflected waves are measured during the experiment. The longitudinal stress free surface reflection waves are depicted in Figure 11. Prior to the hammer strike, no longitudinal stress waves are present; however, once the bar has been struck the stress propagates along the bar, and many free surface wave reflections occur causing the recorded oscillations.

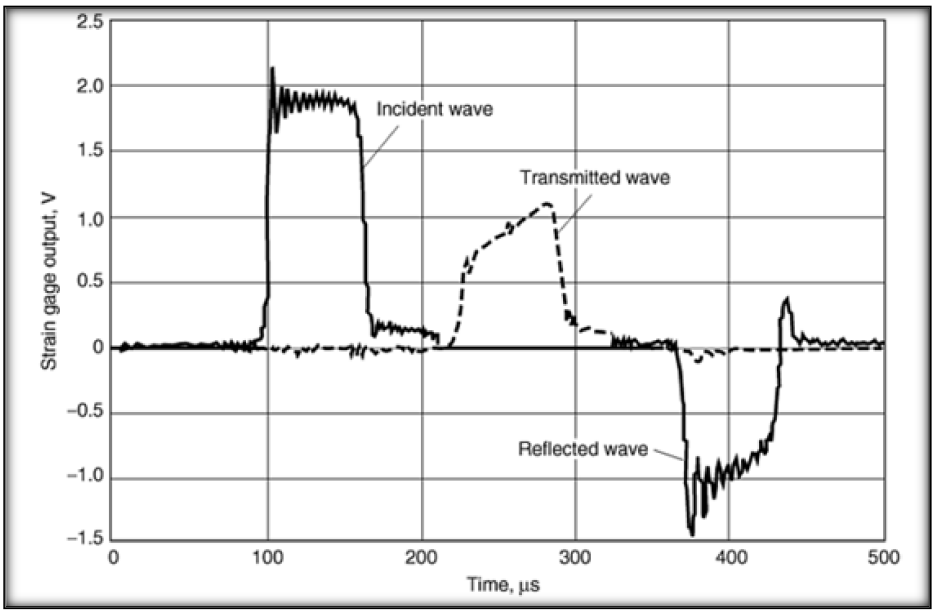

Figure 10 Measured stress-strain time-history from the Split Hopkinson bar test (reproduced from [12]).

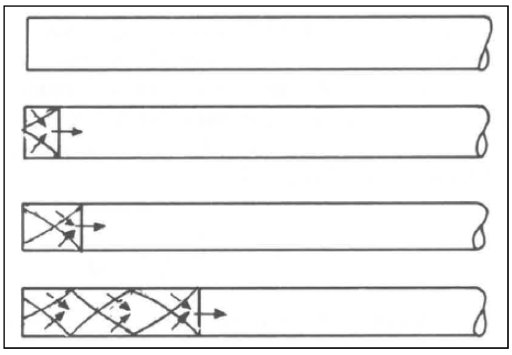

Figure 11 Reflection of the longitudinal stress wave off of the free surface of the incident bar (reproduced from [57]).

The stress-strain material response characteristics of the specimen in the Split Hopkinson bar test are commonly applied in constitutive equations to numerically predict the stress-strain behavior of the specimen material under varying stain rates. The formulation of the Cowper-Symonds and Johnson-Cook constitutive equations are discussed in the following section.

2.4.2 Constitutive Equations

The structural response of a naval vessel to an UNDEX event is often predicted using the finite element methods. To include strain rate effects in the simulation, the vessel material definition applies a constitutive equation or multiple constitutive equations depending on the available material data and simulation objectives. The function of a constitutive equation is to compress the stress-strain curves for each strain rate of a given material (similar to the stress-strain curves for titanium-aluminum alloy in Figure 8) and expressed using a single constitutive equation. There are many constitutive equations that work well for particular applications. The two most common constitutive equations applied in engineering applications are the Johnson-Cook and Cowper-Symonds equations. A brief discussion of the Johnson-Cook and Cowper-Symonds equation formulations are to follow.

The Cowper-Symonds constitutive equation effectively scales the yield strength of a material to calculate the dynamic yield strength at a particular strain rate based on a minimal amount of material data. The Cowper-Symonds equation is expressed as:

$$\sigma_{yd}(\dot{\varepsilon}_p) = \sigma_y \left(1 + \left(\frac{\dot{\varepsilon}_p}{D}\right)\right)^{\frac{1}{P}} \quad [29]$$

where σ_{yd} is the dynamic yield strength as a function of the quasi-static yield strength σ_y, instantaneous strain rate $\dot{\varepsilon}_p$ and material constants D and P. The Cowper-Symonds constitutive equation is a power law function and relatively simple in comparison to other constitutive equations. The Cowper-Symonds equation is ideal when an approximation of material behavior is required since the Cowper-Symonds equation has relatively few material constants. A more sensitive constitutive equation to material characteristics is the Johnson-Cook model, which accounts for the material stress, strain rate and

temperature. The dynamic stress as a function of the instantaneous strain ε_p, strain rate $\dot{\varepsilon}_p$, and temperature T is calculated by the Johnson-Cook constitutive equation and expressed as:

$$\sigma_d(\varepsilon_p, \dot{\varepsilon}_p, T) = (\sigma_0 + B\varepsilon_p^n)\left(1 + Cln\frac{\dot{\varepsilon}_p}{\dot{\varepsilon}_0}\right)[1 - (T^*)^m]$$

in which,

$$T^* = \left(\frac{T - T_r}{T_m - T_r}\right) \qquad [30]$$

where T_m is the material melting temperature and T_r is the reference temperature at which the reference yield stress σ_0 and strain rate $\dot{\varepsilon}_0$ are measured. The material constants , n, C, and m are experimentally determined values, thus making the Johnson-Cook equation sensitive to many material parameters. The sensitivity of the material parameters is compounded by multiplication of the stress, strain rate and temperature effects. Even though the Johnson-Cook equation is highly sensitive to material parameters, stress, strain rate and temperature, it is the most frequently applied constitutive equation.

2.5 Plastic Stress Wave

If the stress wave propagating through a media has an amplitude greater than the elastic yield limit, a portion of the stress wave is considered to be a plastic stress wave. The elastic yield limit varies with strain rate sensitivity, which indicates that the portion of the stress wave considered as plastic, will also vary with strain rate. The differentiating characteristics between elastic and plastic stress waves are the stress amplitude and the propagating wave velocity. The plastic wave is slower than the elastic wave since stress wave speed is proportional to the slope of the stress-strain relationship. Similar to the longitudinal elastic wave speed for longitudinal waves in equation [8], the longitudinal plastic stress wave speed may be expressed as:

$$V_p = \sqrt{\frac{d\sigma/d\varepsilon}{\rho}} \qquad [31]$$

A general stress-strain curve illustrated in Figure 12 presents the change in the slope of the stress-strain relationship at different stress levels in the plastic and elastic regimes. In the elastic regime, Young's modulus defines the slope of the stress-strain curve; however, in the plastic regime the slope of the stress-strain curve varies with stress and strain level.

As stress and strain increase in the plastic regime, the plastic wave velocity decreases. As a result of the decreased plastic wave velocity, wave dispersion occurs. The wave dispersion is presented in Figure 13. The two graphs are plotting stress with respect to distance traveled along the uniaxial stress direction. At early time t_1, in the left graph, the wave dispersion is less than at time t_2, right. As the elastic and plastic waves propagate through the media the dispersion increases with propagation distance.

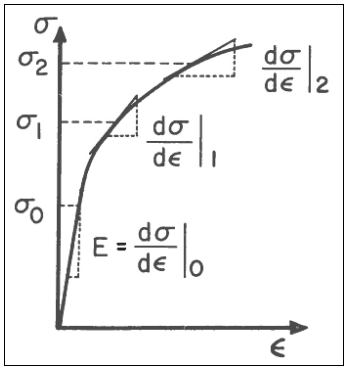

Figure 12 General stress-strain curve with slope of the curve presented at different stress levels (reproduced from [57]).

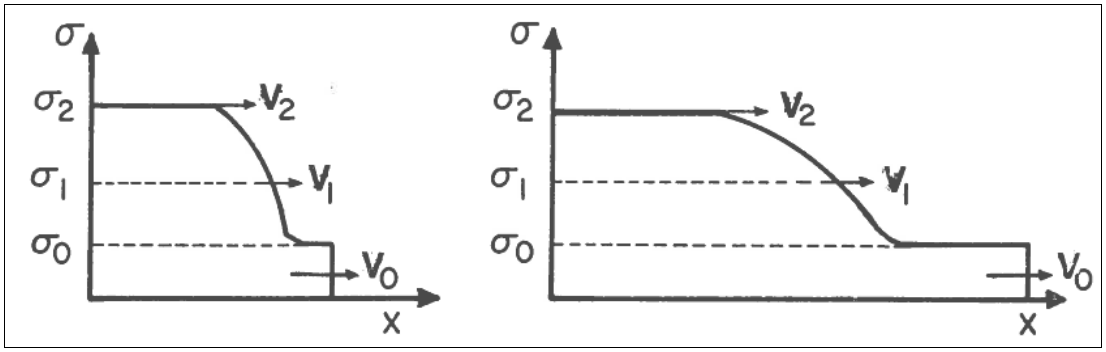

Figure 13 Stress wave dispersion between elastic stress and plastic stress wave velocities at two instances in time: early (left) and late (right) (reproduced from [57]).

The Split Hopkinson bar test is limited to the elastic stress wave propagation within the bars. For higher strain rates which include plastic deformation and plastic stress, the Taylor test is required to calculate the dynamic yield strength of an unknown material.

2.5.1 Taylor Test and Dynamic Yield Strength

The elastic wave propagation during the Split Hopkinson bar test is measured using strain gauges to obtain the material strain rate sensitivity and dynamic yield strength for strain rates between 10^2-10^4 s^{-1}. For strain rates between 10^4 -10^5 s^{-1} and high plastic strains between 50-150%, the Taylor test is used to calculate the dynamic yield strength. The Taylor test in Figure 14 consists of a specimen rod, shot from a gun or launcher, colliding with a rigid wall.

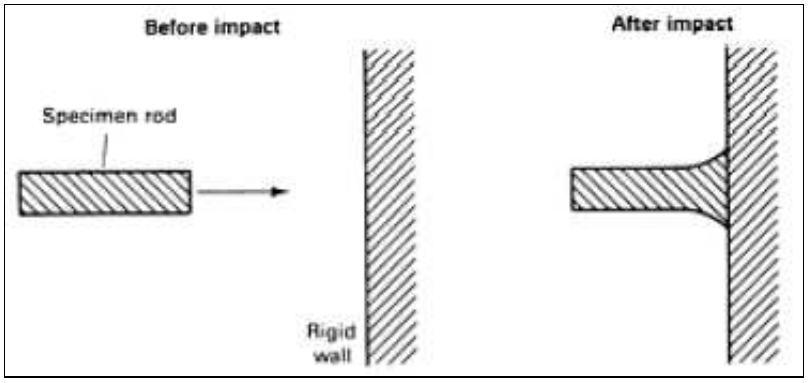

Figure 14 Taylor test experimental setup (reproduced from [57]).

The elastic and plastic wave dynamics are described well in the Taylor test deformation series in Figure 15. Initially a projectile with length L is travelling with a velocity U towards a rigid wall. Upon impact with the rigid surface, an elastic wave travels into the rod propagating at velocity C with a plastic wave following at velocity v. The distance from the rigid interface and the plastic front is denoted as h. The elastic wave has a greater velocity than the plastic wave and propagates until it encounters the free surface of the rod end. The free surface interaction with the elastic wave front reduces the rod free end velocity by $\frac{2\sigma_{yd}}{C\rho_0}$. Once the projectile comes to rest, the final deformed length L_l is composed of elastic region X, and deformed plastic region $L_l - X$.

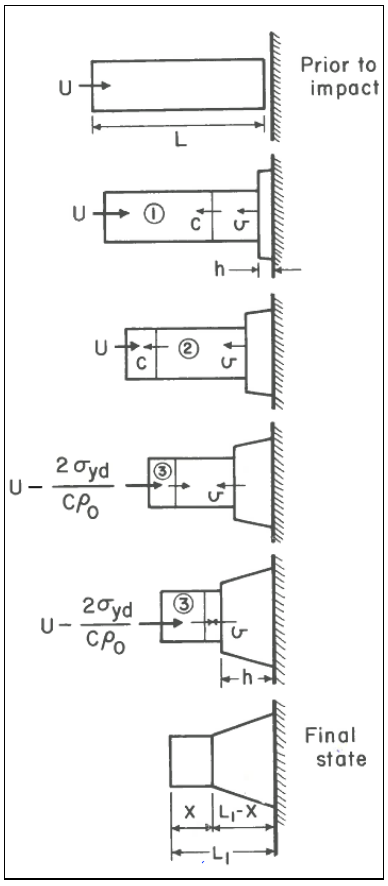

Figure 15 Taylor's test deformation series early to late times (top to bottom) (reproduced from [57]).

The dynamic yield strength, σ_{yd}, can be calculated from the initial and final shape of the Taylor test specimen rod by solving:

$$\frac{L_1}{L_0} = \left(1 - \frac{h}{L_0}\right) \exp\left(-\frac{\rho_0 U^2}{2\sigma_{yd}}\right) + \frac{h}{L_0} \qquad [32]$$

where L_1 and L_0 are the final and initial specimen rod lengths respectively, h is the distance from impact interface to plastic front, ρ_0 is the initial density of the specimen and U is the specimen velocity.

At very high strain rates and stress wave magnitudes, the dynamically loaded material behaves in accordance to the specific properties associated with the shocked state of the material. The parameters defining the material behavior in a shocked state, as well as shock experimental tests, and calculations are discussed in the following section.

2.6 SHOCK WAVES

A shock wave forms in a material when the amplitude of the stress wave is greater than the dynamic flow strength of the material at strain rates at or above 10^5 s^{-1}. This commonly occurs when instantaneous pressure loads are in gigapascal range [56]. The development of a shock front and the shock wave propagation are explained using the piston example illustrated in Figure 16. The piston is initially at rest within a cylinder of gas at pressure P_0, density ρ_0 and energy E_0. The piston is moved into the compressible gas with velocity, U_p, compressing the gas immediately in front of the piston. This compression of the gas atoms creates a shock front travelling at a velocity, U_s. Between the shock front and the piston face is a dense region with increased pressure. The length of the compressed region is defined simply as the difference in shock front and piston velocity multiplied by the shock duration time t_1, $(U_s - U_p)t_1$.

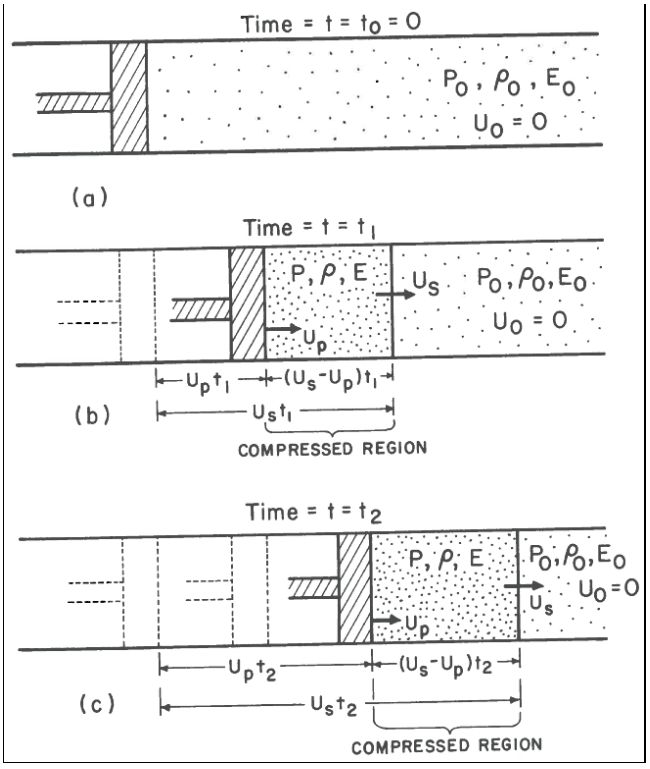

Figure 16 Gas and piston in a cylinder. Piston is initially at rest in a), with velocity U_p in b) and with velocity U_p distance travelled $U_p t_2$ in c) (reproduced from [57]).

At high levels of dynamic flow stress, it can be assumed that the solid material has no resistance to shear and the Rankine-Hugoniot conservation equations may be applied to calculate the shock wave parameters [56]. Generally, the conservation of mass, momentum and energy equations are:

Mass, $\rho_0 U_s = \rho(U_s - U_p)$ [33]

Momentum, $P - P_0 = \rho_0 U_s U_p$ [34]

Energy, $E_n - E_{n0} = \frac{1}{2}(P + P_0)(V_0 - V)$ [35]

where V_0 and V are the media specific volume immediately before and after the shock front, respectively, while the energy, density and wave velocity naming convention remains consistent with that shown in Figure 16. The Rankine-Hugoniot conservation equations can be used to solve for the pressure or energy in the system. In order to use the Rankine-Hugoniot conservation equations, the shock velocity, U_s, must be calculated as a function of the material characteristics the shock wave is travelling through.

The equation that characterizes the shock velocity as a function of the propagation media and particle velocity is called the equation of state (EOS), which has a polynomial form:

$U_s = C_0 + S_1 U_p + S_2 {U_p}^2 + \cdots$ [36]

where C_0 is the sound velocity of the media, and empirical parameters S_1 and S_2 characterize the media. For most metals [56], $S_2 = 0$, thus the polynomial is reduced to:

$U_s = C_0 + S_1 U_p$ [37]

Using the EOS and Rankine-Hugoniot conservation equations, one can calculate the $P - U_p$, $P - \rho$, $P - {V}/{V_0}$, $E - U_s$, and other relationships, assuming the material does not undergo phase transformations. An example of an experimentally measured EOS for multiple materials is provided in Figure 17, proving the shock wave velocity is a linear function of particle velocity.

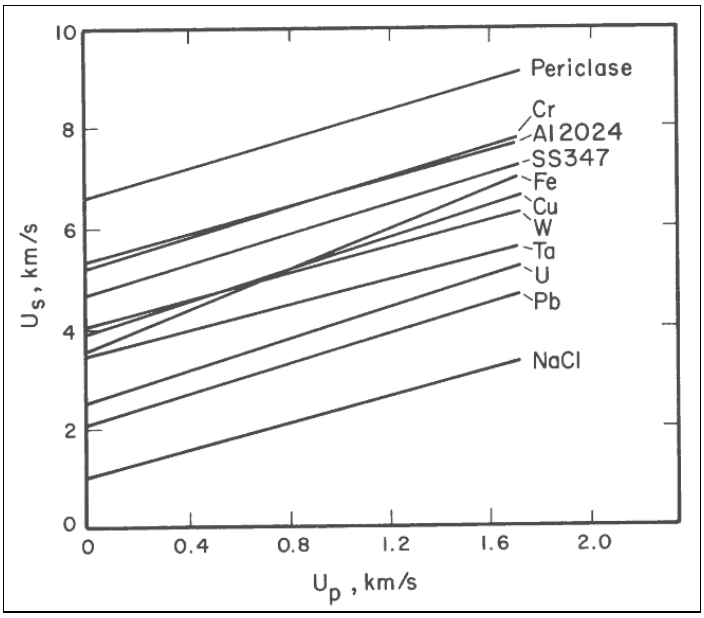

Figure 17 Experimentally determined EOS for multiple materials (reproduced from [57]).

Important shock front and material properties can be derived from the $P-\rho$ relationship immediately behind the shock front. The shocked state of the material in this region is defined by the Rankine-Hugoniot equation or "Hugoniot", which is based on the $P-\rho$ relationship. An example of the Hugoniot is presented in the pressure-specific volume plot shown in Figure 18 as the curved line, which describes the shocked state material properties. The straight line in Figure 18, joining (P_0, V_0) to (P_1, V_1), is called the Rayleigh Line and defines the shock state at P_1. It is important to note that the pressure in a shock front increases as a function of the specific volume from P_0 to P_1. The pressure does not increase along the Hugoniot, $P - {}^{V}/_{V_0}$,but discontinuously, defined by the slope of the Rayleigh line.

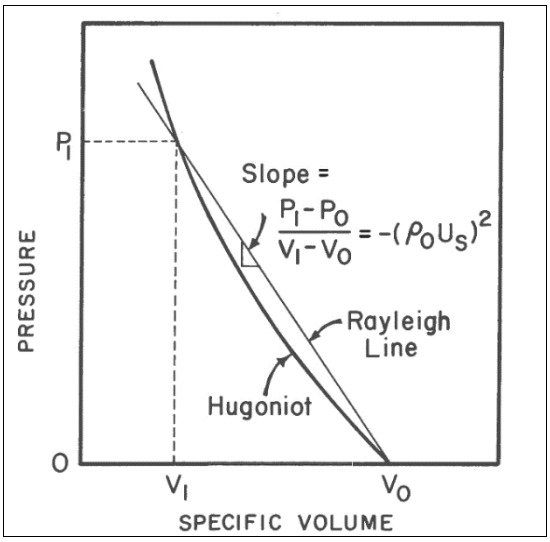

Figure 18 Pressure-specific volume Hugoniot and Rayleigh line (reproduced from [57]).

The Hugoniot and EOS of shocked media are applied in scientific and engineering applications. Using the impedance matching technique, the material EOS can be determined and subsequently used to represent the material response subject to shock loading. The impedance matching technique is discussed in the following sections as well as the applications of the technique in the flyer plate test.

2.6.1 Impedance Matching

A common application of a material Hugoniot and EOS is in the impedance matching technique used to determine the EOS of an unknown material during a Flyer Plate test. Generally, the impedance matching technique plots the inverse Hugoniot at a given particle velocity to determine the pressure during the shock event. To explain the technique, a planar impact example will be used. In this example, a tungsten-carbide (WC) projectile is impacting an iron target at 1200m/s. The impact pressure and reduction in impact velocity of the projectile is determined.

Since the tungsten carbide and iron Hugoniots are known, they will be used graphically to calculate the pressure and velocity. The two Hugoniot material pressure-particle velocity curves are plotted together in Figure 19. The impacting WC projectile Hugoniot is inverted and shifted so P_0 has a particle velocity of 1200m/s. The resulting particle

velocity and impact pressure is determined by the intersection of the two Hugoniot curves. For this example, the impacting pressure is 32GPa and particle velocity reduction of 400m/s. The Flyer Plate test, explained in the following section, uses the impedance matching technique to determine the EOS of a particular material.

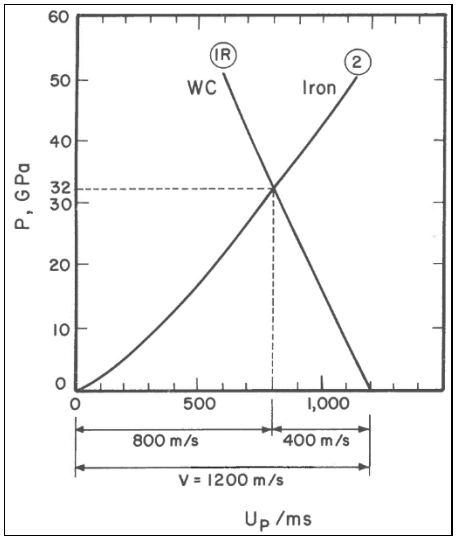

Figure 19 Impedance matching technique for 1200m/s WC projectile colliding with Iron target (reproduced from [57]).

2.6.2 Flyer Plate Test

The Flyer Plate test is used to determine the material EOS from the impact response characteristics using the impedance matching technique. The test consists of a flyer plate of known EOS, propelled by a gas-gun and colliding with a target plate of unknown EOS. The Flyer Plate test setup in Figure 20 shows the components of the Flyer Plate test. A plastic sabot is used to keep the flyer plate planar as it travels down the gas gun barrel. The ring around the flyer plate is used to calculate the particle velocity of the flyer plate by triggering the shorting pin as it leaves the barrel and colliding with the Time-of-arrival pins as the flyer plate collides with the target plate held in a spall ring. The Flyer Plate test uses the particle velocity of the flyer plate prior to impact and target plate shock or particle velocity at impact to determine the EOS of the target plate. The flyer plate velocity prior to impact is measured from the shorting pin and time-of-arrival pins. The free surface velocity of the back of the target plate is measured using laser interferometry.

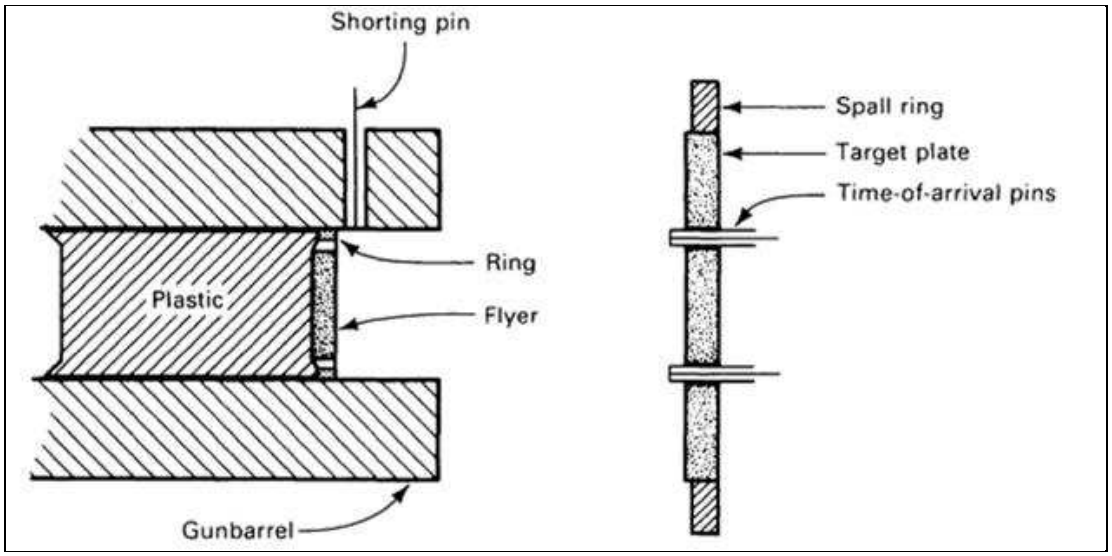

Figure 20 Flyer plate test experimental setup (reproduced from [57]).

Since the flyer plate velocity, EOS, target plate density and shock wave velocity are known, the EOS of the target plate may be calculated using the impedance matching technique. The pressure-particle velocity graph in Figure 21 presents the application of the impedance matching technique to calculate the EOS for the target plate for three different flyer plate impact velocities. The $P - U_p$ curve for the unknown target plate material can be constructed by connecting the intersecting points between the Rayleigh line (with slope=$\rho_0 U_s$) and inverted shock Hugoniot at each flyer plate particle velocity. Using the shock parameter relationships and the $P - U_p$ curve, the EOS of the target plate can be determined.

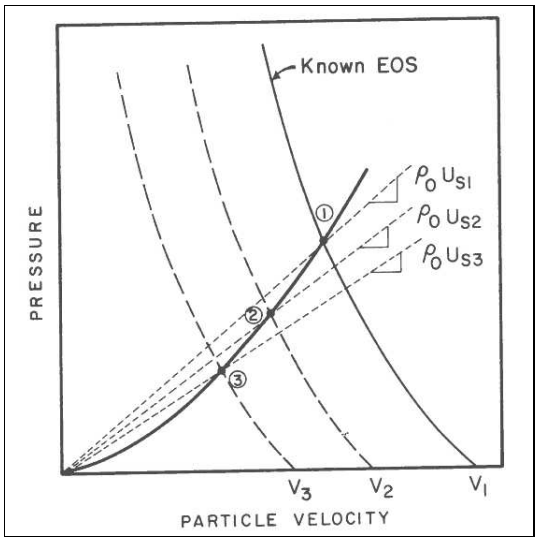

Figure 21 Impedance matching technique to calculate EOS of the target plate unknown material (reproduced from [57]).

2.6.3 Shock Wave Interaction

The pressure, density and wave velocity change when a shock wave propagates from one medium to another. The magnitude of the change is a function of the shock impedance ($\rho_0 U_s$) of the two mediums. To calculate the change in pressure, density, etc. one may apply the impedance matching technique.

For the case in which a shock wave is transmitted from material A with low impedance to material B with high impedance, the impedance matching technique in Figure 22 shows the magnitude of the pressure and particle velocity propagating in each medium. The Hugoniot of medium A is inverted and shifted such that the inverted Hugoniot intersects Hugoniot A and the Rayleigh line or shock impedance. This provides the analyst with the initial pressure travelling in medium A of P_1 and at particle velocity U_{P1}. As the shock front propagates into medium B, the pressure increases and particle velocity decreases corresponding to the pressure and particle velocity at the medium B Hugoniot intersection with inverted medium A Hugoniot. The transmitted and reflected pressure in each medium at t_0, t_1, t_2, t_3 and t_4 correspond with the impedance matching technique pressures and particle velocities. The pressure wave is transmitted and reflected as a compressive wave at the interface.

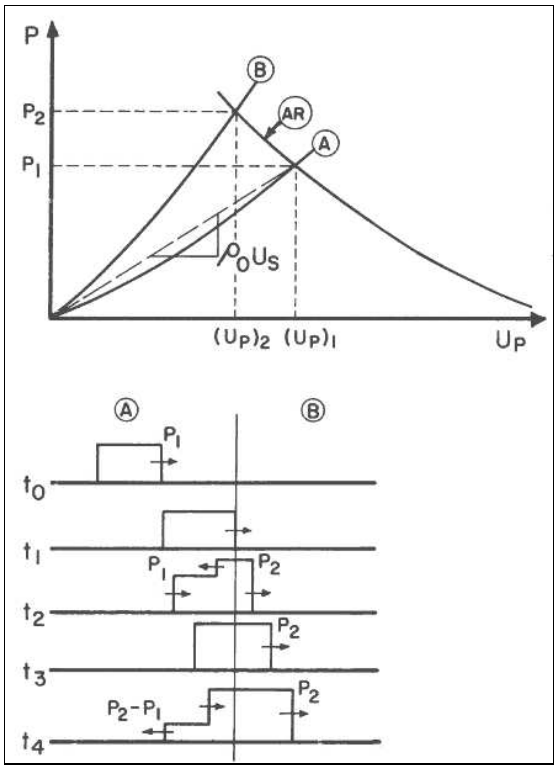

Figure 22 Impedance matching to determine pressure P_2 and particle velocity U_{P2} in material B (top) and resulting pressure time history in low impedance material A and high impedance material B (bottom) (reproduced from [57]).

For the case in which a shock wave is transmitted from material A with a high impedance to material B with a low impedance, the impedance matching technique and corresponding pressure profile are presented in Figure 23. Similar to the low-high impedance reaction, the Hugoniot for medium A is inverted and shifted such that it is mirrored at P_1. The pressure transmitted into medium B is reduced and travels at a greater velocity. The reduction in pressure produces a reflected tensile pulse in medium A which follows the compressive pulse into medium B. If the tensile pulse is large enough, a spall will generate.

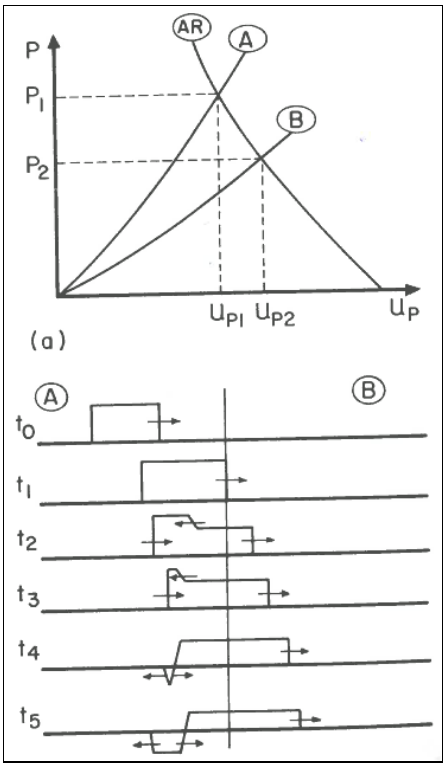

Figure 23 Impedance matching to determine pressure P_2 and particle velocity U_{P2} in material B (top) and resulting pressure time history in high impedance material A and low impedance B (bottom) (reproduced from [57]).

The formation of a spall occurs when the tensile pulse is greater than the spall stress. The spall stress is defined as the highest tensile stress that exists prior to material rupture, which may be obtained experimentally using the Flyer Plate test. The spall stress corresponds with the highest flyer plate impact velocity without spallation occurring. The tensile pulse generated in the flyer plate test is an extreme example of a shock wave transmitted from medium A with high impedance to medium B with low impedance. The impedance matching technique and pressure profile for the case with impedance in material B of zero is presented in Figure 24. The Hugoniot is inverted and reflected about the intersection at P_1. Since material B has impedance of zero, the reflected pressure wave is 0 and once the duration of the initial pressure pulse in medium A has been reduced to 0, a tensile wave is created. The maximum magnitude of the tensile wave that does not cause rupture in the target plate is the spallation stress of the target plate material.

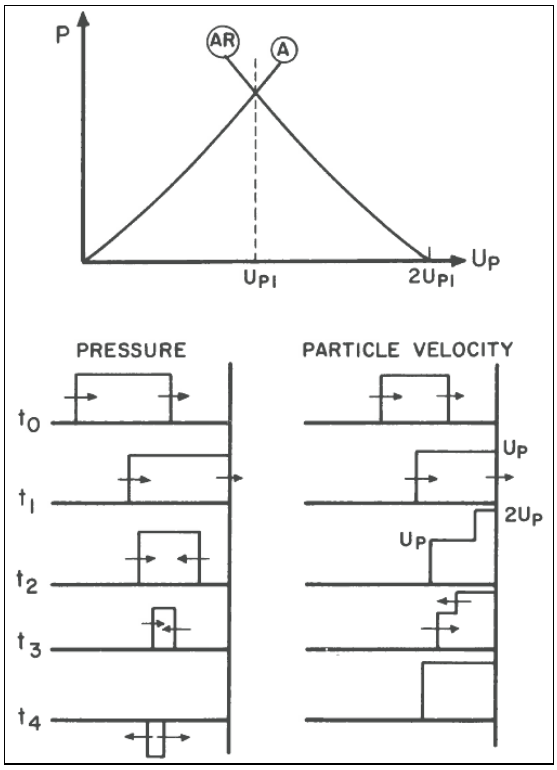

Figure 24 Free surface impedance matching (top) and resulting pressure time history (bottom) (reproduced from [57]).

2.7 STRESS WAVE PROPAGATION SUMMARY

The dynamic behavior of ductile materials has been reviewed to investigate the influences on material dynamic stress, how stress propagates, and how to empirically predict the behavior of a particular material under dynamic loading conditions.

The resistance of a material to dynamic loads is characterized by the dynamic yield strength of the material. The dynamic yield strength is a function of the material strain rate sensitivity. The materials that exhibit a high sensitivity to strain rate have correspondingly higher dynamic yield strengths than quasi-static yield strength. In order to determine the strain rate sensitivity of a material, the Split Hopkinson Bar, Taylor and Flyer Plate tests may be used to investigate material response at different strain rate ranges.

The elastic stress wave mechanics are utilized to process the specimen strain rate characteristic when using the Split Hopkinson Bar for strain rates between 10^2-10^4 s^{-1}. For strain rate sensitivities at strain rates above 10^4 s^{-1} and high plastic strain levels, the Taylor test is used. To determine the EOS of a material in a shocked state and the spallation stress, the Flyer Plate test is used. The experimental tests may be used to determine the material characteristics at high strain rates. Based on the material characteristics, the suitability of the tested material for a particular application may be determined.

The dynamic yield strength of the material at various strain rates may be approximated using a constitutive equation. The Cowper-Symonds and Johnson-Cook constitutive equations are presented to provide an example of a simple (Cowper-Symonds) and relatively complicated (Johnson-Cook) equations. The application of either equation is a function of the available material parameters and analysis requirements. The Johnson-Cook equation requires more material parameters than Cowper-Symonds however it accounts for and is sensitive to the instantaneous stress, strain rate and temperature. The Cowper-Symonds equation requires two material parameters and does not account for temperature.

The response of an unknown material to dynamic loads may be empirically estimated by determining the dynamic yield strength experimentally or by approximating the stress-strain behavior using a constitutive equation. The experimental test must be chosen to reflect the strain rates expected during the dynamic loading application. The experimental testing procedure, stress wave mechanics and post processing calculations have been presented for strain rates above $10^2 s^{-1}$.

CHAPTER 3 LITERATURE REVIEW

A structural response highly sensitive to elastic and plastic stress wave propagation is dynamic pulse buckling and may occur during impact or high pressure loading scenarios. Dynamic pulse buckling may be elastic or plastic; however, it is distinguished from dynamic vibrational buckling, in which the short duration high amplitude load pulse causes the buckling response. A literature review is also included in this chapter to outline the solution methodologies used to predict dynamic pulse buckling as well as the validating experimental and numerical studies.

Early literature provides a brief history or description of structural response subject to dynamic loading with respect to the stability of the loaded structure. Most of the studies used experimental methods to verify their theoretical findings. A trend found in the early literature is the transition from understanding the general behaviour of structures to predicting their response using mathematical formulations. Few studies correlate stress wave propagation with dynamic pulse buckling. As numerical methods advanced, the development of computer software has enabled the analyst a capability for solving finite difference problems quickly and efficiently. Once highly efficient finite element software became available, stress wave propagation behaviour could be used to characterize the buckling phenomena. The following sections present a summary from available literature describing early dynamic structural response, numerical prediction methods and the correlation between stress wave propagation and dynamic pulse buckling.

3.1 DYNAMIC STRUCTURAL RESPONSE

The earliest reference to dynamic buckling was by Koning and Taub [43] in 1934, who, investigated the dynamic stability of a curved bar (in a half sine shape) under a constant axial shock load with finite duration. By solving the partial differential equations for shock loads below, equal to and above the Eulerian static buckling load, Koning and Taub [42]found that the shock load required to induce buckling may be larger than the Eulerian static buckling load if the duration of the shock load is sufficiently short. The

effect of shock amplitude and duration on the dynamic stress state was compared to the static stress state under the Eulerian static load. For shock load durations equivalent to the fundamental period of free vibration, the dynamic shock load limit was found to be a fraction (0.97) of the Eulerian static buckling load. The effect of impulse on dynamic stress was also investigated by Koning and Taub since prior theory suggested that dynamic stress is independent of shock amplitude and duration but a function of shock impulse only. As a result of the study, it was shown that the dynamic stress is dependent on shock load amplitude and duration.

The work of Davidson [20] followed that of Koning and Taub by investigating the behaviour of a curved strut struck by a mass. The assumption that the stress waves and bending displacements act independently, presented by Koning and Taub [43], was evaluated. In Davidson's work, he developed and solved the equations of motion for the curved strut system, as well as experimentally testing an axially impacted strut. The experimental test results suggested that the axial load in the strut was constant, verifying Koning and Taub's theory. The test results also verified the accuracy of the equations of motion, which had indicated that a larger peak load could have been endured if the load had a sinusoidal load time history rather than a rectangular variation. The findings by Davidson are admissible to the elastic regime and a strut subject to a single strike.

The field of dynamic buckling was evaluated further by the experimental and theoretical investigations conducted by Bodner [14], who investigated the assumptions inherent in the theory of rigid plasticity. The theory of rigid plasticity ignores the elastic strain, elastic vibrations, shear deformation, changes in geometry, strain rate and strain-hardening, by assuming that the plastic deformation develops under constant yield stress. Bodner conducted an experiment in which a cantilevered beam with a mass fixed to the free end of the beam system was subject to acceleration applied to the base of the system. Bodner found that the theory of rigid plasticity was an adequate first-order theory, given that the ratio of input kinetic energy to maximum elastic energy is greater than three. Bodner further stated the theory of rigid plasticity was adequate for estimating the damage to complex structural systems to blast loads, where the energy ratio was greater

than 10. As for the effects that are ignored by the theory, it was found that the variation in dynamic and static yield stresses, due to the strain-rate effect, was the primary factor in the discrepancy found between theoretical predictions and experimental results. To account for the strain-rate effects, Bodner [14] applied the Cowper-Symonds strain-rate law to the material constitutive model, and found excellent agreement with his experimental results.

3.2 Dynamic Load Factor

The initial work of Budiansky and Hutchinson [15] is an effort to relate the dynamic buckling load to the static buckling load for the design of imperfection-sensitive structures. By solving the equilibrium equations for a simplified structural system (i.e., an axially loaded three-hinge beam model with a nonlinear spring), Budiansky and Hutchinson developed a set of analytical expressions to calculate the dynamic buckling load factor (DLF). Each expression may be approximated using:

$$\frac{\lambda_D}{\lambda_S} = \frac{7 + 3(\lambda_S / \lambda_C)}{10} \qquad \textbf{[38]}$$

where λ_D, λ_S and λ_C are the dynamic (imperfect), static (imperfect) and static (perfect) buckling loads, respectively. This expression is, however, limited to elastic buckling, where the same dynamic and static buckling mode shapes develop. It is also important to note that the expression has been developed assuming the system is subject to a suddenly applied axial load that is held at a constant value. Due to the limitations, the expression is inherently conservative. The later work by Budiansky and Hutchinson [32] considers the same simple 3-hinge model. However, the axial load had a finite duration and a particular load pulse shape. The dynamic (imperfect), static (imperfect) and static (perfect) buckling loads were calculated under axial rectangular and triangular pulse loads with varying duration. The influence of pulse shape was found to have little significance on the critical dynamic buckling impulse. The varying duration of the pulse load was evaluated with respect to the period of free vibration of the unloaded structure. Budiansky and Hutchinson found that the dynamic buckling load increased with a decrease in load duration that was less than the fundamental period of vibration.

Several other DLF criteria have been suggested since; examples are those developed by Volmir, Budiansky-Hutchinson, Ari-Gur and Simonetta, and Petry-Fahlbusch summarized in [46]. The Volmir criterion is based on a series of experimental tests in which a simply supported rectangular plate was subjected to rectangular and exponentially decaying pulse load. To determine the critical dynamic load, Volmir assumed the buckling mode (sine and half sine) was the critical mode if the dynamic plate response increased in deflection over the shortest time for particular pulse amplitude. Volmir then suggested that the loss of dynamic stability would occur when the out of plane deflection of the plate reaches an assumed critical value (usually equal to the plate thickness or half thickness).

The criterion developed by Budiansky and Hutchinson is based on tests performed on cylindrical shells and axially loaded rods. This criterion is based on displacement criterion and is intended for structures, which exhibit an unstable post buckling path and geometric imperfections. An example of a structure with an unstable post buckling path is a thin shell or arch. These structures have a snap-through type of buckling path. Budiansky and Hutchinson define the dynamic loss of stability of the plate by the point in which a small increase in pulse amplitude results in a rapid increase in plate's maximum deflection. This DLF can be determined by plotting the load versus displacement of a node in the buckled region and establishing the inflection point on the curve. Two examples of the inflection point, at the dynamic critical buckling load are illustrated in Figure 25 for plates with different degrees of geometric imperfections.

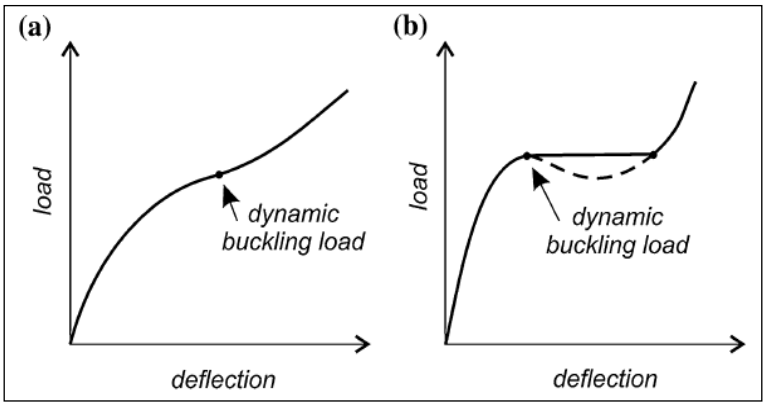

Figure 25 Budiansky-Hutchinson critical dynamic buckling load of plates with (a) large and (b) small geometric imperfections (reproduced from [46]).

The criterion developed by Ari-Gur and Simonetta is based on theoretical and experimental investigations of a plate, clamped on all edges, under a half-sine pulse load. The applied load F, and measured length shortening U, of the experimental tests are shown in Figure 26. The four critical dynamic load criteria defined are determined based on the deflection in the middle of the plate, W_m, load intensity, L_m, and pulse amplitude, F_m, or shortening, U_m.

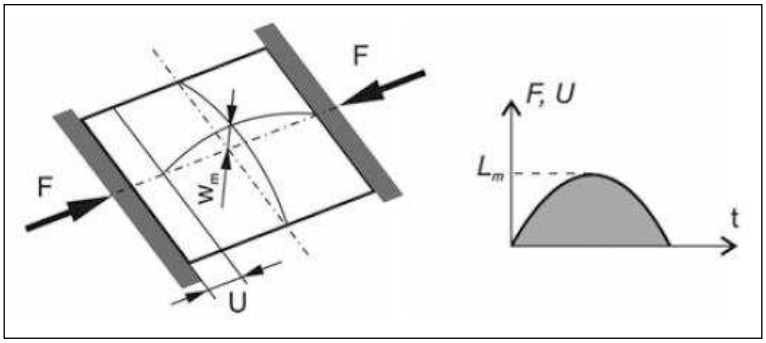

Figure 26 Applied forces F, length shortening U, deflection W_m (left) and applied load pulse (right) (reproduced from [46]).

The first of four criteria, which is based on deflection W_m and pulse intensity, states that dynamic buckling occurs when a small increase in load intensity results in a large increase in deflection. This criterion is quite similar to the criterion proposed by Budiansky and Hutchinson for structures with unstable post buckling paths. The deflection load intensity plot shown in Figure 27 (a) is the graphical representation of the first criterion.

Ari-Gur and Simonetta also found that the pulse duration and amplitude will change the deflection mode. This leads to the second dynamic buckling criterion, which states that dynamic buckling occurs when a small pulse load amplitude increase results in a decrease in deflection. The graphical representation of this criterion is plotted in Figure 27 (b).

The third criterion developed by Air-Gur and Simonetta is with respect to the force pulse and shortening, which is based on the reduction of stiffness due to large deflections. In the event, a small increase in force pulse results in a sudden increase in the shortening of

the loaded edges, dynamic buckling has occurred. This criterion is plotted in Figure 27 (c).

The fourth criterion is a function of the displacement impulse and shortening. This criterion states that dynamic buckling occurs when a small increase in shortening results in a change in the sign of the reaction R_m, at the edge of the plate. The loaded plate reaction distribution (Figure 28) is a sinusoidal shape with tensile forces resulting in the middle of the deformed plate. The resultant tensile force may be larger than the compressive resultant force which would indicate the occurrence of dynamic buckling.

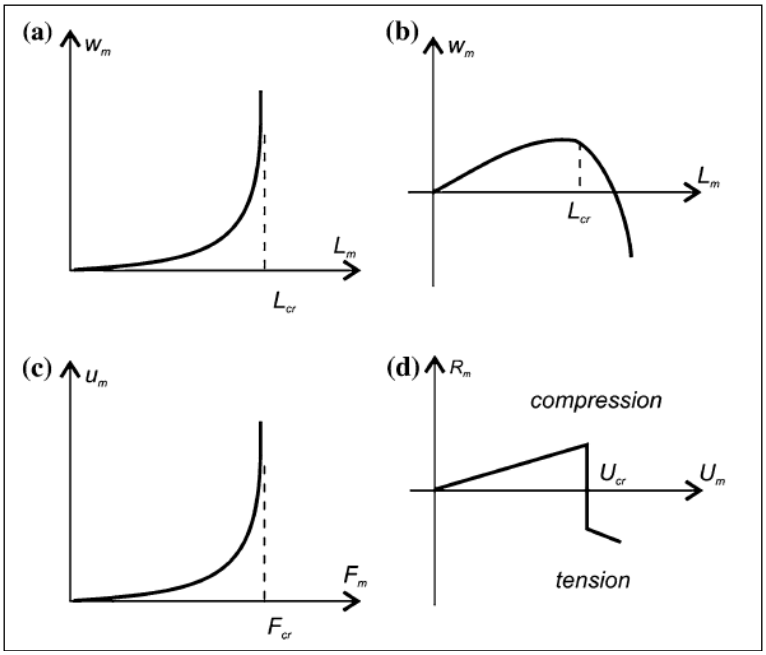

Figure 27 Graphical representation of the Ari-Gur and Simonetta criteria (reproduced from [46]).

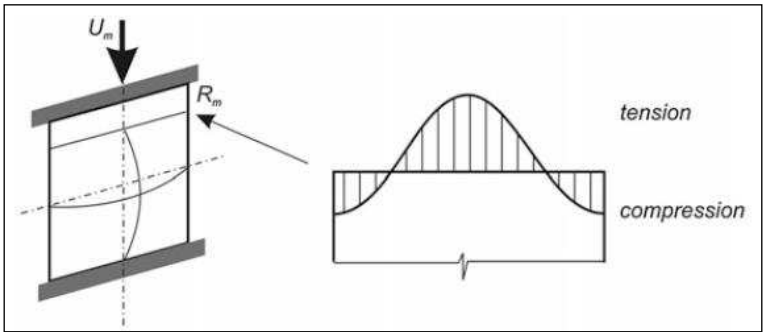

Figure 28 Plate edge reaction load distribution (reproduced from [46]).

The criterion developed by Petry and Fahlbusch is based on the theory that the Budiansky-Hutchinson criterion is overly conservative, since the full capacity of the plate structure is not used. According to the Petry-Fahlbusch criterion, structures with a stable post-buckling path should have a critical dynamic load determined by the stress state. A structure under pulse loading is considered dynamically stable if the equivalent stress is less than or equal to the limit of stress at any time and location. As for the choice of limit stress, Petry and Fahlbusch suggested the material yield strength.

A detailed summary of the works of Petry and Fahlbusch is described in [66], which investigated the application of a stress failure criterion to determine the DLF of isotropic plates subject to in-plane impact loads. In that work, the criterion was used to determine the effects of limit stress, shock function, geometric imperfections and dimensions on the DLF. A FORTRAN code was developed to solve the plate differential equations of motion using a fourth order Runge-Kutta method. The transverse deflection of the plate midpoint was used to evaluate the critical buckling load. Petry and Fahlbusch found that dynamic loads significantly higher than the static buckling load may be experienced, if the duration of the applied load was sufficiently short. For their investigation, Petry and Fahlbusch [66] consider a dynamic response as stable if the effective stress in the plate does not exceed the material yield stress. Using this failure stress criterion, it was determined that a wide range of load durations, near the period of transverse motion, result in a DLF less than unity. The influence of shock pulse shape was also evaluated for sinusoidal, rectangular and triangular pulse shapes. It was found that the DLF was sensitive to the rise-time of the pulse shape, so long as the total impulse remained constant. An increase in load rise-time results in a shift of lowest DLF to a lower pulse duration.

The size of the geometric imperfection was found to directly influence the DLF. An increase in imperfection amplitude resulted in lower DLF for short pulse durations. The effect of plate thickness on DLF was found to be minimal for longer pulse durations; however, an increased sensitivity to plate thickness was observed at short pulse durations. The limit stress of the loaded plate had very little influence on the DLF. To assess the

influence of stability criterion on the DLF, the Budiansky and Hutchinson criterion (i.e., the maximum gradient of deflection with respect to load), and the proposed stress criterion were applied to a plate with a pulse duration equivalent to the transverse vibration period. The failure stress criterion applied in the study suggests a critical DLF approximately twice the DLF determined by the Budiansky and Hutchinson criterion.

3.3 Early Stress Wave Interaction and Dynamic Buckling

The experimental and theoretical work of Abrahamson and Goodier [1] focused on how the axial compressive stress wave and material stress-strain relationship influences the dynamic buckling behaviour of axially loaded rods. The mild steel solid and hollow rods were loaded axially by a high velocity impactor which caused the rods to buckle and develop a thickened proximal end. Through high speed photography, Abrahamson and Goodier were able to determine the stress wave interaction during the pre-buckling, buckling and post-buckling phases. It was found that due to the sustained plastic flow, axial strains (up to several percent) developed in the proximal end up to a length equivalent to the time taken for the elastic wave to travel the length of the rod to the free end and reflect back to the loaded end as an elastic unloading wave. The wavelength of the plastic flow stress was observed in the thickened proximal end. The thickened proximal end proved to be a result of the lower plastic strain-hardening modulus at the high strain values experienced during plastic axial compression. Abrahamson and Goodier also found that the flexural motion of the impacted bar is developed as a result of the stress and strain amplitude along the bar at position B' (see Figure 29), lagged behind stress and strain amplitude of position C'. Position B' and C' represent the inside and outside diameter of the impacted rod, respectively. Due to their relative positions on the impacted rod position C' develops larger strains, and thus, creates more displacement than in the inner surface B' of the buckled column.

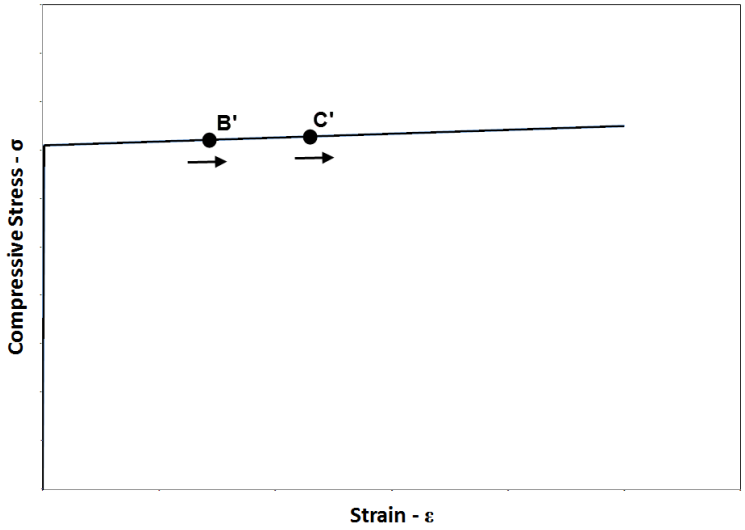

Figure 29 Stress-strain diagram for an impacted bar inside position *B'* and outside position C' (reproduced from [1]).

In addition to the experimental investigation, Abrahamson and Goodier [1] developed and solved the differential equations of motion. The number of buckled half waves and amplitudes were in good agreement with the experimental observations. They also noted that difficulty was encountered in the determination of the buckling waves within the plastic flow zone.

Experimental tests were conducted by Florence and Goodier [24] to confirm their numerical response using number of buckling half waves and percent longitudinal compression. The experimental tests projected 6016-T6 and 2024-T3 Aluminum cylinders against a rigid plate and measured the cylinder shortening and number of half waves developed. By assuming a constant impact velocity, the dependence of displacement and velocity perturbation amplitude on the harmonic number was determined by solving the equations of motion with and without inclusion of strain-hardening modulus. The harmonic number resulting in the largest displacement or velocity perturbation amplification was considered as the mode of buckling. The buckling mode determined from the velocity perturbation amplification was found to have better agreement with experimental results. The strain-hardening modulus was found to have little effect on the number of developed half waves. This was presented as a result of a

restoring moment that was present in the column, even though the strain-hardening modulus was 0 MPa.

3.4 Finite Difference Method

The research conducted by Hayashi and Sano [29], [30] evaluated the accuracy of the beam equations of motion to determine the dynamic buckling behaviour of initially bent (half-sine wave) elastic bars subject to low and high velocity impact. In the first report by Hayashi and Sano [29], the experimental mid-span axial force was compared to the calculated values by solving the Bernoulli-Euler beam equations (using the finite difference method) for low impact velocities (3.1 cm/s). The experimental tests were conducted on different beam slenderness ratios, imperfection amplitudes, striking masses and striking velocities. For each of the tests, the mass was free to rebound after initial contact and strike repeatedly until coming to rest. The repeated striking behaviour was also included in the numerical calculation and yielded good agreement for the first five impacts. In the second report by Hayashi and Sano [30], good agreement was found between the experimental and numerical deflected shapes of the impacted bar that were subjected to high velocity impacts (2.45 to 10.0 m/s). The variation in experimental tests was in the impactor velocity with the slenderness ratio and impacted mass remaining constant. The deflected shape was calculated numerically by solving the Timoshenko beam equations of motion using the finite difference method. Some observations from the experimental tests included:

- High velocity impacts develop higher buckling modes.
- Higher buckling modes are a result of the bars axial inertia.
- Local buckling at the proximal end quickly reduces axial force in the bar and develops a tensile wave towards the distal end.
- Increase in impact velocity decreases the buckled wave length.

The 1982 experimental and theoretical work by Ari-Gur *et al.* [10] was intended to determine the parameters and their effects on the dynamic buckling load of slender columns. The experimental tests included the axial impact of thin rectangular bars with varying initial imperfection and slenderness. Analytically, the bar deformation was

calculated by solving the Rayleigh-type beam equations of motion using the finite difference method with the assumption that the material remained elastic. Several observations were made as a result of the analytical and experimental studies, which include:

- The maximum axial strain in the bar is inversely proportional to the magnitude of the initial imperfection.
- There is a significant decrease in static buckling strain for slender columns relative to the moderate decrease in dynamic buckling strain, which results in an increase in DLF with increased slenderness.
- For all loading durations, the DLF is always greater than or equal to unity.
- It is important to include inertial effects in dynamic problems.
- A change in material density may result in a change in dynamic buckling strain.
- The stress wave propagation velocity, material density and bending stiffness of columns have a secondary effect on DLF.

The perturbation method was applied by Pedron and Combescure [65] to evaluate its application to submerged stiffened cylindrical shells subject to transverse shock loading. The cylinder was considered to be infinitely long, stiffened circumferentially and axially. The shock wave was assumed to be planar with amplitude equivalent to the sum of the incident and radiant pressure which included fluid-structure interaction effects. The perturbation method was used to determine the critical buckling mode. The study was limited to impulsive loads similar to the duration of shell modal period. It was observed that the impulse and peak pressure directly influenced dynamic buckling. The study was limited to the elastic response of a cylindrical shell.

The dynamic pulse buckling of composite rectangular plates was investigated by Ari-Gur and Simonetta [11]. The goal of their research was to determine how the anisotropic material properties would affect the DLF. Similar to the previous studies, a lateral initial geometric imperfection was applied in the longitudinal and transverse directions, with a half-sine pulse shape. The loaded plate was 1 m square with initial geometric imperfection amplitude of 25% of the plate thickness. The dynamic equations of motion

were solved using the finite difference method for multiple load durations ranging from 5 – 160 ms. This range in load duration covers the impulsive, dynamic and quasi-static load durations since the plate fundamental periods ranged between 40-60 ms. The study found that the deformation of the plate, relative to the peak loading was different for the different load durations. The peak deflection is obtained after the load peak is reached for small amplitude pulses. For long duration loading (quasi-static), the peak displacement and load arrive at roughly the same time. The peak deflection under dynamic pulse durations occurs before the load is released. The study found that at low pulse loads the lateral deflection increases as the stiffness of the plate decreases. This is contrary to what was discovered under high pulse loads. The plate tends to stiffen non-linearly due to in-plane tension until the dynamic buckling load is reached and the lateral displacement increases suddenly. The buckling load for loading durations greater than the fundamental loading period and less than the quasi-static duration is lower than the static buckling load. The findings of the finite difference method were compared to those determined from a finite element analysis using ANSYS and were within 15%.

3.5 Application of Galerkin Method

The Galerkin-type solution to the equations of motion was used to investigate the effects of axial stress waves on dynamic buckling of axially loaded elastic-plastic beams by Lepik [47]. The numerical study evaluated the dynamic buckling of a beam loaded instantaneously with infinite duration. The Galerkin-type of solution was applied to solve the following cases: elastic wave propagation and reflection, elastic wave propagation and part elastic part plastic reflection, and elastic propagation and plastic reflected. The result of numerical analyses revealed that the stress waves have a negligible effect on the final buckling form.

The Galerkin method was also employed by Bich *et al.* [13] to solve the equations of motion of an axially loaded stiffened functionally graded cylindrical shell. The load was applied as a step loading within an infinite duration. For this type of loading, the critical load was considered to be the amplitude of the step load to cause dynamic buckling. Bich *et al.*. found that the load-displacement curve for imperfect shells did not clearly define

the dynamic buckling load however the contrary was found for perfect shells. The axially loaded cylindrical shell in that study was stiffened with rings and stringers and analysed for different combinations of each. The study found that by increasing either the number of stringers or rings, the DLF increased. By combining stringers and ring stiffeners, a greater increase in DLF was achieved. The study also investigated the relative influence of the geometric parameters, radius and shell thickness. For thin cylindrical shells, the stiffeners had an increased effect on the DLF and could have been characterised by a steeper load-displacement slope in the unstable region of the curve.

3.6 FINITE ELEMENT METHOD

Prior to the 1989 research of Weller *et al.* [84], the structural dynamic buckling behaviour under finite load duration was exclusively investigated with respect to beam and column response. Weller *et al.* numerically evaluated plates and beams subject to in-plane half sine wave load pulses using the ADINA finite element code. The study evaluated the influence of initial geometric imperfections and impact duration. For this study, the initial plate imperfections were modeled as a half sine wave in the longitudinal and transverse directions and the dynamic load had a half sine pulse shape. The in-plane buckling load of the thin plate was compared to the experimental tests by measuring the central lateral displacement. The application of the modified Donnell technique to the in-plane plate buckling DLF calculations was also investigated and found that the required imperfection magnitude was too high. As a result, a modified Southwell method was employed to determine the DLF. The numerical and experimental studies revealed that the reduction in load duration, less than the fundamental period of free vibration, increased the DLF. For load durations longer than the fundamental period, the DLF was less than unity. In terms of the initial geometric imperfection, the DLF is reduced to less than unity at large imperfection magnitudes.

Further studies on the application of the Modified Donnell Technique were completed by Abramovich *et al.* [2] in 1989. Their study evaluated the Donnell and Southwell techniques for calculating the DLF from experimental and analytical tests of in-plane dynamically loaded composite plates. The ADINA finite element code was used to carry

out a parametric study to evaluate the influence of initial geometric imperfection, gravity and boundary condition effects on the critical buckling load. A result of the Abramovich *et al.* work was the development of a consistent method of determining the DLF where the initial imperfections were large and unknown. The technique has also been shown to accurately determine the DLF where boundary conditions are poorly defined. The parametric study revealed that small geometric imperfections (20% plate thickness) were found to be similar to modelling the plate as a shallow shell, however at large (70% plate thickness) imperfections the plate can no longer be represented as a shallow shell.

The application of the modified Donnell technique was extended to the calculation of DLF of dynamically loaded in-plane composite plates by Abramovich and Grunwald [4]. Their study used the bending and membrane compressive strain relationship in the plate to determine the critical DLF for various plate aspect ratios, boundary conditions, load amplitudes and load durations. The bending and membrane strains were determined by bonding two strain gauges to either side of the plate at the same location. Before the dynamic tests were carried out, the static buckling load was experimentally determined by applying a quasi-static increasing load until elastic bifurcation occurred. The natural frequency was also determined before the axial impact tests by striking the plate and measuring the elastic strain response. The dynamic test impact load amplitude was varied by increasing the mass drop height and the load duration was modified by changing the impactor mass and applying a rubber layer at mass impact position. The experimental dynamic tests found that when the loading duration matched the fundamental period of lateral vibration, a DLF of less than unity was observed for one series of composite plates. By decreasing the load duration, the DLF increased above unity as expected.

The works completed by Su *et al.* [76] [77] use a simplified four-hinge, four compressible bar model to determine the effects of strain-rate, inertia and elasticity on the impact energy absorbing properties of a structure. The simple model represents a simply supported column impacted axially by a lumped mass. The structure responds in bending at the hinges and in axial compression in the bars. The equations of motion were solved to determine the axial force and bending moment during the dynamic response (loading,

unloading and reversed loading) using the 5th order Runge-Kutta method. For this study, the material model was assumed to be elastic-perfectly plastic. The dynamic behaviour of the model was different than the static behaviour with and without strain-rate effects. The model is considered inertia sensitive since it was found to be more sensitive to impacting mass than initial velocity, initial imperfection size or effective hinge length. The numerical studies were found to agree well with experimental data for strain-rate insensitive materials and disagree with strain-rate sensitive models. The rate-dependence study [77] applied the same elastic perfectly-plastic, four-beam four-hinge simplified model as the inertia and elasticity [76] study. The strain-rate effects were accounted for by applying the Cowper-Symonds rate law to the material constitutive model. The study found that the peak load on the system increased, and the structural response time decreased when rate-effects were included. The strain-rate dependence increased the elastic contribution to the energy partition, which directly influences the early model response. The work of Su *et al.* [76] found that strain-rate dependence and inertia are equally significant in the dynamic response of the structure. Although the strain-rate dependence and inertia are equally significant, the influence of mass on the final displacement of strain-rate dependent and independent models is greater than the influence of initial velocity. The initial velocity was found to affect the peak force more than the mass. By adjusting the mild steel Cowper-Symonds coefficients to D=300s^{-1} and q=2.5, better agreement with experimental tests were achieved.

The work by Kounadis *et al.* [45] presented a lower and upper bound limit of dynamic buckling load. The method was developed for a multi degree of freedom system subject to impact by a lumped mass with transverse and axial inertia included by applying the law of impulse momentum.

Abramovich and Jones [3] experimentally examined the influence of geometric and material parameters on the transition from global buckling to progressive collapse. Their work focused on the buckling of stocky (D/t>=40) and slender (D/t>=100) tubular columns (square and cylindrical) under static and dynamic axial loads. The global bucking refers to the classical three-hinge bending response and progressive folding

refers to the local rippling effect. The graph in Figure 30 maps the regions governed by global bending, progressive folding and combined (transition) global and progressive collapse as a function of column length (L), side wall height (C) and wall thickness (t) under equivalent impact loading.

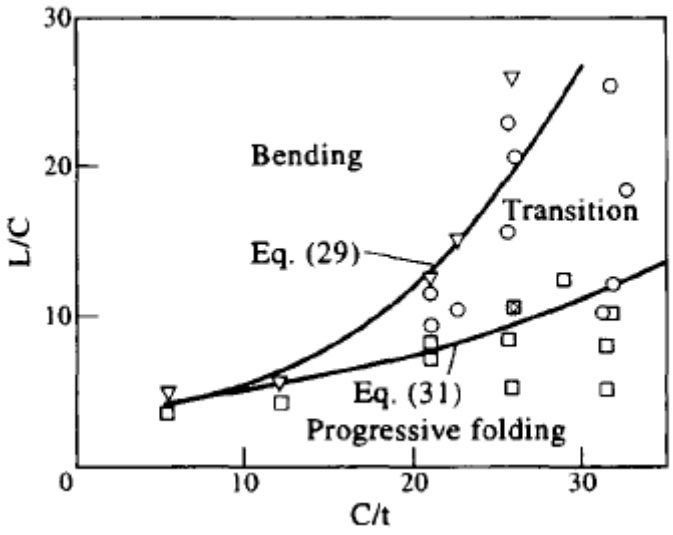

Figure 30 Relationship between dynamic buckling behaviour (reproduced from [3]).

The high speed footage of the drop hammer tests were used to determine the dynamic buckling process which was described as a function of stress wave interaction. The stress wave interaction produces a high-impact pressure that leads to plasticity of the cross section. This plastic cross-section is what develops the collapse mechanism at the proximal end of the column. The influence of lateral inertia forces was found to be negligible for local progressive collapse; however, the inertia may not be neglected under global bending. Generally, an increase in impact velocity resulted in a transition from global buckling to progressive collapse.

The dynamic shear loading of cylindrical shells as a result of seismic events was investigated by Michel *et al.* [58]. In their study, a shell with radius to thickness ratio of 450 and radius to height of one was experimentally tested using a shaker table, and numerically analysed using axisymmetric solid elements with ABAQUS. The stiffness of the cylindrical shell was evaluated with varying levels of geometric imperfection

amplitude when subject to shear, pressure and axial compression loading. The geometric imperfection shape was affine to buckling modes 1 to 10. It was found that shear buckling was less imperfection sensitive than buckling due to pressure or axial loading. The shear load from the experimental tests was plotted with respect to displacement to determine the static buckling load. The dynamic experimental tests and numerical analyses confirmed that combined buckling and vibration modes resulted in a critical dynamic buckling load at 70% of the static buckling load. This study provides an example of the impact of closely spaced buckling and vibration modes on the DLF.

The application of the perturbation method in dynamic elastic pulse buckling was analysed using finite element and finite difference modelling by Kenny *et al.* [41]. The study verified the requirement of geometric imperfections in order for dynamic buckling to occur in an axially loaded beam. The finite difference evaluation of the buckling problem assumed a constant axial stress state and the effects of axial inertia and deformation were neglected. The finite element method, however, accounted for the axial inertia and deformation while determining the stress wave propagation during the impact event. The study compared the analytical characteristic transverse deflections with those calculated by the finite difference and finite element methods of an axially loaded beam with a half sine global imperfection. The theoretical transverse deflections were 3-5 orders of magnitude larger than the numerical finite difference and finite element methods. The influence of random geometric imperfections was also evaluated by numerical methods and found to have a larger effect on the buckling response than the global deformations. The FE analysis evaluated the application of 2D axisymmetric solid elements and the Euler-Bernoulli beam element formulation to determine the unbounded growth of transverse displacements. This parametric study found that the 2D solid elements required a significant level of discretization, as well as the inclusion of geometry and material non-linearity in order to replicate the transverse deflection. The beam element formulation was limited to the plane sections remaining plane after deformation.

The dynamic buckling behaviour of an axially impacted 2-plate system was numerically investigated by Webb *et al.* [81] using the finite element method. Their study compared the experimental and theoretical work of Tam and Calladine [78] with the numerical analysis of the same axial impact experimental tests using 2D-plane strain elements. The numerical analyses results agreed well with the experimental results using Cowper-Symonds strain rate law with coefficients D=40 s^{-1} and P=5. The finite element study by Webb *et al.* proposed dividing the plate buckling behaviour into phases governed by the stress state and deformation. A phase diagram is shown in Figure 31 to illustrate the velocity and deformation characteristics associated with each phase. The "stress wave zone" is considered pre-phase I, which accounts for the elastic wave propagation and reflection. The reflected stress wave is a function of the impacted mass and velocity and may be beyond the yield strength. Once the stress wave has travelled the length of plate and reflected, phase I begins with the "squashing zone" and ends at the arrival of the "transition zone". The "transition zone", "zone of work" and "elastic recovery zone" are lumped into phase II, where the bulk of the energy dissipation occurs during rotation of plastic hinges. The numerical results were in good agreement with the findings of Tam and Calladine [78].

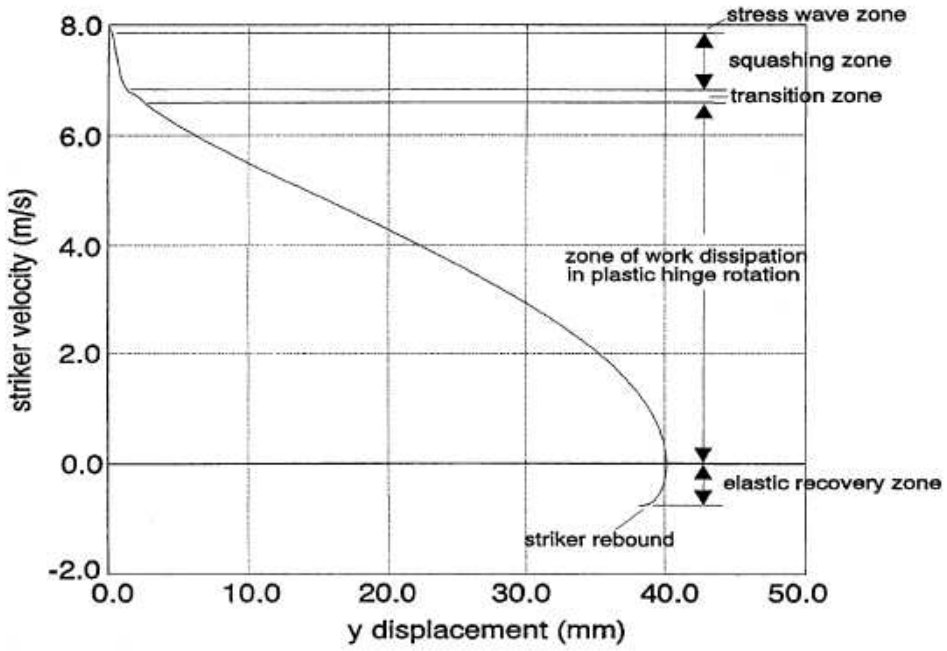

Figure 31 Phase diagram relating striker velocity with out-of-plane deformation (reproduced from [81]).

The dynamic buckling response of fluid-solid slamming of plates was experimentally investigated by Cheong *et al.* [16]. The experimental test axially loaded the mild steel plate by dropping the test fixture from height to a pool which loaded the rigid bottom plate of the fixture. The fixture had a large mass above the plate, fixed top and bottom boundary conditions with variable (fixed, pinned and free) plate side conditions. After the plates buckled, they were continually loaded with varying impulse loads to determine their post-buckled capacity with varying plate side boundary conditions. The post-buckled plate transverse bending was found to increase with increased impulse loads, resulting in increased lateral membrane strain and reduced longitudinal strain. A plastic collapse criterion was developed from this behaviour as follows: when the transverse maximum effective bending strain sharply increases while the lateral effective membrane strain rapidly decreases as impulse increases. The numerical study found that different side boundary conditions induced different plastic collapse mechanisms. The strengthening of the boundary conditions of the plate was found to have a significant influence in increasing the critical buckling impulse.

The dynamic buckling of stiffened cylindrical shells under axial load was numerically and experimentally investigated by Yaffe and Abramovich [86]. The purpose of their study was to determine if a DLF below unity would develop in complex stiffened structures when the load pulse duration would become equivalent to the fundamental period of vibration. The experimental set up consisted of an externally stiffened cylindrical shell (length 200 mm and radius 120 mm) clamped between two loading plates with a dropped mass loading the upper plate. The dynamic response was measured using three pairs of strain gauges placed in the inside and outside of the shell plating. The numerical model was analysed using the ADINA code and consisted of a quarter symmetric cylindrical shell with two rows of shell elements between stiffeners and beam elements representing the stiffeners. Prior to the drop tests, the cylindrical shell was lightly impacted to determine the lowest bending frequency and a static elastic buckling test was performed to measure the static buckling strain. The experimental tests were not performed as expected due to a lack of repeatability in determining the load pulse duration. The numerical study found that the DLF was greater than unity at the period of

fundamental vibration. However DLF <1 occurred when the load period was normalized as:

$$T' = cT / 2a \quad \textbf{[39]}$$

where c is the sound speed in the cylinder material, T is the half sine-wave pulse duration, and a is the length of the cylinder. The study also found that the geometric imperfections had a significant influence on the dynamic buckling response.

The local buckling of circular tubes under bending was numerically investigated by Corona *et al.* [18] to accurately calculate the axial wrinkling wavelength which is directly used to determine the critical curvature of a member. The bifurcation modes historically over-predicted the buckling wavelength in experimental comparisons when using isotropic plasticity constitutive models. The work introduced Hill's quadratic anisotropic yield function, which had been shown to facilitate accurate calculation of the local axial buckling wavelengths and determination of the critical curvature of the section. In order to apply Hill's function, the user must experimentally determine the anisotropic constants (S_θ, S_r, $S_{x\theta}$) from axial, circumferential and hydrostatic pressure buckling tests. The stress-strain relationship should overlap in each test; however, if one assumes isotropic plasticity, a variation in the level of plastic strain may develop. The magnitude of the variation is the level of plastic anisotropy. By varying the anisotropic constants, the plastic variation will be eliminated, and the three stress-strain behaviours will overlap. A numerical parametric study was conducted to determine the influence of variations to S_θ, and S_r. The study found that the buckling wavelength increased when S_θ <1 and S_r>1 and decreased for S_θ>1 and S_r<1. The limit was found to have been directly influenced by the ovality of the member; it increased when S_r<1 and decreased when S_r>1. The paper concluded by suggesting that yield anisotropy, when present, should be incorporated in the bifurcation and post buckling calculations.

The elastic buckling of imperfection sensitive shells under uniform lateral pressure is numerically investigated by Sosa *et al.* [74], using the finite element code, ABAQUS standard. Their study applied a reduced energy approach to calculating the lower-bound elastic buckling loads. To determine the lower-bound buckling load, the membrane

energy contribution to the shell stability had been removed, since imperfection sensitive structures may lose membrane energy contribution when local imperfections are present. The classical bifurcation analysis included the membrane energy contribution, and therefore, had been labelled as an upper bound buckling load.

An experimental and numerical study was conducted by Lu *et al.* [53] on the response of liquid-filled cylindrical shells under impact loading. The intention of the study was to investigate the influence of material yield strength, wall thickness, length, and impact velocity on the energy absorbing characteristics. The study investigated impact test on aluminum, galvanized iron and stainless steel cylinders. The experimental test was setup such that a drop hammer impacted a load cell located on the top of the cylinder, with the load measured by the loading cell and water pressure measured by a pressure gauge fixed to the cylinder bottom. Generally, the tests suggested that the fluid pressure absorbed the majority of the impact force, thus, raising the impact resistance of the cylinder. The experimental tests were characterised in the deformation process by three stages: dynamic loading, dynamic buckling and elastic unloading. The sudden loading of the cylindrical shell caused oscillation of the impact force and internal pressure during the dynamic loading phase. The dynamic buckling and elastic unloading phases were associated with the development of buckling waves and a sharp drop in load and pressure, respectively. The buckling mode, impact force and pressure time histories from the experimental tests were used to verify the numerical model constructed in an LS-Dyna environment. The constitutive model used for the cylinder was linear elastic-plastic with Belytschko-Tsay shell element formulation. The water in the cylinder was represented using hexahedral elements defined as an ideal fluid with volume modulus of 1.37 GPa. The parametric study found that the impact force and internal pressure remain consistent for each impact velocity when the linear strain-hardening modulus is low. The loading duration, however, increased with an increase in impact velocity. For linear strain-hardening modulus greater than 1% of the elastic modulus, the internal pressure and impact force increased with an increase in impact velocity. The developed buckle wavelength was found to be independent of the impact velocity and yield strength. The number of buckling waves was found to increase with an increase in hardening modulus.

Lu *et al.* study [53] found that an increase in material hardening modulus increased the fluid pressure developed in the cylinder and impact force, however, the load duration subsequently decreases. Generally, the tests suggest that the water inside the cylindrical shell increases the stability of the structure and reduces the imperfection sensitivity.

The numerical study of Mania [55] investigated the influence of a viscoplastic constitutive model on the critical dynamic buckling behaviour of axially loaded plate columns. The critical buckling behaviour was evaluated using the axial pulse load amplitude to cause buckling. The study evaluated plate columns with closed sections using the finite element code, ANSYS. The isotropic and orthotropic material constitutive models were applied to columns with geometric imperfections. The geometric imperfection was applied as a fraction of the wall thickness (0.01, 0.05 and 0.1) in the shape of the first static buckling mode. The closed plate sections were represented using shell elements and subjected to a load in the form of a half-sine wave and a rectangular pulse load with duration equivalent to the fundament period of flexural vibrations. Mania's study assumed the column was constructed of either bi-linear isotropic and orthotropic mild steel (σ_y=100 MPa, E=200 GPa, E_h=2 GPa) with the dynamic response described by the Perzyna constitutive model. By including strain rate sensitivity, the DLF significantly increased for isotropic (29%) and orthotropic (40-60%) columns. The Budiansky-Hutchinson and Air-Gur Simonetta criterion were applied with similar strain rate sensitivity behaviours however the Air-Gur Simonetta criteria found marginally increased strain rate sensitivity when compared to the Budiansky-Hutchinson criterion. The orthotropic material model was found to be more strain-rate sensitive.

The work of Less and Abramovich [48] determined the dynamic buckling load of a stringer stiffened curved laminate composite panel. Using the ANSYS FE code, the curved composite panel (modelled using 8-noded shell elements) was loaded axially on the curved edge. The paper lists the steps for determining the dynamic load factor for different half-sine load amplitudes and durations. Firstly, the static buckling load was calculated using an eigenvalue buckling analysis. Then a modal analysis was carried out to determine the fundamental mode of vibration. Following the natural frequency

analysis, the equations of motion were solved using FE for the different load durations and amplitude. A geometric imperfection of 10% of the panel shell thickness in the shape of the static buckling mode was included in the panel model. The critical buckling load was then determined by plotting the lateral deflection of the shell (at the mid-span between stringers) as a function of the axial load. The DLF criterion of Hutchinson-Budiansky (i.e., when a small increment in load results in a large increase in lateral deflection) was used in this study. This study found that load durations near the fundamental local shell bending mode (in the shell section between stringers) resulted in a DLF less than unity.

Dynamic buckling of axially impacted cylindrical shells was investigated by Wei *et al.* [83] to determine the influence of material parameters on the buckled shape. The perturbation method was employed to determine the wavelength of the buckled shape, while varying the material density, specific heat, strain hardening modulus, strain-rate sensitivity, thermal effects, strain rate, mean shell radius and shell thickness. In addition to using the perturbation method, the finite element method (using MSC Dytran) was used to investigate the influence of imperfections on the low speed buckling behaviour of aluminum cylindrical shells. The authors explained the perturbation comprehensively as the method of determining the buckling modes by perturbing the deformed cylindrical shell by a very small amount. The deformed state was considered buckled if the superimposed perturbations grew as a function of time. Using this method, the wave number and initial perturbation growth rate were found to increase when the initial axial stress increased and hardening modulus decreased. The initial perturbation growth rate also increased when mass density decreased; however, the wave number and mass density varied independently. The maximum perturbation growth rate and wave number were dependent on the axial velocity and length of the cylindrical shell.

In their study, the shell buckling was not affected by the length to radius aspect ratio for the nominal axial strain rate. An increase in the strain hardening exponent, shell wall thickness and shell radius found to monotonically increase the half wavelength. A decrease in the half wavelength occurred when the applied strain rate, mass density and

thermal softening exponent were increased. The analytical perturbation method was compared to the experimental data of Florence and Goodier [24]; they found that the half wave number differed by less than 33%. This discrepancy between their calculated and the experimental wave number was attributed to simplification made to the perturbation terms, neglecting the geometric initial imperfections, assuming geometric axisymmetry and neglecting high-order strain terms.

The 3D shell-element model used to investigate the influence of geometric imperfections (30% thickness reduction) on the buckling behaviour assumed frictionless contact between the developed folds. By varying the random imperfections, the buckling mode remained the same; however, the deformed shape changed. The average axial load during the buckling action remained the same for 5 or 50 geometric imperfections (thickness variations). The peak axial load was larger for the model with 5 imperfections. Wei *et al.* [83] therefore, claimed that the energy absorbed by axial strain remained the same for different geometric imperfections.

Wei and Batra [82] continued the application of the perturbation method to determine the wave number and initial growth rate of thermo-viscoplastic cylindrical shells subject to impulsive radial loads. In that study the half wave lengths observed in the experimental work of Lindberg and Florence [49] was compared to those calculated by the perturbation method with good agreement. The analyses in the study used the Litonski-Batra thermo-viscoplastic relation to calculate the stresses for radially prescribed impulsive velocity where elastic deformations are considered negligible, and no strain-rate reversal was assumed to have occurred until the buckling modes had fully developed. The study investigated the strain hardening and strain-rate hardening independently. An increase in the strain hardening modulus was found to decrease the initial perturbation growth rate and the number of developed half waves. The initial perturbation growth rate and number of half waves tended to increase quickly when the material viscosity increased from a small value; however, they increased slowly when the viscosity was initially large. Strain-rate hardening materials were determined to increase the perturbation growth rate and wavelength at a lower rate than the strain hardening only materials. Since the

buckling mode may change throughout the deformation process, the perturbation method is not recommended to be used for computing the energy absorbed in post-buckling deformations. This method also ignores the thickening effect, which provides additional stability at high prescribed velocities. By neglecting the thickening effect, the computed buckling loads are considered highly conservative.

3.6.1 Stress Wave Propagation

The local (short wave) and global (long wave) dynamic buckling of axially impacted cylindrical shells was analytically and numerically investigated by Xu *et al.* [85]. The study focused on the influence of the longitudinal stress wave propagation, prior to end reflection, on the dynamic buckling behaviour. The dynamic buckling load and shape were determined by calculating the eigenvalues and eigenvectors of the Hamiltonian system of equations. The global modes were characterised by bending and ovalization of the shell, while local modes exist as axial ripples in the cylinder shell. By calculating the normalized critical buckling load for several wave propagation times, the local, global and combined buckling modes may be determined from Figure 32. The three curves, which do not converge at early stage wave propagation times, are the global buckling modes and the curves corresponding to the short propagation times which are the local modes. Time, *T,* where the two sets of curves intersect corresponds to the wave propagation time at which the combined global and local buckling mode is developed. From Figure 32 one may conclude that local modes typically developed at short wave propagation times, and global modes develop at later propagation times.

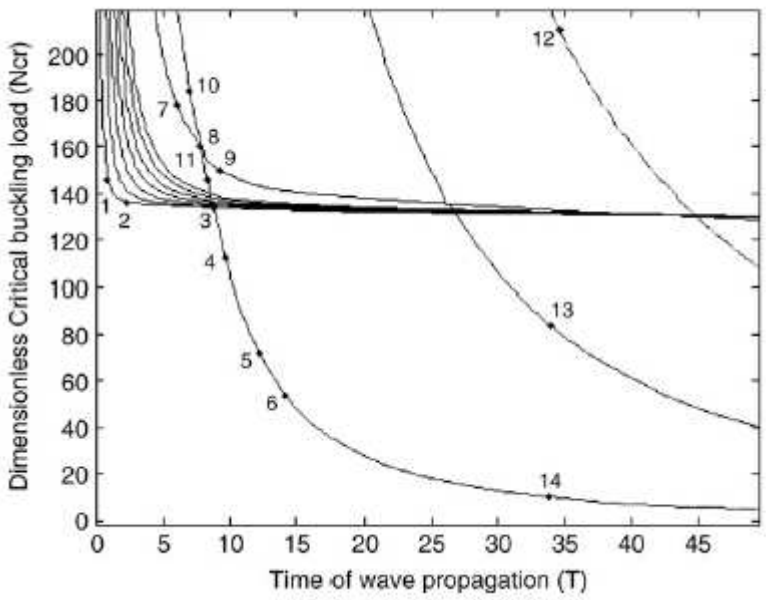

Figure 32 Critical buckling loads as a function of wave propagation time (reproduced from [85]).

Elastic buckling of rings subject to high loading rates of a hydrostatic pressure pulse was investigated by Putelat and Triantafyllidis [67] using the Hamiltonian method. The study also briefly employs the frozen coefficient analysis method to determine the quasi-static buckling modes. The analysis calculated the hoop, bending and shear potential energy components for multiple rings with different slenderness values. By plotting the potential energy components as a function of time, the onset of instability is indicated by the peak hoop potential energy. The study found that small pressure loading rates resulted in the global modes governing the deformed shape, and the local modes governing the deformed shape under large loading rates. In terms of stress wave propagation, Putelat and Triantafyllidis determined that the global buckling mode occurred after the axial and shear stress waves traveled around the circumference of the ring under small loading rates. Under large loading rates, localized buckling developed. Axial stresses traveled at the longitudinal wave speed with the shear and bending stress waves travelled at the bending wave speed.

The collective works of Karagiozova and Jones [34] heavily relate the dynamic buckling of axially loaded cylindrical shells to the stress wave propagation characteristics.

Karagiozova and Jones numerically investigated the influence of elastic and plastic stress waves on buckling initiation. The numerical study analysed axially impacted cylindrical shells with different geometric characteristics, impact velocities and impact methods. A discretized axisymmetric model of the cylinder was utilized in that study. The material constitutive equations used the Tresca yield criterion, since the von Mises yield criterion predicted higher critical loads than those observed in experimental tests. Since the Tresca yield criterion was used, there were three stress wave propagation speeds: one elastic and two plastic (fast and slow). The fast and slow plastic wave speeds corresponded to small and large plastic deformations respectively. The numerical calculations were verified by comparing the axial deformation and deformation duration with those from experimental tests of Florence and Goodier [24] and Murase and Jones [61]. The verification analyses included low (6.26 m/s) and high (125.3 m/s) speed events as well as stationary cylinder and projected cylinder impact tests with good agreement. The analysis of the projected cylinder found that buckling developed in zones of sustained plastic flow, where the slow plastic wave propagated. This buckling lasted until partial elastic unloading occurred with the development of a wrinkle (radial displacement). The stationary cylinder analyses found that a uniaxial stress state developed from the propagation of the faster plastic wave along the length of the cylinder. The wrinkling at the impacted end was resisted by the cylinder radial inertia; however, the stationary end buckled from the reflected elastic wave (created a slow plastic wave). These numerical studies have shown that at early times, the deformation is governed by the stress wave propagation and on structural response at later times. If the cylinder is thick enough, the lateral inertia would suppress the development of a wrinkle. Thin cylinders would wrinkle due to the lack of radial inertia. If the cylinder is moderately thick the small wrinkles developed by the elastic and faster plastic waves would be amplified by the slower plastic waves.

The influence of stress waves on the buckling type of axially loaded cylindrical shells is investigated numerically by Karagiozova and Jones [35]. The stress waves developed in the axisymmetric models are analysed for different cylinder geometric characteristics (thickness-radius and radius-length ratios) and material properties (steel and aluminum). A bilinear stress-strain relationship is assumed for steel and aluminum materials. The

strain-rate sensitivity in steel cylinders was accounted for using the Cowper-Symonds equation (D=16,640 s^{-1}, q=3.53). The strain-rate sensitivity in aluminum cylinders was effectively ignored. The study represents the cylindrical shell using solid axisymmetric elements employed in the ABAQUS Standard. The dynamic buckling behaviour of the cylindrical shell is characterized by dynamic plastic buckling and dynamic progressive buckling. Dynamic plastic buckling is developed when small wrinkles are observed along the length of the cylinder. The development of shell folds is considered as dynamic progressive buckling. The dynamic buckling response of the aluminum cylindrical shells suggests that a decrease in thickness and radial force will increase the likelihood of dynamic progressive buckling. It has also been shown by Karagiozova and Jones that dynamic buckling type is directly dependent on the strain hardening modulus and shell geometric parameters. A decrease in the slope of the strain hardening modulus decreases the plastic wave speed subsequently increasing the time to travel across the length of the shell.

Cylindrical shells with a low hardening modulus value allow for radial displacements to increase in the region of plastic flow, and develop progressive buckling, which in turn results in elastic unloading and stopping the propagation of the plastic wave resulting in dynamic progressive buckling. The aluminum impact analyses verified that the decrease in radial inertia decreases the buckling resistance and leads to dynamic progressive buckling where elastic unloading halts the plastic wave propagation. The axial impact analyses of steel cylindrical shells revealed that progressive buckling developed without the presence of elastic unloading, which typically occurs during progressive buckling of aluminum cylinders. Generally, dynamic plastic buckling of strain-rate insensitive shells occurs when there is sufficient radial inertia to sustain the plastic flow throughout the length of the cylinder and avoid elastic unloading. Dynamic plastic buckling, however, does not occur in strain rate sensitive shells due to the propagation of plastic strains at the elastic wave speed. An effect inherent to strain-rate sensitive materials is the increase in plastic strain, although the stress may be decreasing. This causes multiple plastic strain wave magnitudes to propagate along the cylinder and localize, thus, causing local buckling. The axial impact of aluminum and steel cylinders, insensitive to strain-rate

effects, identical geometric properties and equivalent E_h/E ratios were analysed. It was found that the increased radial inertia of the steel cylinder developed plastic buckling and the aluminum cylinder with lower radial inertia developed progressive buckling. For dynamic plastic buckling to develop, it requires sustained axial plastic flow without strain localization. The localization of strain results in dynamic progressive buckling. The influence of loading type on the type of dynamic buckling was also assessed by Karagiozova and Jones [35] by impacting a stationary cylinder with a mass and also by projecting a cylinder with a fixed mass into a rigid wall. The test results suggested that the buckled shape of the cylindrical shell was dependent on the initial kinetic energy of the system and not on the mass of the impactor.

The sensitivity of the bucking response to inelastic material properties and approximations was numerically assessed by Karagiozova and Jones [37]. It is important to note that the complexity of the dynamic buckling response is generally beyond analytical solutions. The focus of the aforementioned publication was to determine the influence of plastic material property approximation and axial inertia on the initiation, development and pattern of dynamic buckling. Several different hardening modulus approximations were investigated including low slope, high slope, piecewise linear and strain-rate sensitive. The Cowper-Symonds expression was used to approximate the strain-rate sensitivity with aluminum constants of D = 1,288,000 s^{-1} and q=4. An axisymmetric, 8 node solid element representation of the stationary impacted column, without geometric imperfections, was analysed using the ABAQUS Standard. The study found that the hardening modulus approximation had an influence on buckling shapes with an increase in impact velocity. In terms of the plastic wave speed, the von Mises stress wave was found to be the fastest, followed by Tresca and then uniaxial. The study results suggest that axial inertia also has a significant influence on the dynamic buckling response of axially impacted cylindrical shells. Impacted cylindrical shells with a high strain hardening modulus resulted in a faster plastic wave propagation reaching the cylinder end, before the lateral deflection could develop. This was contrary to the findings observed when a lower hardening modulus was considered, which resulted in the

development of dynamic progressive buckling before the plastic wave reached the distal end.

The piecewise hardening modulus resulted in two plastic wave propagation speeds with larger strains propagating the slowest. Axially impacted cylindrical shells with strain-rate sensitive hardening modulus were characterized by plastic strains travelling at elastic wave speeds, increasing with time and varying in magnitude. This plastic strain propagation behaviour resulted in strain localization, thereby developing dynamic progressive buckling. The numerical study also suggested that progressive buckling would always occur unless there is sufficient energy (lateral inertia) to provide buckling resistance. Axial inertia effects on the dynamic buckling response were investigated by impacting cylindrical shells of different lengths. The analysis results proved that the number of cylinder folds did not depend on the cylinder length; however, they would be dependent on the material properties. It has been noted that the peak impact load develops as a result of the stress discontinuity at t=0 and is directly dependent on the initial kinetic energy. The study findings suggested that the critical dynamic load is directly dependent on the shell radial inertia and the capacity of the cylinder to absorb the kinetic energy through compression and folding.

Karagiozova [36] extended the aforementioned stress wave propagation works on cylindrical shells [34], [35] to include the axial impact of square tubes. The stress wave propagation of square tubes must consider a plane stress state (include shear stress wave) instead of a biaxial stress state, which assumes shear stress can be ignored. Additional restraint provided by the corners of the square tubes generates the shear stress waves. This study assumes the square tube is constructed of a material which is strain-rate insensitive, has isotropic hardening and follows the von Mises yield criterion. Karagiozova [36] describes a single elastic and two plastic wave speeds (i.e., one fast and the other slow), which are dependent on the stress state and propagation direction. Fast plastic waves can propagate near the elastic wave speeds, while slow waves are directly related to the ratio between the hardening and elastic moduli. A decrease in the ratio leads to a decrease in the slow plastic wave propagation speed. The shear stress wave,

however, behaves in a more complex manner. An increase in the shear stress always decreased the slow plastic wave speed. It may or may not, however, increase or decrease the fast plastic wave speed.

The intention of the study in [36] is to understand plastic zone propagation speeds. By varying the plane stress state, it was shown that the slow plastic waves propagate in an elastic-plastic medium at speeds higher than the uniaxial stress wave. The study also suggests, based on theoretical calculations, which lower plastic stress wave propagation speeds result from high impact velocities. To verify the findings, a numerical analysis of an aluminum plate fixed at one end with rotational edge constraints (to replicate a square tube) and impacted at the other was completed using shell elements. The analysis results also found that the plastic wave speed propagated faster than the uniaxial plastic wave in a non-uniform fashion (caused by the shear stress along the edge boundary). The numerical studies also agreed with the theoretical slow and fast plastic wave propagation speeds. By analysing the buckling behaviour numerically, it was found that the plastic zone propagation was directly related to the buckling deformation initiation. This implies that understanding stress wave propagation is crucial to the analysis of the buckling deformation pattern of structures subject to in-plane dynamic loads.

The work completed by Karagiozova [36] on theoretical elastic and plastic stress wave propagation speeds in axially impacted square tubes is investigated experimentally and numerically by Karagiozova and Jones [37] in the second part of the two part publication. A quarter symmetric shell model of the square tube was analysed using ABAQUS Standard with a bilinear plastic aluminum material definition. To initiate axisymmetric buckling behaviour, 0.1 mm out-of-plane geometric imperfections were modelled along the square face edges. An identical set of impact analyses were performed on geometrically equivalent (length and cross sectional area) cylindrical shells to understand the influence of shape. At low impact velocities local deformations developed with the rest of the tube undeformed. In contrast, the higher impact velocities developed dynamic plastic buckling with small wrinkles throughout the square tube. An axial compression phase and a bending phase characterized the dynamic buckling of the tubes. The

compression phase is of particular importance to the buckling behaviour of small b/h ratios and high strain hardening materials since the bending rigidity is low in the remaining elastic portion of the tube. Similar to part one of the publication, the numerical study found a strong correlation between the shear stress in small hardening ratio and slow plastic wave speed. Several square tubes with varying b/h (where b is the side face width and h is the face thickness) ratios were subject to axial impact and analysed numerically. The results of the study suggest that the axial and lateral inertia of the shell influence the initial wrinkle location.

A common buckling pattern, when subject to high impact velocities, is wrinkling at the proximal end due to large initial plastic strains, followed by wrinkling at the distal end due the reflection of the fast plastic stress wave. The magnitude of the shear stress wave slowed the slow plastic wave speed and resulted in strain localization which, under sustained plastic flow, deformed and buckled. An increase in lateral inertia resulted in small strains propagating at high speeds. Once a square tube region buckled, plastic reverse loading occurred, therefore stabilizing the section. The only way dynamic buckling could occur in each test was if plastic flow was sustained in the entire shell wall. It has been found that elastic unloading would occur during buckling deformation and interrupt plastic wave propagation. Regardless of the strain hardening characteristics, the shear stresses could significantly affect the plastic wave speeds. The study has also shown that a shell can absorb a larger kinetic energy if the mass is applied with a higher velocity. This is due to the proportion of kinetic energy that is absorbed during the compression and bending/folding phases. Smaller impact mass results in a larger portion of energy absorbed during the compression phase and small wrinkles are observed under large impact masses with the same initial velocity. The force displacement graph illustrates the initial compression phase as the flat initial part of the curve. If the force displacement graph shows an initial peak and an immediate decrease, it suggests the tube is under a force beyond the elastic limit with wrinkles forming under sustained plastic flow. A similar set of impact analyses was conducted using equivalent cylindrical shells and it was found that the length reduction was independent of impact velocity. The square and cylindrical shells may be buckling differently since the slow and fast plastic

stress waves travel at different speeds. Wave speeds in cylindrical shells are slower than those in square tubes due to the small radial inertia of the equivalent cylindrical section. Buckling characteristics of slow plastic waves are large folds developing from strain localisation and faster plastic waves develop quickly over a large portion of the shell.

The observations from the numerical and experimental tests of axially impacted cylindrical shells are reported in part one of Karagiozova and Alves publication [38]. The purpose of the study is to investigate the effective length and material properties that govern the transition from a progressive collapse to global buckling. Progressive collapse is considered local wrinkling or folding, contrary to global buckling, which is characterized by local denting and global bending. The experimental tests included quasi-static and dynamic axial loads on aluminum cylindrical shells with varying lengths. By varying the lengths, the critical length indicating a progressive or global buckling could be determined. From the quasi-static tests, the critical length to cause progressive or global collapse was found within 1 mm. Multiple cylinder lengths were also loaded dynamically using a drop hammer to determine the critical transition length from global to progressive buckling under dynamic loads. The test findings suggest that the critical transition length is sensitive to the impact velocity with the dynamic critical length more than doubling the static critical length. The increase in buckling transition length is due to inertial effects.

Numerically, the cylindrical shells were modelled using shell elements with a point mass on a rigid plane representing the impactor. To initiate asymmetric buckling, geometric imperfections in the shape of the first two buckling modes were included in the shell model. In order to achieve good agreement with experimental tests, an imperfection magnitude of 0.0005L was used. The numerical tests investigated the influence of yield and hardening modulus on buckling transition by analysing identical cylinders with various yield strength and hardness modulus. The kinetic energy of each test was kept constant by varying the impact velocity and mass. Resulting buckling behaviour for the three cylinder materials agreed with experimental findings suggesting that progressive collapse is sensitive to the impact velocity. The tests also found that the buckling

response was sensitive to the material properties as well. For materials with low hardening modulus, progressive collapse developed at lower velocities with more rapid local bending deformation growth. The reduced yield strength subsequently reduced the amount of energy absorbed during initial compression and thus reducing the critical buckling length. Generally, an increase in impact velocity was found to increase the critical buckling length. This, however, is not a rule since the numerical study found several increased velocities reduced stability when progressive buckling occurred at the distal end.

Numerical studies, including strain-rate effects, were also conducted and their results suggested an increase in impact velocity (compared to strain-rate insensitive cylinders) was required to cause progressive buckling of strain-rate sensitive cylinders. Karagiozova and Alves extended the dynamic buckling theory to include energy absorption phases. A large proportion of the kinetic energy is absorbed in the compression phase with the remainder of the energy absorbed through folding or bending. The development speed of local wrinkles has been shown to stabilize the cylinder response. Materials with similar strain hardening modulus were found to have similar available energy for global buckling after the initial compression phase. The lower strain hardening modulus was found to absorb more energy through folding due to quick wrinkle forming. Therefore, the proportion of the absorbed initial kinetic energy and the speed of local wrinkle deformation influence the critical buckling length. In conclusion, materials with high yield strengths and low hardening modulus are better energy absorbers than low yield strengths and high hardening modulus. This is due to the high energy absorbed during the initial compression phase, and increased speed of wrinkling due to low hardening modulus.

The second part of Karagiozova and Alves's [39] two part publication theoretically evaluated the critical buckling length, defining the transition from progressive buckling to global bending. The same bi-linear material characteristics in part one [38] were investigated in this paper as well, however, no attempt is made to associate modal interaction with the critical buckling length. During the low speed global bending and

high speed progressive buckling, a 1.0 ms compression phase was observed to exist. Following the compression phase, a maximum lateral displacement velocity was observed at the tip of a wrinkle (i.e., at the location of the buckling hinge). Lower bound estimation, Euler mode, of the critical transition length was analytically presented as:

$$L_{cr} = \frac{2R}{(1+\sqrt{\lambda})}\left(\frac{3E_h}{\sigma_0}\right)^{1/2} \quad \textbf{[40]}$$

where R is the cylinder radius, λ is the hardening to elastic modulus ratio, and σ_0 is the material yield strength. The Euler buckling is applicable to global bending about a single hinge; however, for a three rod two hinge mechanism, the critical transition lengths may be determined as follows:

$$L_{cr} = \frac{R}{(1+\sqrt{\lambda})}\left(\frac{18E_h}{\sigma_0}\right)^{1/2} \quad \textbf{[41]}$$

and,

$$L_{cr} = \frac{R}{(1+\sqrt{\lambda})}\left(\frac{30E_h}{\sigma_0}\right)^{1/2} \text{ (reproduced from [39])} \quad \textbf{[42]}$$

The total theoretical shortening of the model, at the end of the compression phase, is the area between the intersection of V_1 and V and below curve V, eq(25), shown in Figure 33 where:

$$V_1 = \frac{9\gamma w_0^2}{L}\sinh(2\gamma t)\,, \quad V = V_0 - \frac{A\sigma_0}{G}t \quad \text{(reproduced from [39])} \quad \textbf{[43]}$$

are a function of time, *t*, shell cross sectional area, *A*, material flow stress, σ_0, initial lateral displacement, w_0, initial impact velocity, V_0, impacting mass, *G*, and factor γ expressed as:

$$\boldsymbol{\gamma = \frac{3}{L}\sqrt{\frac{6\sigma_0}{\rho}}\sqrt{1 - \frac{30E_hR^2}{\sigma_0(1+\sqrt{\lambda})^2L^2}}} \quad \textbf{[44]}$$

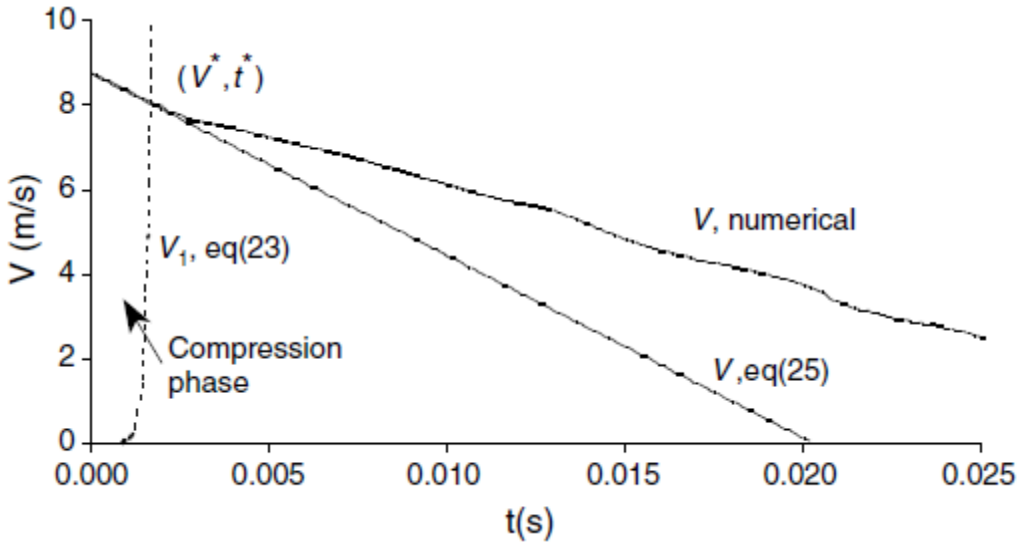

Figure 33 Striker velocity as a function of time used in the analytical and numerical solutions (reproduced from [39]).

Shells with low yield strength were found to remain in the compression phase longer than geometrically identical shell with a higher yield strength and equivalent hardening modulus. The impacted tube (with lower yield strength) requires increased impact velocity to stabilize the response and transition to progressive buckling. A two beam single hinge model was used to theoretically evaluate the impact problem for progressive buckling with material properties represented by spring stiffness attached to the rod ends and hinge. Using this theoretical representation, it was shown that the low strain hardening modulus contributes to high velocity buckling. The influence of axial inertia provided by the impacting mass was also evaluated and found that the increased impact mass increased the buckling velocity. For this set of analyses, the mass was increased with a corresponding decrease in velocity to keep a constant kinetic energy.

Empirical approximations of the critical transition buckling length from purely progressive buckling to purely global bending are developed in Karagiozova and Jones [40]. The approximations were derived from axial impact experimental tests followed by numerical analyses to verify the mechanics of each collapse. Numerically, the ratio of hardening modulus to the yield stress was evaluated for its influence on the critical length. The numerical studies also evaluated the influence of impact mass and velocity as

well as cylinder geometric characteristics such as length, diameter and wall thickness. Generally, the buckling patterns can be split into global bending (development of local plastic hinges), progressive buckling (local shell folding) and a combination of bending and buckling. The buckling behaviour is characterized by a compression and a bending phase which may be de-coupled. The compression phase is largely compression combined with small lateral displacement. The bending phase, however, has minimal compression combined with large lateral displacements and rotations. Semi-empirical approximations of the global hinge ($V_{1,glob}$), striker (V_{str}) and progressive buckling fold ($V_{1,\ progr}$) were developed using simplified representations of the bending and folding deformation behaviour. By correlating the time of buckling (t^*_{glob} or t^*_{progr}) from the finite element analysis, the earlier time to initiate buckling was found to dominate the deformation behaviour. This theory is shown graphically in Figure 34 with the corresponding deformed finite element mesh next to the graph. This is not the rule, however, since global buckling can develop after several folds have generated. As presented previously, low velocities lead to global buckling and higher velocities will develop progressive folding.

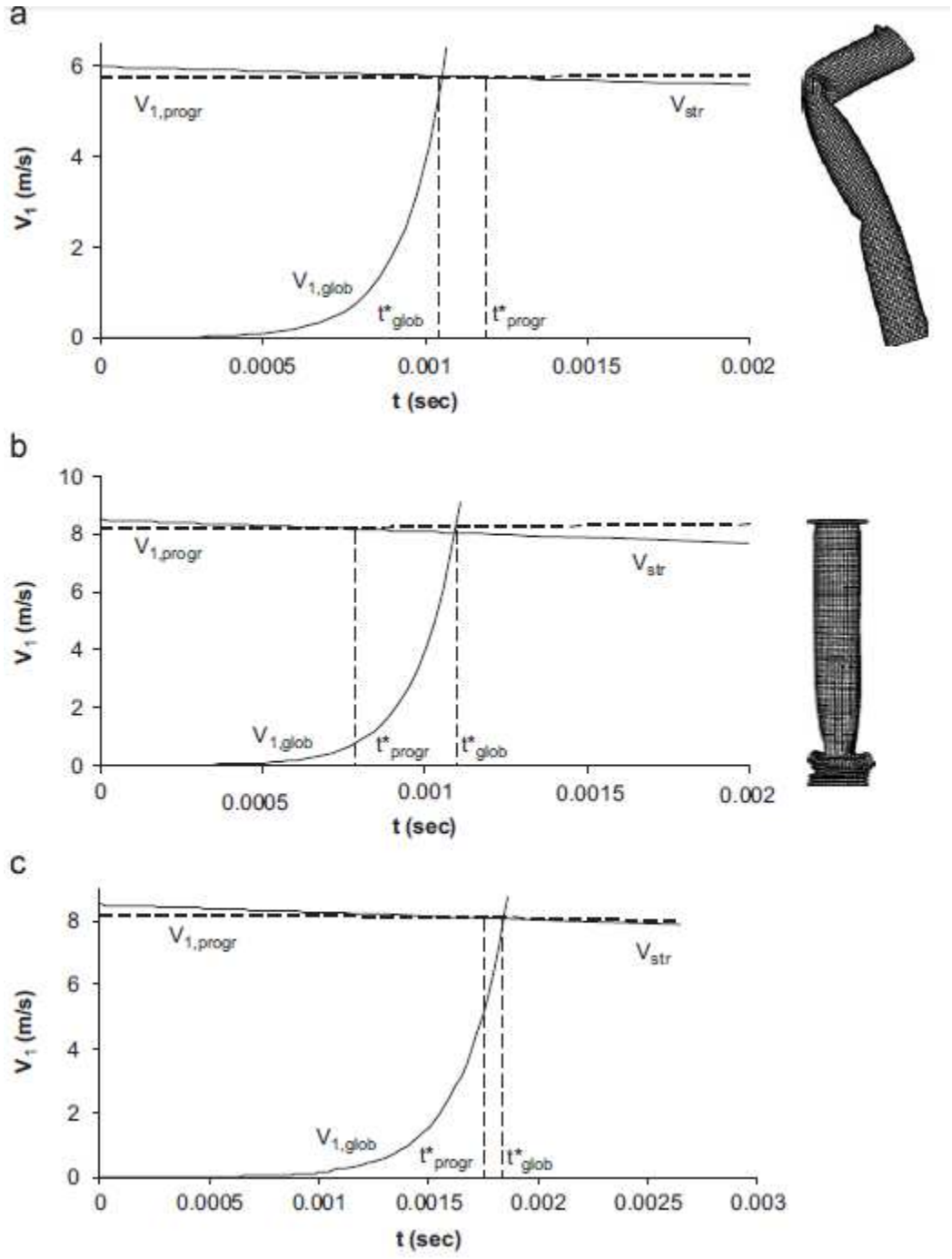

Figure 34 Transition from global to local collapse (reproduced from [40]).

In accordance with the graphs, it has been seen that an increase in local fold formation is the stabilisation mechanism when increasing the impact velocity. By varying the yield strength, it was found that global collapse develops quicker for low yield strength

materials due to the lower bending rigidity. The hardening modulus has been found to have a larger effect on progressive buckling which requires a larger hardening modulus to initiate buckling transition from global to progressive. An increase in the transition velocity does not relate to an increase in the compression phase duration. A higher yield stress has been shown to increase the global mode development speed during the compression phase causing a higher impact velocity requirement to achieve progressive buckling. A lower strain hardening modulus will result in a lower progressive buckling velocity than a cylinder with a higher strain hardening modulus. A material with a lower yield strength or cylinder with a thinner wall requires more folds to absorb the kinetic impactor energy.

3.6.2 Advanced Element Formulations

The local and global Euler buckling of stiffened plates and cylindrical shells was numerically investigated by Sridharan and Zeggane [75] using an element formulation embedded with the local buckling deformation. An amplitude modulation function was employed in the element formulation, which accounts for local modes and deformation with respect to the local element coordinates and neighbour elements using additional degrees of freedom. By using the novel element formulation one may account for the local and global buckling modes with a relatively coarse mesh. The study investigated the modal interaction of stiffened panels which have a reduced imperfection-sensitivity due to the resistance of the stiffeners to radial movement and the cancellation of plate buckling modes with stiffeners along nodal lines. To evaluate the element formulation, a 5-bay stiffened cylindrical shell modelled using eight second order elements. The buckling response using the novel element formulation (8 elements) was compared to the buckling response 16x24 8-noded element mesh in ABAQUS and found good agreement for global and local buckling modes. Sridharan and Zeggane [75] also investigated the global and local buckling modes of several beam section types with excellent agreement with the similar ABAQUS results.

3.7 SUMMARY

The collection of reviewed literature focused on the structural response of impacted bars, plates and cylindrical shells to provide examples of dynamic material characteristics and their influence on structural response. Several general concepts are emphasized including dynamic load factor (DLF), strain rate, elastic and plastic wave propagation as well as numerical analysis techniques to predict and characterize the dynamic pulse buckling.

The dynamic load factor has been utilized by many researchers to compare the dynamic response of the structure with the static Euler buckling load. The DLF varies as a function of load pulse shape and duration. It is generally at a minimum when considering the load duration is equal to the fundamental mode of vibration. Dynamic load factors which are less than unity suggest that the dynamic structural response may be less stable than the static response. The majority of the literature reviewed herein provides examples of DLF greater than unity suggesting the dynamic response of the impacted structure is improved over the static response. The same theory applied to naval platforms subject to short duration high pressure shock loads suggests the evaluation of the structure may be best evaluated as a function of the dynamic load duration, amplitude and modal response of the structure.

The effect of strain rate on the dynamic yield strength has generally been applied to cylindrical shell pulse buckling utilizing the Cowper-Symonds methodology. Several studies suggest strain-rate sensitivity will make a difference in the pulse buckling behavior and damaged state of the impacted object. Strain-rate effects are highly material and loading (compression, tension or triaxial) specific and may or may not govern the dynamic yield strength of the material of the loaded structure. The material and loading specific strain rate effects are observed in the variation in Cowper-Symonds coefficients used throughout the literature. In terms of applying strain rate effects to dynamically loaded structures, it is important to understand the material characteristics at the loading rates in question. Otherwise, an accurate approximation of the structural dynamic response may not be realized.

Elastic and plastic stress wave propagation has been used in many examples to describe and characterize the pulse buckling performance of structures subject to impact loads. The deformation of the impacted structures is a direct function of the material characteristics. Strain rate sensitivity and hardening modulus representation may alter the deformed state of the numerical prediction in terms of global response and local buckled regions. The sensitivity of the structural response to changes in hardening modulus or strain-rate sensitivity is a function of the impact momentum and energy as well as the structural configuration. Therefore, it is important to consider the dynamic problem (impacting and struck structures), material formulations and analysis requirements when predicting dynamic pulse buckling. The level of conservatism inherent in the analysis may be adjusted by the material constitutive model and modeling assumptions.

CHAPTER 4 NUMERICAL INVESTIGATION

Ship structures are required to remain operational following dynamic impact loads from wave slamming, ice crushing, or weapons effects, including underwater shock or air blast events. The structural response of the vessel subject to dynamic impact loads is legislated to remain elastic up to a prescribed design load limit. Under extreme dynamic loading conditions, the structural response may be well beyond the elastic yield limit for some sustained period of time. The duration of the load, loading rate and material properties of the loaded structure will determine the level of plasticity developed in the structure. Additional factors that may influence the level of plasticity in the structure include the global and local mass and stiffness of the loaded structure. The mass and stiffness at the global structure level will influence the modal response, thus increasing the amplitude of the structural response when the loading duration and natural frequency modes align. At a local structure level, the structural response may be influenced by local modes; however, stress wave propagation and reflection have been shown in the literature to govern the dynamic pulse buckling of impacted objects.

The following sections present numerical evaluations showing the response of structures that were considered in some published experimental studies, as well as a stress wave propagation investigation for a double bottom ship structure subject to a rectangular pressure pulse. Numerical simulations of experimental examples are used to present stress wave behaviour of elastic stress waves for stress wave loading and unloading problems. The simulations are validated using experimental data. Axial and shear stress wave propagation and interaction behaviour within a ship double bottom structure is presented. There are several different structural details within the double bottom structure and each has an effect on the stress wave behaviour. These include transverse floors with cut-outs and vertical stiffeners as well as transverse frames; which are discussed in detail in the following sections.

4.1 FE EXAMPLE OF ELASTIC UNLOADING

Consider two long slender bars struck by a hammer with the distal end of one bar free and the other bar fixed. The longitudinal stress wave propagates along the length of the bar and reflects at the end. In the fixed end condition, the reflected stress wave amplitude is the same as the incident wave amplitude. The reflected stress wave amplitude for the free end condition is opposite in sign. This theoretical stress wave behaviour will be evaluated numerically using published experimental test data. A common methodology to analyse the structural response of ships is through the use of finite element (FE) methods.

Starting with the initial works of Koning and Taub [43], dynamic pulse buckling of impacted structures was characterized using stress wave propagation. The experimental work of Abrahamson and Goodier [1] used high speed photography to observe the stress wave interaction in axially impacted bars. The tests impacted a long slender aluminum alloy bar into a steel plate with varying velocity, cross-section and length. Impacted ends of the bars sustained plastic flow until the elastic unloading wave arrives at the proximal end. The deformed shape of the impacted bar is generally characterized by a shortening and thickened impacted end however, at higher impacted velocities, a buckled region of the bar develops. The experimental results for a 457 mm long, 11.5 mm diameter rod of aluminum 6061-T6 are shown in Figure 35.

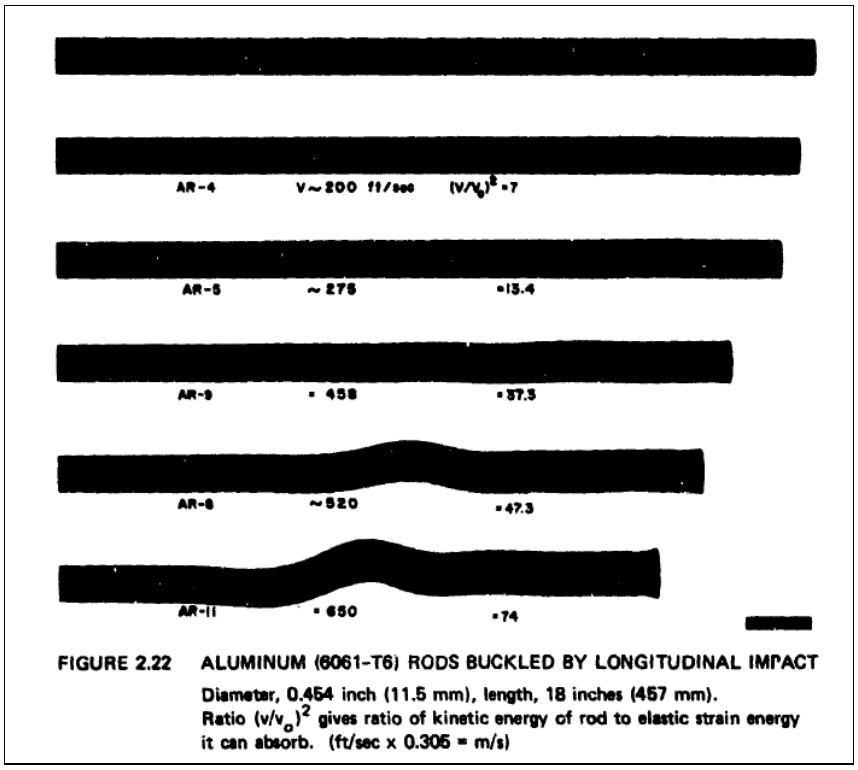

FIGURE 2.22 ALUMINUM (6061-T6) RODS BUCKLED BY LONGITUDINAL IMPACT
Diameter, 0.454 inch (11.5 mm), length, 18 inches (457 mm).
Ratio $(v/v_o)^2$ gives ratio of kinetic energy of rod to elastic strain energy it can absorb. (ft/sec x 0.305 = m/s)

Figure 35 Impacted thick aluminum bars with varying impact velocity (reproduced from [49]).

The experimental test in Figure 35 is a relatively simple problem that can be replicated numerically. By doing so, one may evaluate how well numerical methods idealize stress wave propagation and predict the rod shortening amplitude. Impacted slender rods were analysed using LS Dyna's [52] explicit finite element solver. The rods were modeled without imperfections using 1.5 mm hex8 solid elements. This refinement level was sufficiently refined to capture the elastic and plastic stress front as it propagated along the bar. The rod material was represented using an isotropic and kinematic hardening constitutive material model with hardening modulus and yield strength of 1,240 MPa and 310 MPa, respectively. Strain rate effects were ignored in the analysis since the bars are made up of low strain rate sensitive aluminum. The rod is considered unrestrained, loaded using an initial velocity and impacts a fixed steel plate; contact algorithms have been defined to replicate the impacting action.

The axial stress contours are plotted in Figure 36 at six different time instances showing the early impact time on the left and progressively later times on the right. The impacted

end is the bottom of the plot with the free end at the top of the rod where time is labelled. Initial impact is shown at time instance 1 with axial stress propagating from the bottom to the top of the figure. The elastic unloading wave reflects off the free distal end of the rod between time instances 3 and 4. Time instances 5 and 6 show the unloading wave propagation from the free distal end to the impacted proximal end of the rod. The experimental tests published in [49] used high speed photography to capture the stress wave propagation and elastic unloading. Figure 36 presents similar stress wave propagation characteristics with an elastic unloading wave reflecting from the free distal end of the impacted rod.

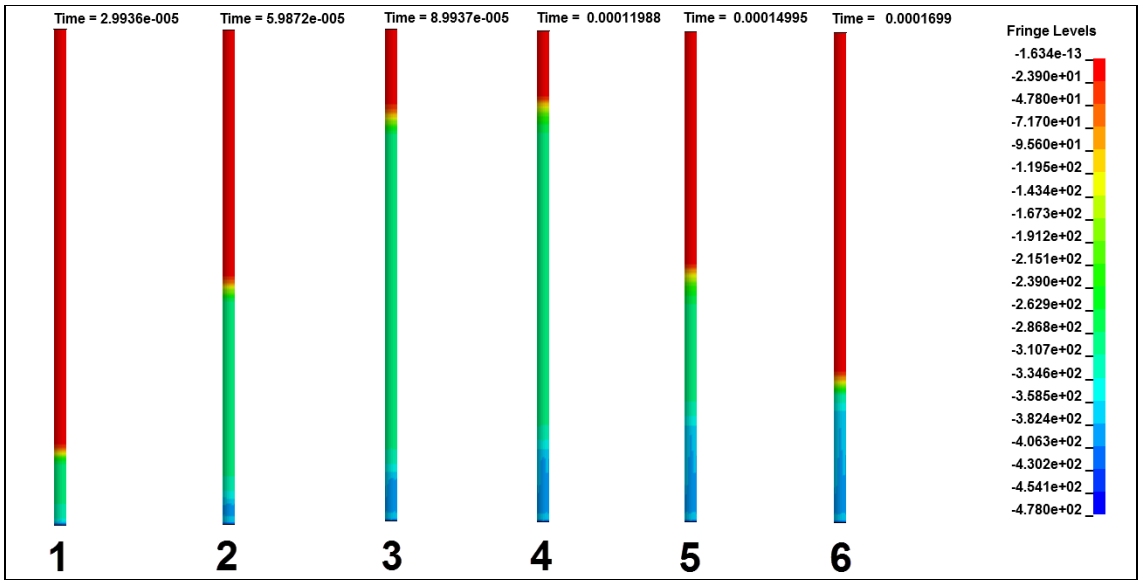

Figure 36 Axial stress contours along AR-4 from initial impact (left) through elastic unloading (right) (MPa).

The longitudinal/axial stress wave propagation is properly simulated using finite element analysis; however, it is also important to replicate the deformed shape of the impacted rod. Table 1 presents the test specimen, impact velocity and rod compression magnitude. The numerical and experimental compression magnitudes compare well for specimens AR-4, AR-5 and AR-9. The variation in the numerical and experimental compression amplitude may be a result of small strain-rate sensitivities in the material as well as the nonlinear characteristic of the material stress-strain curve at stress amplitudes above dynamic yield. At impact velocity of 158.6 m/s, the numerical and experimental compression magnitudes begin to diverge. The deformed shape of the experimental

impacted rod AR-8 includes a half sinusoid buckle at approximately the mid-length of the rod. The numerical analysis, however, does not compute a similar deformed shape. A thick impacted end of the impacted rod is developed in the numerical analysis and is the extent of the plastic deformation. In order to predict the buckled condition in Figure 35, an initial imperfection in the numerical model is required.

Table 1 Numerical (LS-Dyna) and experimental compression amplitude.

Specimen	Impact Velocity		Compression (mm)	
	ft/s	m/s	Numerical	Experimental
AR-4	200	61.00	5.86	5.588
AR-5	275	83.88	11.30	11.684
AR-9	458	139.69	28.15	28.448
AR-8	520	158.60	34.80	38.608

4.2 FE Example of Stress Wave Reflection

The deformed slender bars in Figure 35 have a free distal end opposite the impacted proximal end. The stress wave propagation characteristics of an impacted bar with a fixed distal end are different than a bar with a free distal end. The capability of the FE methods to predict the stress wave propagation characteristics has been shown throughout the literature. Parameters of the numerical analysis published in the literature may not be applicable to all dynamic problems. To study the dynamic stress wave propagation in a fixed ended impact problem, the works by Hayashi [29] are replicated using LS-Dyna [52]. Hayashi [29] experimentally and numerically analysed a curved slender bar of rectangular cross section subject to low [29] and high [30] speed impact loads with a fixed distal end. The Hayashi [29] low speed experimental setup is shown in Figure 37 with mass M impacting the slender bar along a motion guide G. The motion guide ensures the motion of the impacting mass is purely axial. The distal end of the slender bar resists translational motion as well as rotation about the axial and out of plain (y) axis. The bar is considered free to rotate in the y-x plane about the z axis.

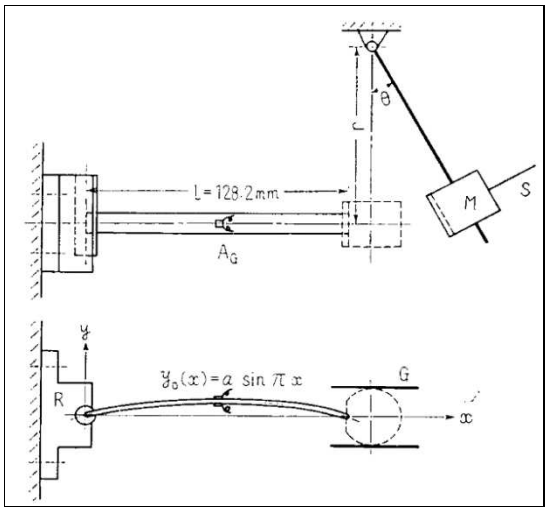

Figure 37 Experimental test setup for low impact dynamic buckling showing plan view (top) and elevation view (bottom) (reproduced from [29]).

The numerical analysis in [29] solved a series of partial differential equations to approximate the lateral deflection and central axial force of the impacted bar. Validation of the numerical analysis is presented by Hayashi [29] as a comparison between the numerical and experimental force time history. The mid-column normalized numerical displacement (blue dashed), and experimental force (green dashed) are plotted in Figure 38 as a function of normalized time. Five impacts between the impacting mass and beam are indicated by the five positive pressure peaks. The Normalized experimental and numerical force amplitudes are similar for the first impact between $\bar{t} = 0$ and $\bar{t} = 20$. The numerical force amplitudes of Hayashi [29] deviate from the measured experimental forces for the following four impacts.

The experimental setup in Figure 37 was numerically analysed using LS-Dyna [52] explicit solver without additional imperfections included in the numerical model. The sinusoidal out-of-plane imperfection was the only form of imperfection included in the numerical model. To replicate the physical response of the experimental test, the impacted end of the slender beam was restrained to out-of-plane translation such that it is free to translate axially. The opposite end is restrained in five degrees of freedom with the beam free to rotate about the z-axis, in the y-x plane. The impacting mass was represented by an unrestrained thick plate with an initial velocity and contact defined between the mass and beam end using a LS-Dyna [52] contact algorithm.

The numerical work of Hayashi [29] is verified by comparing the numerical and experimental force-time relationship; as shown in Figure 38. An approximation of the experimental and numerical force-time relationship is plotted in Figure 38 with the analysis herein labelled “Pearson – LS Dyna”. Some differences between the Hayashi [29] experimental and Pearson numerical force-time relationship are apparent in the force amplitude and phase during the third, fourth and fifth mass impacts. The difference between the “Experimental” and LS-Dyna force amplitude and phase is, however, marginal and the numerical model has accurately captured the physics of the problem for low impact loads.

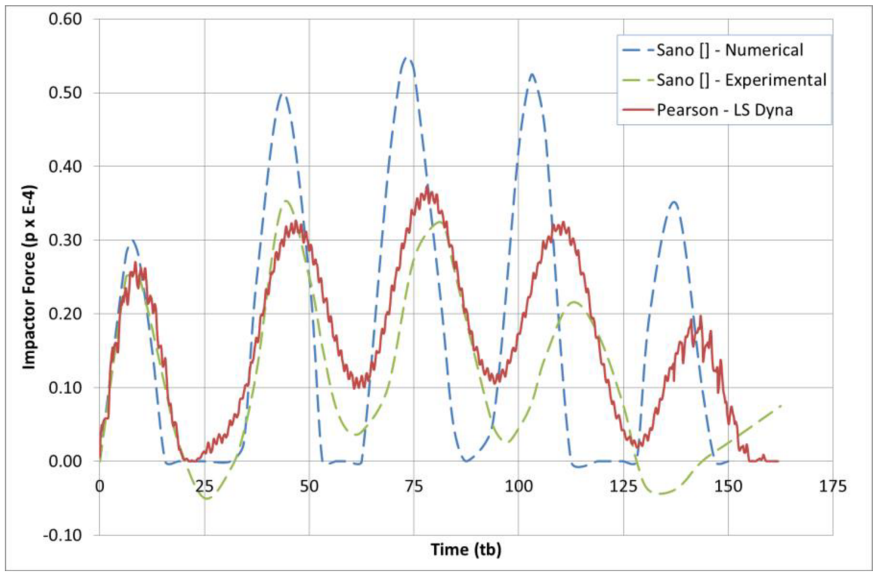

Figure 38 Normalized numerical (Pearson) and simplified Hayashi [29] numerical and experimental impactor force.

The axial stress wave propagation of the slender beam problem in Figure 37 is shown in Figure 39. Axial stress shortly after impact is plotted at the bottom of the figure and the stress state after reflection shown at the top. The axial stress wave is initially propagating from right to left since the impacting scenario is such that the fixed end of the beam is on left, and the impacted end is on the right. Stress reflection characteristics are well presented in the top three beams of Figure 39. When the axial stress wave reaches the end of the beam, prior to reflecting, the stress amplitude is approximately 1.0 MPa. After

reflection, the stress amplitude increases to approximately 2.0 MPa. A doubling of the stress wave amplitude is observed in the stress contours at the fixed end.

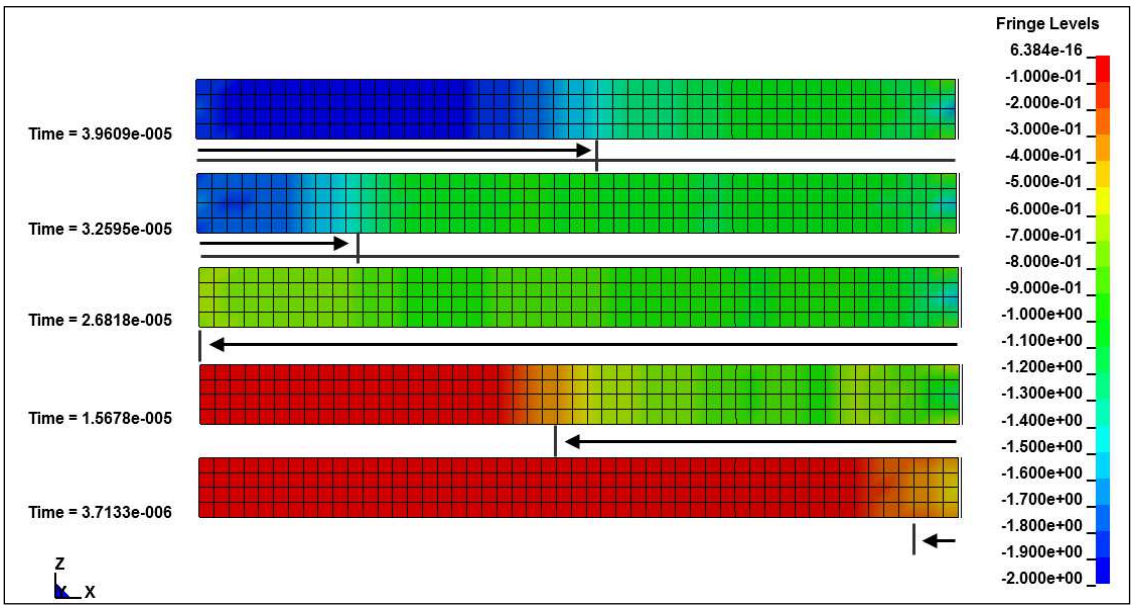

Figure 39 Axial stress wave propagation of from early impact (bottom) to post reflection (top) (s) (MPa).

A detailed observation of the stress wave propagation can be determined by plotting the mid-surface axial membrane stress as a function of time. Figure 40 and Figure 41 present the axial normal XX stress for the full analysis and early stress-time history, respectively. The full stress-time history in Figure 40 describes how the stress develops in the beam during the impact event with a relatively consistent mid-surface elemental axial stress throughout the impact event.

A detailed inspection of the axial normal stress amplitudes along the bar early in the beam response time is plotted in Figure 41. The theoretical initial and reflected stress wave arrival times are plotted as vertical dashed lines. The location of the elements along the length of the beam are also plotted in Figure 41 with increasing element number corresponding to further position from the impacted end of the bar. In Figure 41, the arrival of the stress wave is observed at each element along the length and indicated by a rise in membrane stress to roughly -1 MPa over 0.044ms. Each element experiences a rise in membrane stress to roughly -1 MPa followed by a period of sustained stress amplitude

until the arrival of the reflected wave. The sustained stress amplitude exists during a period of constant loading. Once the reflected wave arrives, the elemental stress amplitude rises to roughly -2.0 MPa over a similar period as the initial stress rise to -1.0 MPa. The reflected stress wave increases the amplitude in each element until it reaches the element closest to the impactor; where the stress originated. At this instance in time, the stress behaviour and interaction is complex and may not be simply described by axial membrane stress wave characteristics. Impactor mass and velocity as well as beam stiffness and modal response to the impact load begin to influence the stress amplitude.

Theoretical arrival times for the initial and reflected stress waves agree well with the measured values from the impact analysis. This is observed by comparing the vertical dashed lines in Figure 41 with the corresponding changes in stress amplitude in the solid line with the same colour. Using element number 146 (orange) as an example, the initial stress wave arrival in the analysis (solid) and theoretical (dashed) suggests an arrival time of 0.018ms. The reflected stress wave theoretical arrival time has a similar level of agreement with the initial stress wave comparison with the analysis at 0.032ms. An interesting effect of the stress wave interaction is the stress wave influence on loading behaviour. The loading rate, in this instance, decreases steadily and plateaus until the arrival of the reflected stress wave.

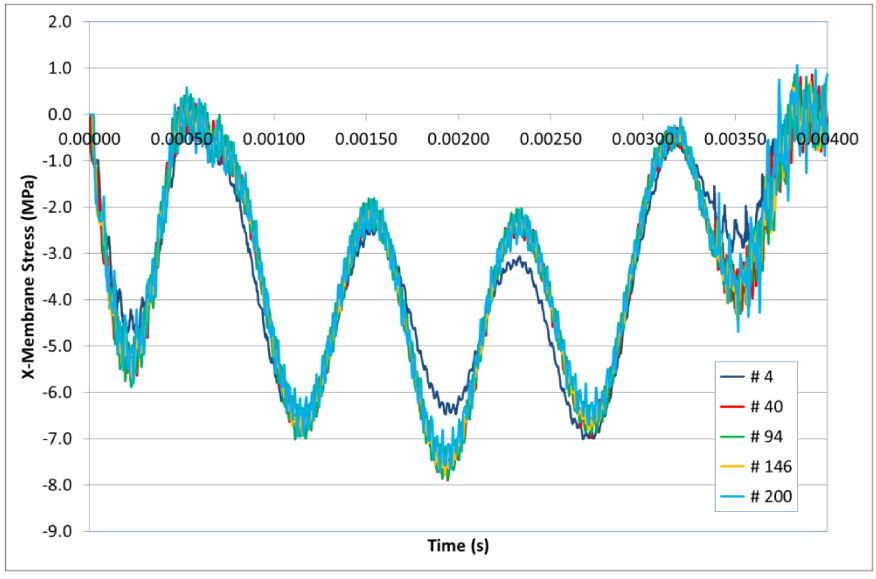

Figure 40 Mid-surface X-membrane stress along the length of the impacted beam full time history.

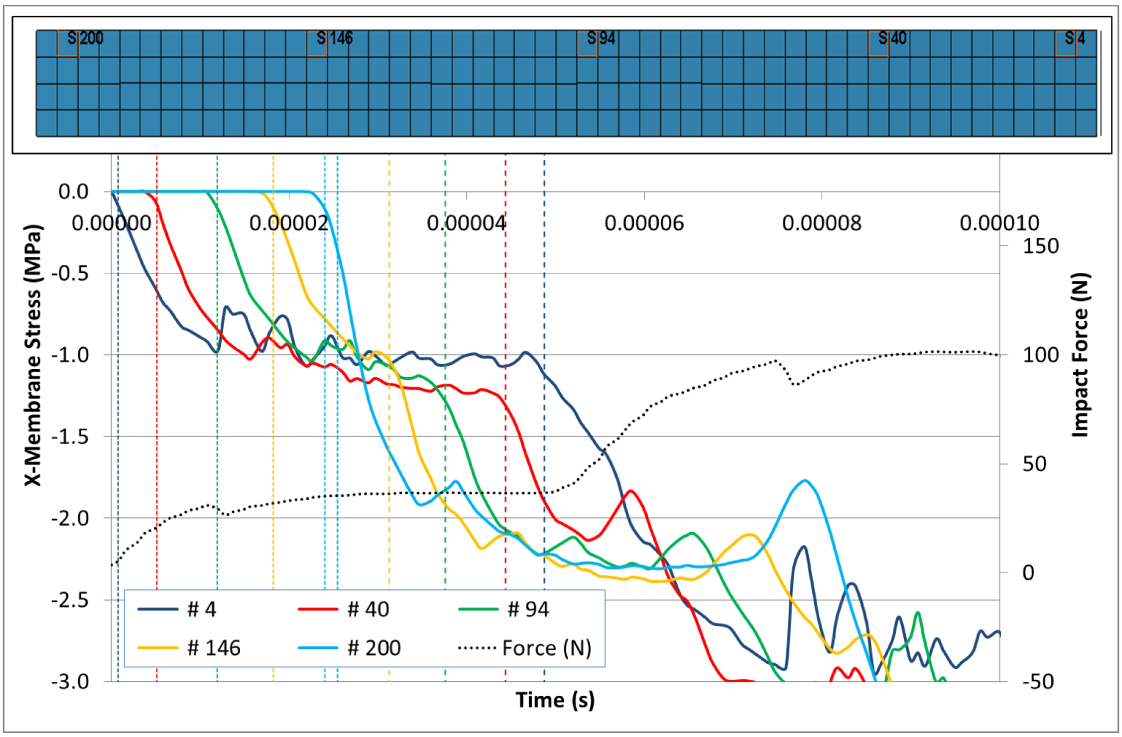

Figure 41 X-membrane stress along the length of the beam from impact to t=0.1 ms and location of elemental stress (impact on right) with impact force.

4.3 FE Example of Dynamic Pulse Buckling

There are several examples of dynamic pulse buckling that utilize numerical methods to predict the buckling behaviour of impacted cylinders. Many publications include structural imperfections to induce pulse buckling with minimal reference to experimental testing for verification of the numerical model. An example of a cylinder impact study which includes experimental verification and does not use imperfections in the numerical model, is the dynamic pulse buckling problem of Lu *et al.* [53]. Lu *et al.* verified their numerical representation using the experimental set up in Figure 42. The dynamic buckling of the fluid-filled cylindrical shell, labelled 'specimen' in Figure 42, is induced by the drop hammer tup impacting the gasket, '2', and the loading cell, '3'. The impacting force is measured in the loading cell while the fluid pressure is measured by the pressure transducer, '1', at the bottom of the test specimen.

The study by Lu *et al.* investigated the buckling behaviour of the cylinder subject to different impact velocities and impacting masses for variations in cylinder length, material type and wall thickness. The experimental test and numerical analyses are presented in [53] with excellent agreement in displaced shape, pressure time history and force time history for several examples of specimen configurations and impact scenarios. The numerically replicated the fluid-structure interaction of the dynamic buckling problem using the arbitrary Eulerian-Lagrangian (ALE) method employed by LS-Dyna. The Lu *et al.* analysis [53] used ALE elements to represent the fluid and the study herein simplifies the problem by using Lagrangian elements to represent the fluid. The analysis included contact definition between the hammer tup and cylinder top as well as cylinder wall self-contact. The cylinder is considered fixed at the base with no representation of the gasket or loading cell.

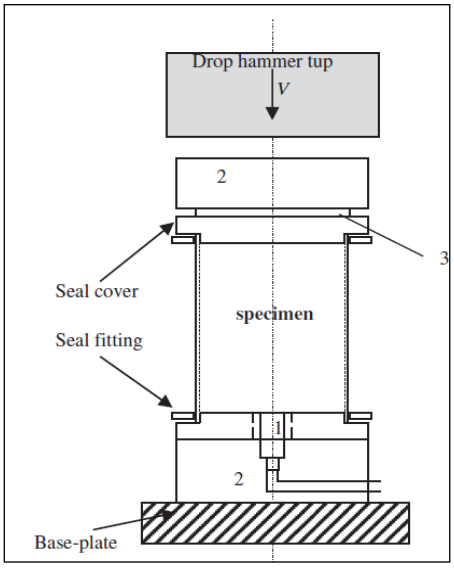

Figure 42 Experimental dynamic impact test setup (replicated from [53]).

The test case analysed was a 244mm long aluminum cylindrical shell with radius of 75.5mm, 1mm wall thickness and impacted by a 56kg mass at 6.26m/s impact velocity. The model consists of 2976 shell elements representing the cylinder wall with 7 through thickness integration points and 14,400 hexahedral solid elements representing the fluid. The cylinder wall material model is represented using an isotropic hardening constitutive model with hardening modulus of 1% of the elastic modulus. The fluid material model utilized MAT_ELASTIC_FLUID with a bulk modulus of 1.93 GPa.

The displaced shape from the experimental tests of Lu *et al.* [53] and the current study are shown in Figure 43 with generally good agreement. The flattened region near the top of the cylinder and buckling modes along the length of the cylinder match the experimental test well. The amplitude of the buckled modes are slightly greater in the experimental analysis. This may be due to the limitations in assuming a single hardening modulus for the cylinder wall material, application of Lagrangian fluid elements and an imperfection-free model. In addition to the displaced shape of the impacted cylinder, the impulse measured at the bottom of the cylinder was also compared and shown in Figure 44. Excellent agreement is observed in the impulse time history throughout the analysis. Based on the agreement between displaced shape and impulse time history, it can be concluded that using the simplified Lagrangian fluid model can adequately represent the physical effects of the internal fluid.

Figure 43 Lu *et al.* experimental displaced shape (left), Lagrangian fluid model displaced shape (right).

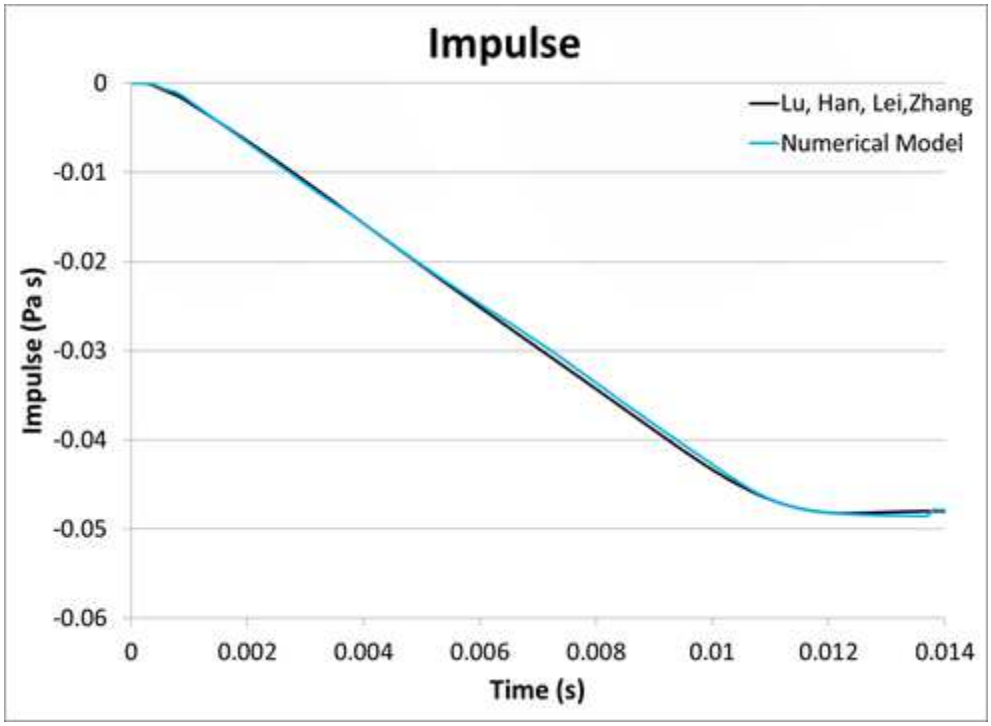

Figure 44 Impulse time history comparison between Lu *et al.* [53] and Lagrangian fluid model.

Several elements along the length of the cylinder wall (plotted in Figure 45 at deformed and undeformed states) were chosen to display the stress wave behaviour. Elements near the impacted and fixed ends of the cylinder (5046, 5574 and 7110, respectively) are in the pulse buckling region with significant plastic deformation while elements in the mid-region of the cylinder (6054 and 6678) are outside buckled zones and deform under radial expansion. By plotting the initial and reflected stress wave arrival times, one may observe the change in stress amplitude with respect to elastic and plastic stress wave characteristics. The initial and reflected stress wave arrival times are plotted in Figure 46 as vertical solid and dashed lines, respectively. Each line colour is associated with each element along the length of the cylinder wall. By plotting the von Mises stress amplitude as a function of time along with the stress arrival times, conclusions about the stress wave behaviour may be drawn.

The initial and reflected stress wave arrival time plotted in Figure 46 is computed using the von Mises stress wave velocity in the numerical analysis (approximately 4,250 m/s).

Analytical approximations of the axial stress wave (equation [8]) in the aluminum cylinder shell overestimate the stress wave velocity (5,200 m/s). The over-prediction in stress wave velocity may be due to the Lagrangian approximation of the fluid. Consider a single element on the cylinder wall, each node of that element is connected to the neighbouring aluminum cylinder shell elements and solid fluid elements. By simplifying the cylinder wall and water interaction as fully connected systems, this may have resulted in the slowed stress wave propagation. However, the deformation of the cylinder and impulse matches well with the experimental measurements, therefore, the reduced stress wave velocity is representative of the structural system and adequate for this evaluation.

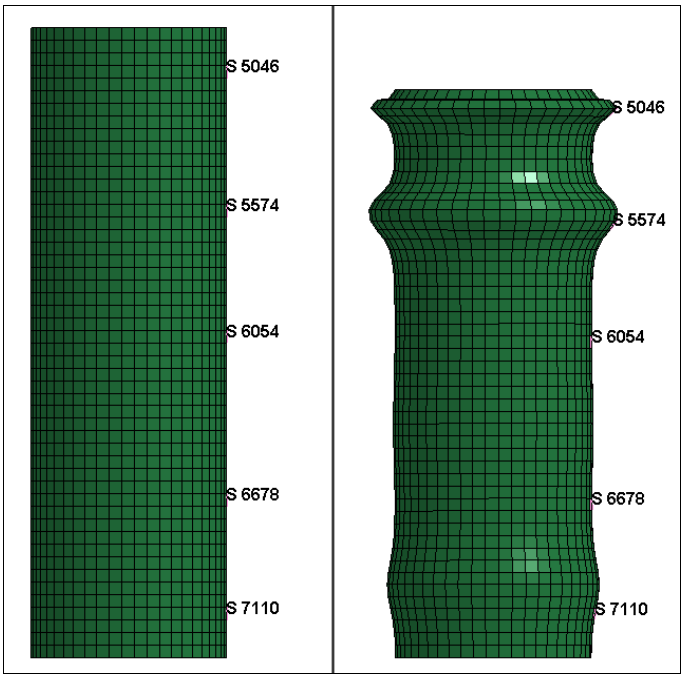

Figure 45 Cylinder shell elements used for stress wave analysis of undeformed (left) and deformed (right) cylinder.

The initial and reflected longitudinal elastic stress arrival times in Figure 46 align well with several of the positions along the length. However, there are some anomalies in the stress behaviour that may not be solved purely by the elastic stress wave. The von Mises stress amplitudes of elements 7110, 6678 and 6054 are characterised well by the longitudinal stress wave response. A doubling of the von Mises stress amplitude is initiated by the arrival of the reflected longitudinal stress wave. The von Mises stress

behaviour cannot be purely characterized by the longitudinal stress wave in elements 5046 and 5574. The von Mises stress in element 5574 does increase at the arrival of the reflected longitudinal stress wave, however, the stress amplitude marginally increases prior to the stress wave arrival. By plotting the arrival time of the longitudinal plastic stress with the von Mises stress amplitude in Figure 47, one may observe the stress wave characteristics of element 5046 near the impacted end of the cylinder. The von Mises stress amplitude of element 5046 increases initially through the elastic wave (approximately 95 MPa), and then continues to increase as the plastic wave arrives soon after the elastic wave amplitude is reached. Element 5574, however, is not directly influenced by the plastic stress wave, since the elastic wave has enough time to reflect at the end of the cylinder and double the initial stress amplitude in the element.

The elastic and plastic stress wave characteristics are shown in the element von Mises stress amplitudes in Figure 46 and Figure 47. This indicates the elastic and plastic stress wave propagation characteristics discussed in Chapter 2 and 3 are applicable to this problem. It also indicates that the deformed shape of the cylinder in Figure 45 can be correlated with the plastic and elastic wave propagation characteristics. The plastic folding zone occurs in the region governed by the plastic wave. Similarly, buckled regions along the cylinder length developed at regions which are governed by reflected elastic stress wave.

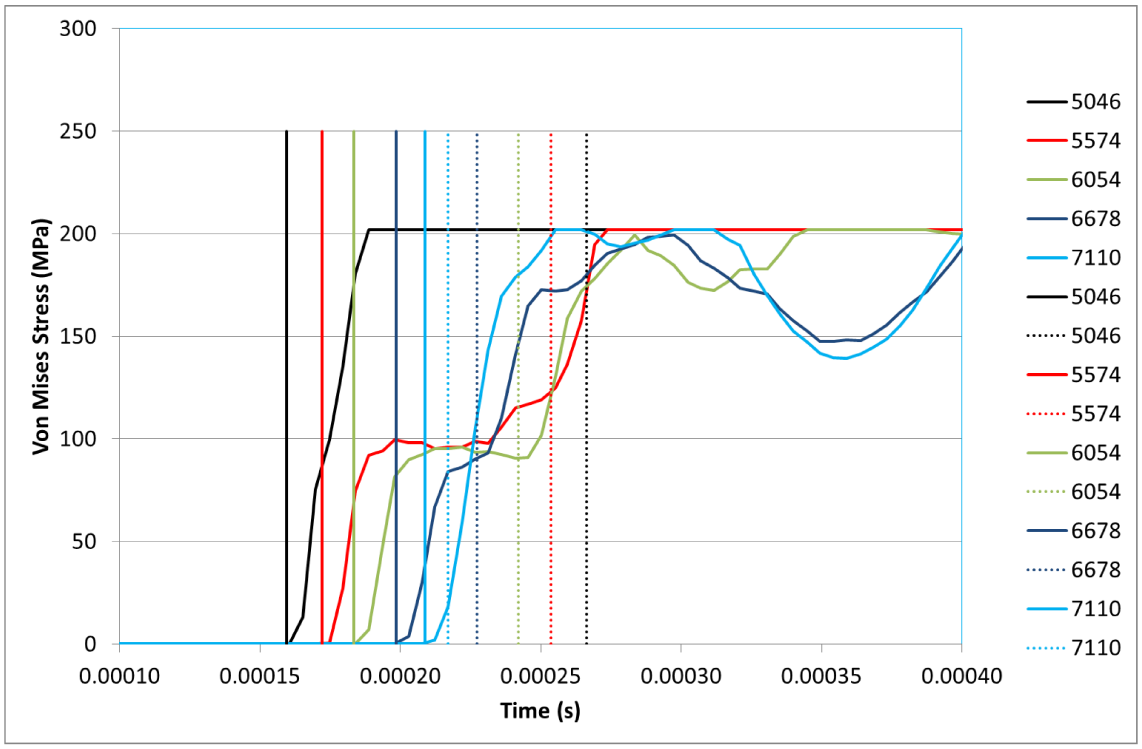

Figure 46 Mid-surface von Mises stress with initial and reflected longitudinal elastic stress wave arrival.

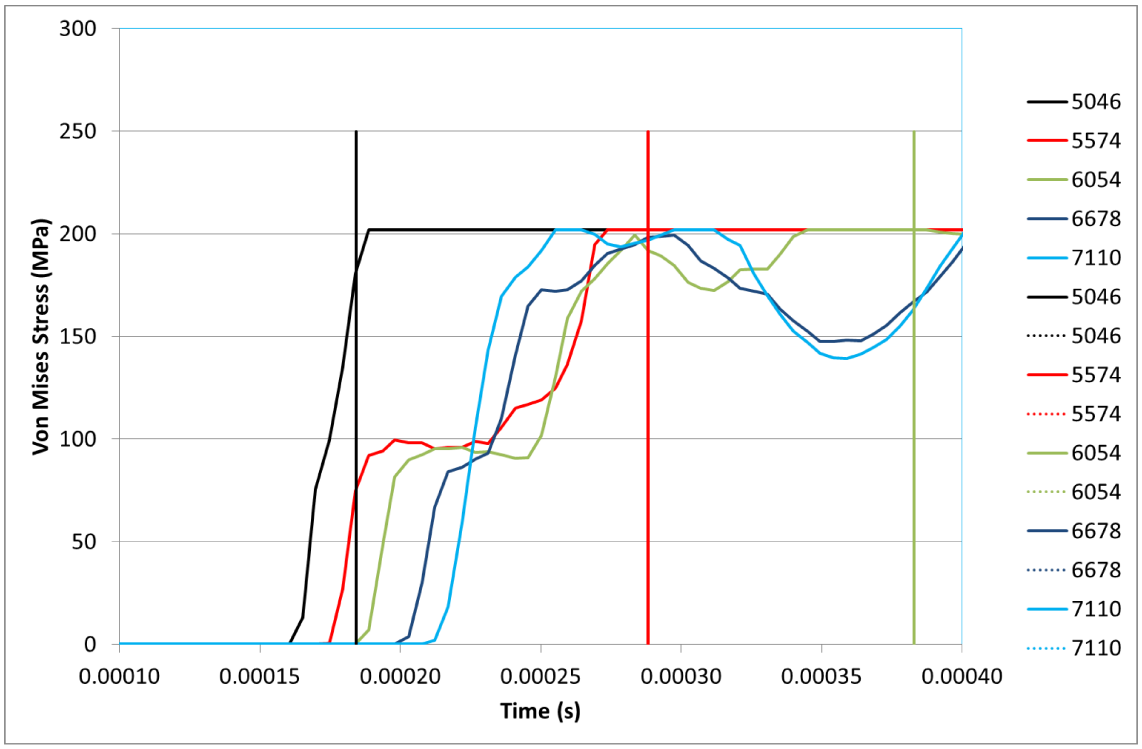

Figure 47 Mid-surface von Mises stress with the initial longitudinal plastic stress wave arrival.

4.4 Stress Wave Interaction in Ship Double Bottom Structure

The previous examples verified the theoretical stress wave propagation behaviour in axially impacted bars. A significant influence on the stress wave behaviour is observed as the fixity/stiffness of the impacted bar increases positively. The literature and theory considers simple examples when describing stress wave propagation behaviour. Ship structures, however, are complex systems with varying stiffness positioned longitudinally, vertically and transversely. As the complexity of the structural stiffness increases, a more detailed description of stress wave propagation behaviour may be required when considering pulse buckling response of such systems.

An example of a complex ship structure arrangement is the double bottom section of an icebreaking vessel. Figure 49 shows the port side numerical model of the symmetrical icebreaker double bottom structure. Several different regions of stiffness are found in this section, including: transverse deck and hull stiffeners, cut-outs and stiffeners in the transverse floors, flanged and free-edged brackets, as well as unstiffened longitudinal plating between transverse frames. The modelled structure in the double bottom section is fully welded together with sniped bracket flanges and web stiffeners to accurately represent the stress propagation in a similar structure. The double bottom depth at the centreline is 1830 mm, with 406 mm transverse stiffener spacing. The section is loaded by a step-wise rectangular pressure pulse shown in Figure **48** with 1.0 ms duration and constant amplitude applied to the hull plating. The boundary conditions applied to the numerical model include; symmetrical conditions along the centreline as well as the forward and aft longitudinal plating nodes. The boundary conditions idealize a symmetrical, continuous/infinitely long section subject to the same pressure loading representation. Further verification of the symmetrical boundary condition accuracy to represent an infinitely long system is required. The symmetrical boundary conditions are sufficient for this study of stress wave propagation. The furthest port edge of the model (at the end of deck and bracket) was pinned. This was done to simplify the model and remaining structure outboard and above the double bottom structure.

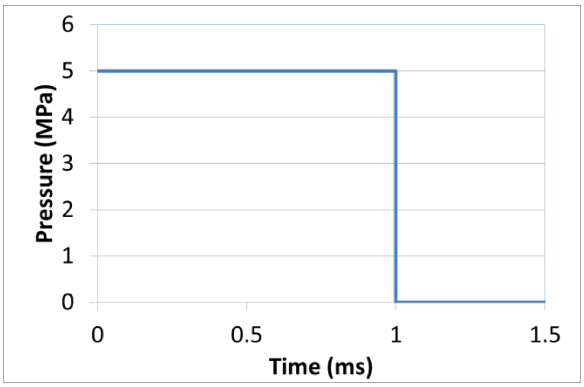

Figure 48 Pressure pulse applied the hull plating.

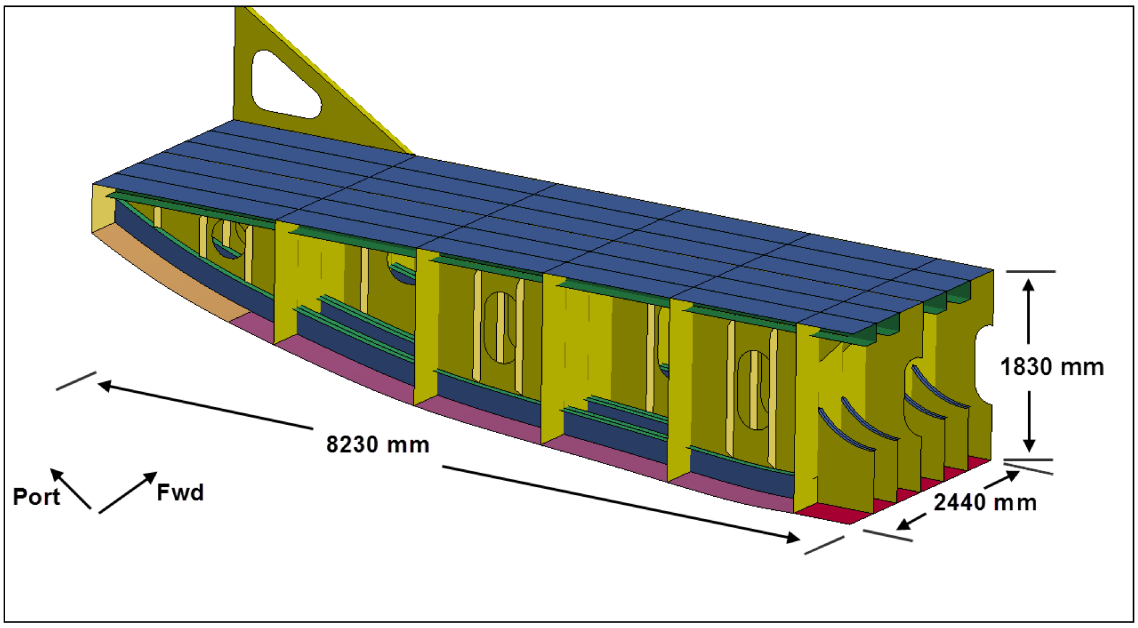

Figure 49 Icebreaking double bottom section.

The double bottom is meshed with a relatively coarse 50 mm element size to capture the specific details of the stress wave propagation behaviour. When considering the element size for a specific problem, the analyst must ensure the element size is sufficient to capture the expected progressive collapse and local folding that may develop. The stress contours in Figure 50 depict the mid-surface global ZZ (vertical) stress at six different instances in time (from t=0.017 ms to t=0.43 ms). Red stress contours represent tensile stresses, and blue/yellow/green stress contours represent compressive stresses. The transverse floor in Figure 50 is initially at a stress state of 0 MPa. Once the pressure load is applied to the hull plating, the stress wave begins to propagate through the vertical

structure unobstructed until it approaches the cut-outs. A similar observation can be made as the stress wave propagates past the cut-outs with stress concentrations developed on the sides of the cut-outs and stress reductions at the top and bottom. The stress reductions above and below the cut-outs are a result of the cut-out shape. Similar stress behaviour around cut-outs is also developed when the geometry is subjected to quasi-static loads. The Lloyd's Register Naval Ship Rules [51] require the ship designer to account for cut-outs when computing the hull girder strength. To determine the effective strength of the section, each cut-out must account for longitudinal extension or shadow zone of the cut-out. Figure 51 shows the maximum longitudinal extension of deck openings as per Lloyd's Register Naval Ship Rules [51]. The stress contours in Figure 50 show the relatively low stress amplitudes above and below the cut-outs similar to the maximum cut-out extension in Figure 51. The length corresponding to the low stress contours, however, does not match the length of the cut-out extensions. This may be due to the structural configuration of the double bottom transverse floor, and suggests the maximum extension may be considered as a conservative estimate of the cut-out effective length.

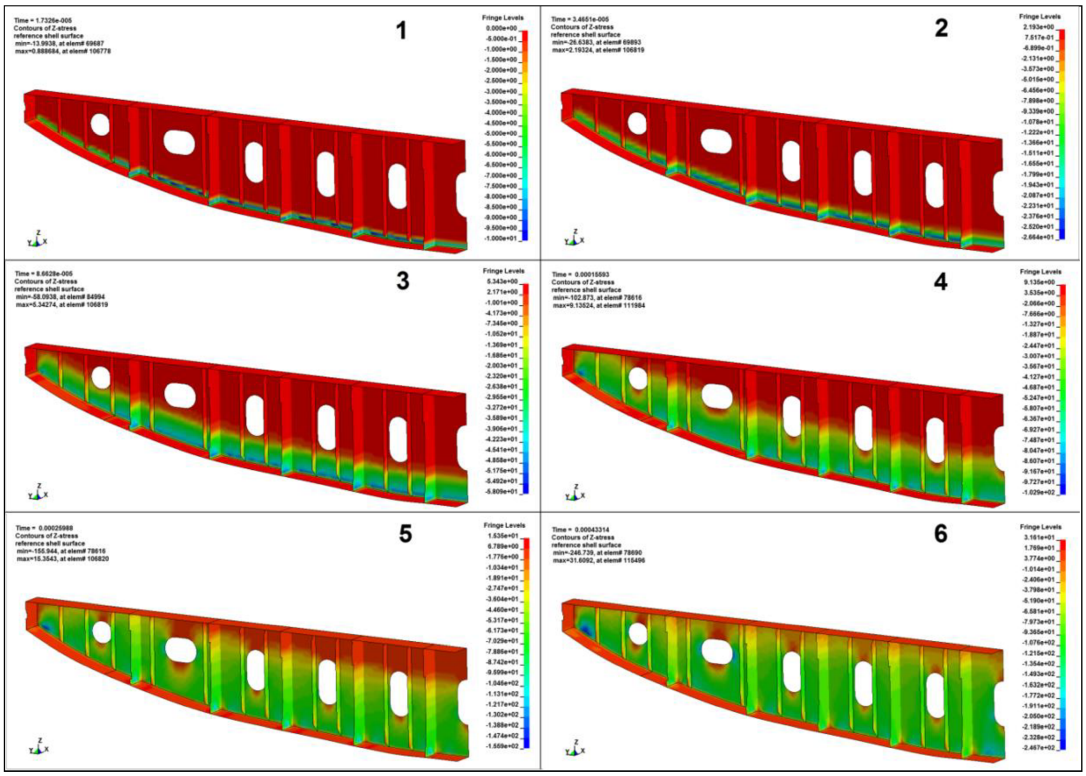

Figure 50 Contours of directional Z (global) stress in the double bottom transverse floor.

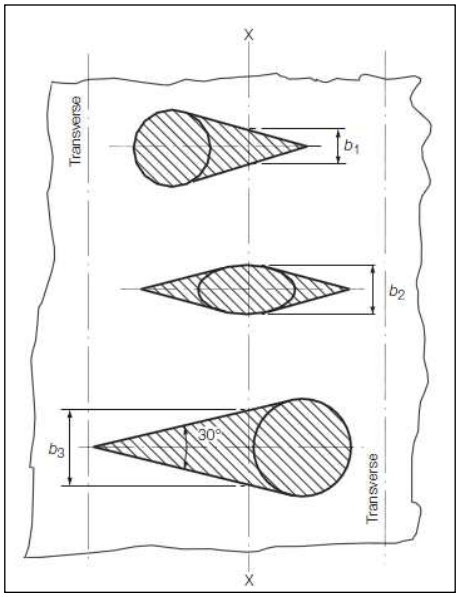

Figure 51 Longitudinal extensions of hole openings or shadow regions (reproduced from [51]).

Similar to the global ZZ stress plots in Figure 50, global YZ (transverse-vertical shear) directional stress contours are plotted in Figure 52 at 5 instances in time (for t=0.069 ms to t=0.398 ms). The stress contours in time instances 1, 2, 3 and 4 are fixed (-5 MPa to 5 MPa) in an effort to display the stress wave propagation behaviour. Shear YZ stress in time instance 4 and 5 are the same, however, the stress contour range in 5 is adjusted to (-50 MPa to 50 MPa) to display the stress amplitude at this instance in time. The shear stress contours in item 6 of Figure 52 are the same as item 5 to show how the stress propagates at this amplitude.

The shear stress wave propagation in the transverse floor is influenced by the shape of the hull and web stiffeners resisting the transverse (-Y) component of the pressure load. One may observe this by comparing the stress developed in the longitudinal girder nearest the centreline and the web stiffeners port of the centreline. The plating near the centreline is loaded with a small transverse component, and as a result, has low shear stress wave amplitude. Several YZ shear stress characteristics are observed in Figure 52 including stress concentrations developed at cut-out corners upon stress wave arrival and web stiffener influence on the floor web shear stress at early phases of stress wave

propagation and interaction. The figure at time instance 6 shows the stress arresting function of the shear stress in transverse floor webs. As the stress begins to propagate away from the cut-out radius towards the longitudinal double bottom girder connection, the web stiffener redirects the shear stress downward along the stiffener edge.

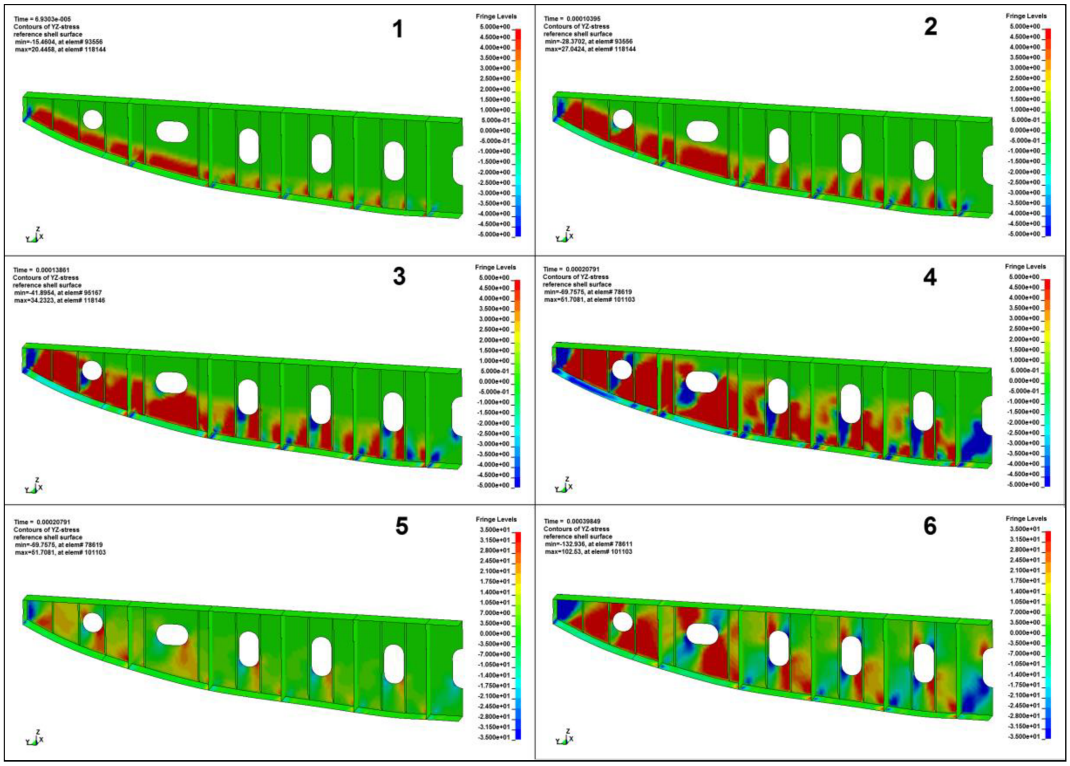

Figure 52 Global YZ stress contours in the double bottom transverse floor.

Icebreaker transverse floor structure shown in Figure 49 has two common sections; the transverse floor web frame shown in Figure 50 and Figure 52, spaced every 3 frames, and the stiffened frame sections spaced 406 mm. Some commonalities are shared between the transverse floor types, including web plating cut-outs and web stiffeners. The variations between the two structures include the deck and hull transverse stiffeners, alternating web floor plating and bracketing near the centreline. Changes in structural details also resulted in changes in the stress wave propagation characteristics.

The mid-surface global Z (vertical) stress contours are shown in Figure 53 at different instances in time. Similar stress wave propagation characteristics are displayed in the stress amplitude around the cut-outs and web plating in instances 3 to 6. Some changes in

the ZZ stress states are shown most clearly in the hull stiffener web at time instance 2. The stress amplitude varies as a result of the stiffness above the flange of the transverse hull stiffener. Higher stress amplitude is measured in the web plate stiffened sections than the unstiffened open sections. The stress variation suggests there may be a change in stress wave behaviour in the stiffener web of the open section and stiffened web section. To investigate the stiffener web stress wave interaction behaviour, the stiffened web and open sections near the centreline were refined to 10mm. The global ZZ (vertical) directional stress is plotted in Figure 55 for several elements through the depth of the hull stiffener web shown in Figure 54**Error! Reference source not found.**. Directional stresses in the stiffener web of the open section and stiffened plate section as well as initial stress wave arrival and reflected wave arrival times are paired by colour. Element 177,660 (solid line) and 181,067 (dashed line) are near the flange of the hull stiffener and plotted in black. The black solid and dotted vertical lines represent the initial and reflected stress wave arrival times of element 177,660, respectively. Similar stress amplitude and stress wave arrival pairs are also plotted in Figure 55 for other element pairs through the depth of the hull stiffener.

Although the element pairs are not precisely positioned at the same elevation above the hull plating, a general pattern is observed between the reflected stress wave arrival and stress amplitude. The stress rate remains constant until the reflected stress wave arrives. At the arrival of the reflected stress wave, the stress rate begins to deviate, reduce and become non-linear. The stress rate deviation is a function of the stiffness of the structure above the stiffener flange. A decrease in stress rate is observed in the open section upon arrival of the reflected wave, and a constant stress state remains in the stiffened web plate above the stiffener.

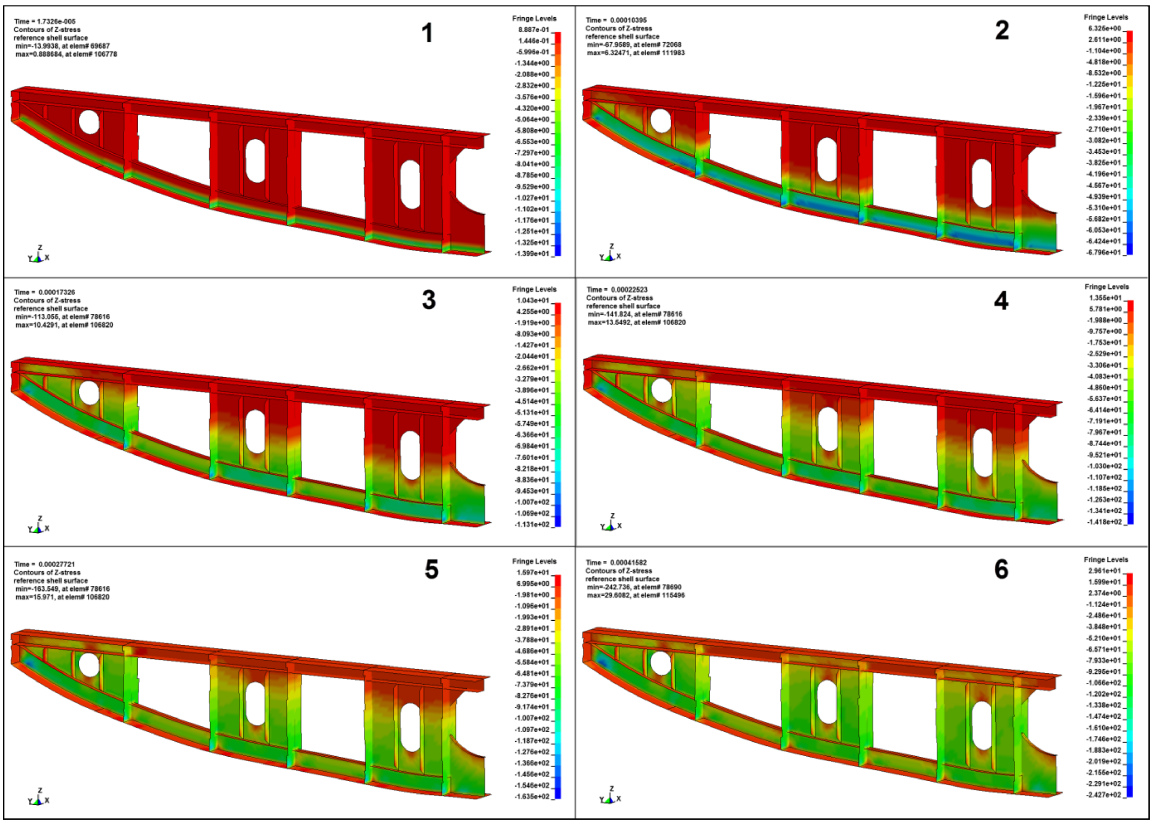

Figure 53 Variations in the ZZ component of global stress contours in the transverse stiffened floor.

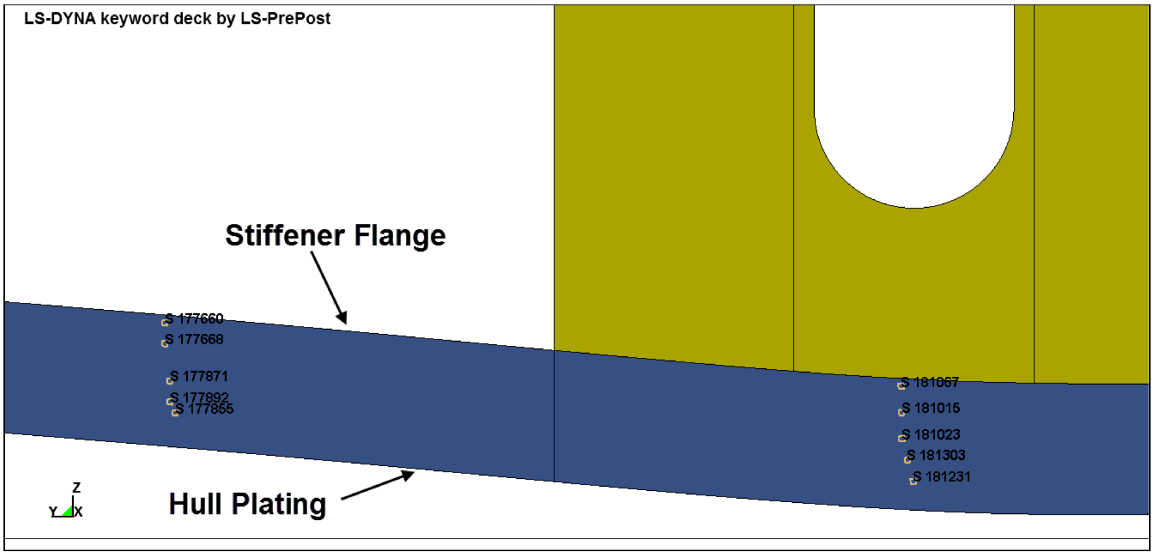

Figure 54 Element positions for stress time history reported in Figure 55.

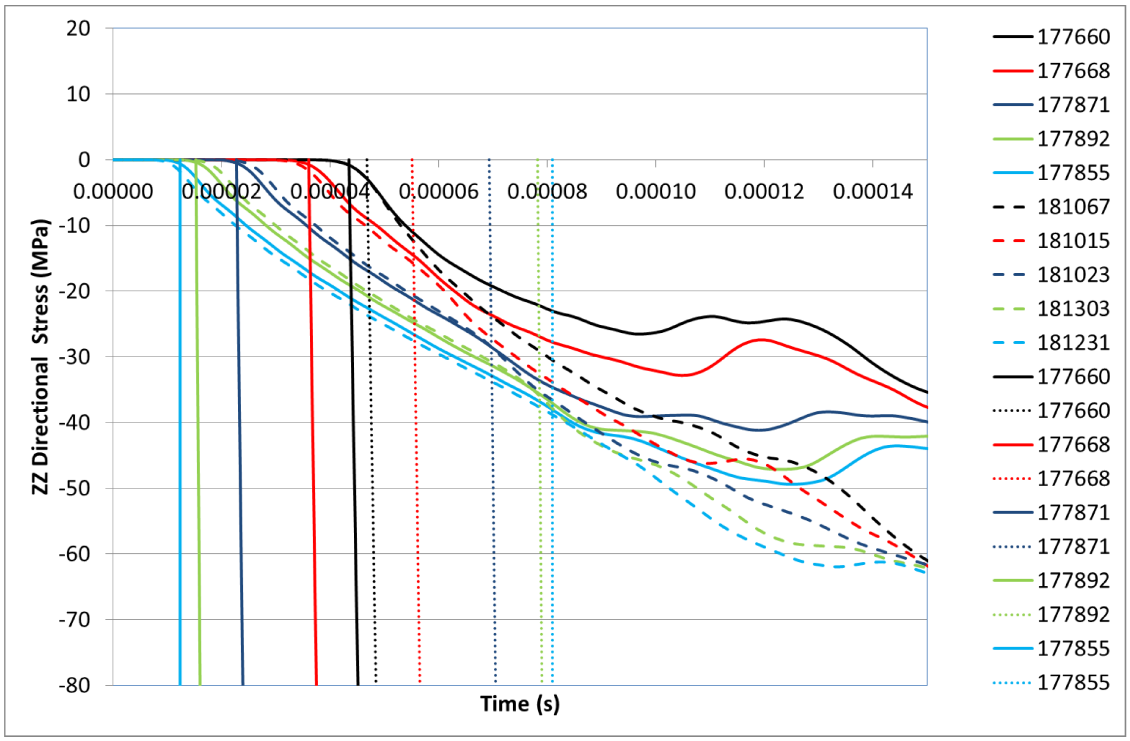

Figure 55 Variation of the global ZZ (vertical) directional stress as a function of time, including stress wave arrival time.

The global YZ (shear) directional stress of the stiffened transverse floor, in Figure 56, shows more variation than the Z directional stress in Figure 53 when compared to the transverse web frame in Figure 52. The YZ directional stress in the transverse floor initiates at the connection between the web frame web stiffener and the hull, where a discontinuity in stiffness exists. The stiffened transverse floor does not have web stiffeners below the stiffener flange and the shear stress wave initiates at the longitudinal girder/hull connection. Once the stress propagates through the depth of the stiffener web, the shear stress amplitude increases at the web stiffener toe. The stress contours of time instances 1 through 5 are plotted in Figure 56 from -5 MPa to 5 MPa to more clearly display the stress wave propagation characteristics. Web stiffener stress arresting and redirecting behaviour is also observed in the stiffened transverse floor. Instead of the shear stress developing across the web plating, it is redirected toward the hull stiffener flange. Stress states 5 and 6 in Figure 56 are the same instance with the stress contours adjusted in instance 6 (-50 MPa to 50 MPa). In instance 6, the stress amplitude is less than instance 6 seen in Figure 52, which represents the same time. The reduction in stress

amplitude is due to the reduction in web stiffener effective span provided by the flange of the transverse hull stiffener.

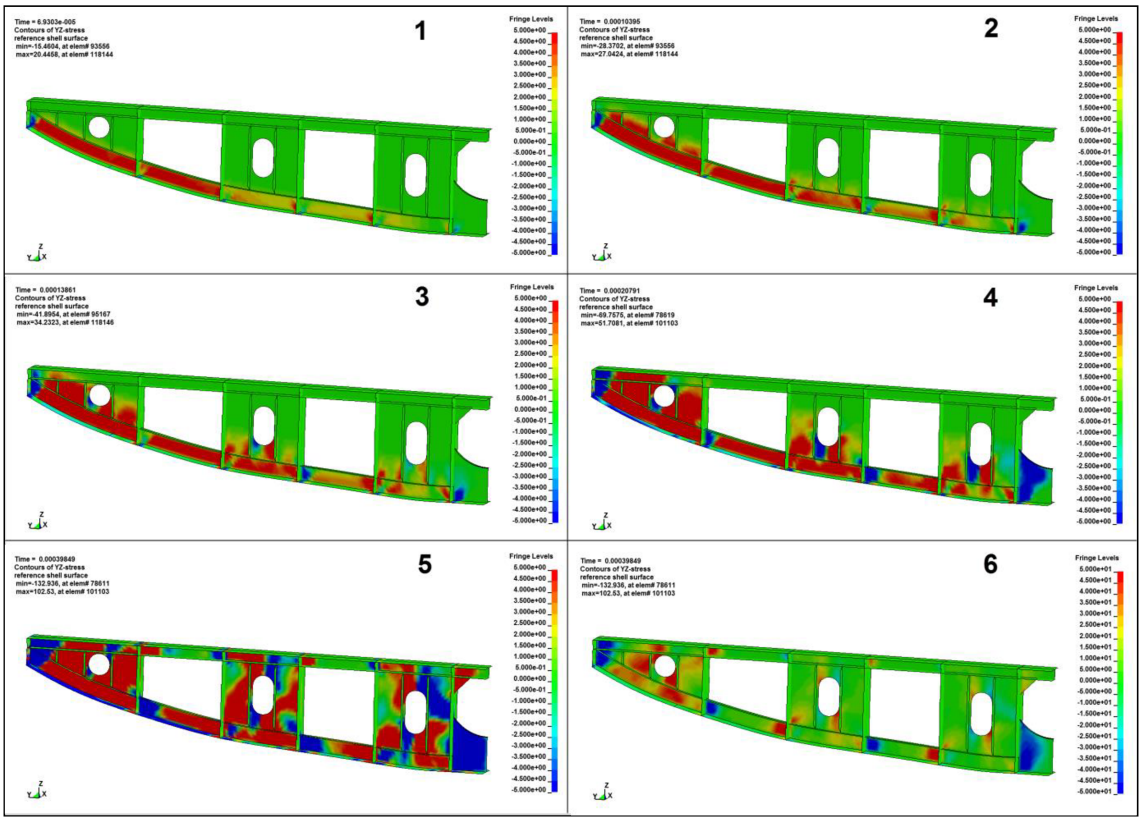

Figure 56 Variation in the global YZ stress contours in transverse stiffened floor.

The stress wave propagation behaviour was investigated within the double bottom structure of an icebreaking ship. Shear and normal stress contours within the stiffened plate transverse floor structure indicated that the stress wave interaction is governed by the local structural details. The normal stress propagation past the cutout is governed by the shape of the cutout. Normal stress concentrations are observed at the corners of the cutout with shadow zones developed above and below the cutouts. The shear stress was largely influenced by the plate web stiffeners within the floor. This was indicated by the redirection of the shear stress along the edge of the web stiffener near the cutout. Within the transverse framing section, the normal stress wave propagation was influenced by the continuation of plating above the frame flange. When plating exists above the stiffener flange, the stress within the frame web continues to increase. In the web section that does

not have plating above the flange, the stress amplitude is reduced by the elastic stress wave reflection off of the flange surface. Based upon the stress wave interaction within the double bottom transverse floor and frames, the early stress wave interaction may not be used to characterize the structural response. The local structural details within the double bottom structure provide the structural stability required to prevent dynamic pulse buckling.

CHAPTER 5 SUMMARY AND CONCLUSION

5.1 DYNAMIC MATERIAL CHARACTERISTICS

Elastic and plastic stress wave propagation characteristics and theory are utilized in the context of this study to provide a general background of the stress state developed in structures subject to dynamic loading events. The amplitude and duration of the elastic and plastic stress wave is a function of the loading environment and shall interact or propagate as a function of the structural configuration. In order to determine the presence of plasticity during a dynamic event, one may be required to understand the strain rate characteristics of the material at the strain rate levels of interest. There are several physical testing methodologies required to characterize the strain rate sensitivity, each facilitating a range of strain rates. Strain rate sensitivity is typically measured to assess the effect of strain rate on the yield strength of a particular material. The adjustment in yield strength as a function of strain-rate can be included in numerical strength predictions by using constitutive material formulations. Application of constitutive material models to a particular dynamic event may require specific knowledge of the expected material effects, including sensitivities of the material to temperature.

Most of the commonly used pulse buckling prediction methodologies are highly sensitive to the material and structural representation of the dynamic event. In terms of the material representation, the analyst must ensure that an appropriate hardening modulus is defined, and strain rate sensitivities are properly accounted for. The hardening modulus directly influences the plastic wave propagation speed and therefore, changes the extent of the plastic zone. Predicting the dynamic yield strength and presence of plasticity during the loading event may be directly related to the strain rate sensitivity included in the material constitutive model. An oversensitivity to strain rate may result in an overly stiff material representation at strain rates of interest and an under sensitivity to strain rate may result in premature buckling. Proper material constitutive models and representation of the impacting event are required to accurately predict the deformation behavior of the loaded structure.

5.2 Dynamic Stress Wave Propagation

The influence of stress wave propagation on structural response may vary between structures and dynamic loading events. A specific structural response that may be directly influenced by stress wave propagation is dynamic pulse bulking. The historical and present dynamic pulse buckling characteristics and prediction methodologies have been reviewed. Many studies simplified the dynamic pulse buckling experimental test by considering a rod or cylindrical shell subject to impact loading. The effect of stress wave propagation in the reviewed examples was most greatly influenced by the structural arrangement and stiffness of the boundary conditions. Upon impact, an axial elastic stress wave propagates until it reflects as an unloading or loading stress wave, depending on the impedance of the boundary condition at the distal end of the impacted structure. Unloading stress waves are a result of free end or low impedance boundary conditions and may reduce the extent of the plastic zone. Fixed end or high impedance boundary conditions result in a doubling of the stress wave and may result in dynamic pulse buckling of the distal end of the impacted structure.

5.3 Geometric Imperfections

The presence of geometric imperfections within the numerical model may be required to accurately predict the dynamic response of the loaded structure. The shape and amplitude of the imperfection varies with the structural configuration and loading scenario. Rod and fluid-filled cylindrical shell impact examples reviewed in Chapter 3 were modeled without inclusion of imperfections. A comparison with the experimental tests showed that imperfections were required to predict the deformation of the rod at high impact velocities; however, an accurate representation of the fluid-filled cylinder did not require geometric imperfections. This suggests that the amplitude and shape of geometric imperfections are specific to the structure and dynamic loading scenario of interest.

5.4 Stress Wave Interaction in Simple and Complex Structures

Stress wave propagation and interaction behavior for fixed and free impacted structures have been numerically evaluated in Chapter 3 along with a brief investigation into stress

wave behavior in ship double bottom structure. These examples have shown that the stress amplitude experienced early in a dynamic event can be attributed to directional stress wave interaction. In simple problems, the early stress wave interaction may be enough to characterize the global response of the structure. For complex structures such as the ship double bottom evaluated herein, the global response of the structure cannot be determined through directional stress wave propagation characteristics. Stress wave propagation may be well suited for characterizing the response of simple structural configurations such as a lattice mast. The plated structure of a ship double bottom is complex and structural stability is provided through local structural details.

5.5 Analyst Guidance for Dynamic Pulse Buckling Problems

There are multiple items to consider when evaluating a dynamic problem sensitive to stress wave propagation and dynamic material characteristics. A decision tree is provided in Figure **57** to summarize the considerations required when evaluating such a dynamic problem. The analyst must first consider the complexity of the loaded structure and the loading duration. If the structure is similar to the ship double bottom structure considered earlier, it may be sufficiently stiffened that stress wave propagation would not influence the structural stability. For simple structural systems, the FE numerical model would likely require inclusion of geometric imperfections. The types of imperfections include variations in thickness, extent and shape amplitude specific to the loaded structural system. Along with the geometric imperfections, the analyst must also accurately model the dynamic material behaviour using an appropriate constitutive model. Depending on the strain and loading rate, the constitutive model may need to include strain rate dependency or material's equation of state. For load pulse durations (T_s) longer than the buckling mode periods of interest (T_p), the elastic buckling or plastic progressive collapse may be considered adequate for the evaluation. For load pulse durations shorter than the buckling mode period (T_p), the mass and velocity should be properly represented such that the momentum and kinetic energy are accurately accounted for in the numerical simulation.

Once the structural configuration and loading are properly represented numerically, then the finite element model can be analyzed using a dynamic non-linear explicit FE solver. The analysis results can then be post processed using a similar methodology presented in Chapter 4 to track the stress wave propagation. During the post processing phase, determination of dynamic pulse buckling must be carefully considered using dynamic stability criteria specific to the needs of the structural problem.

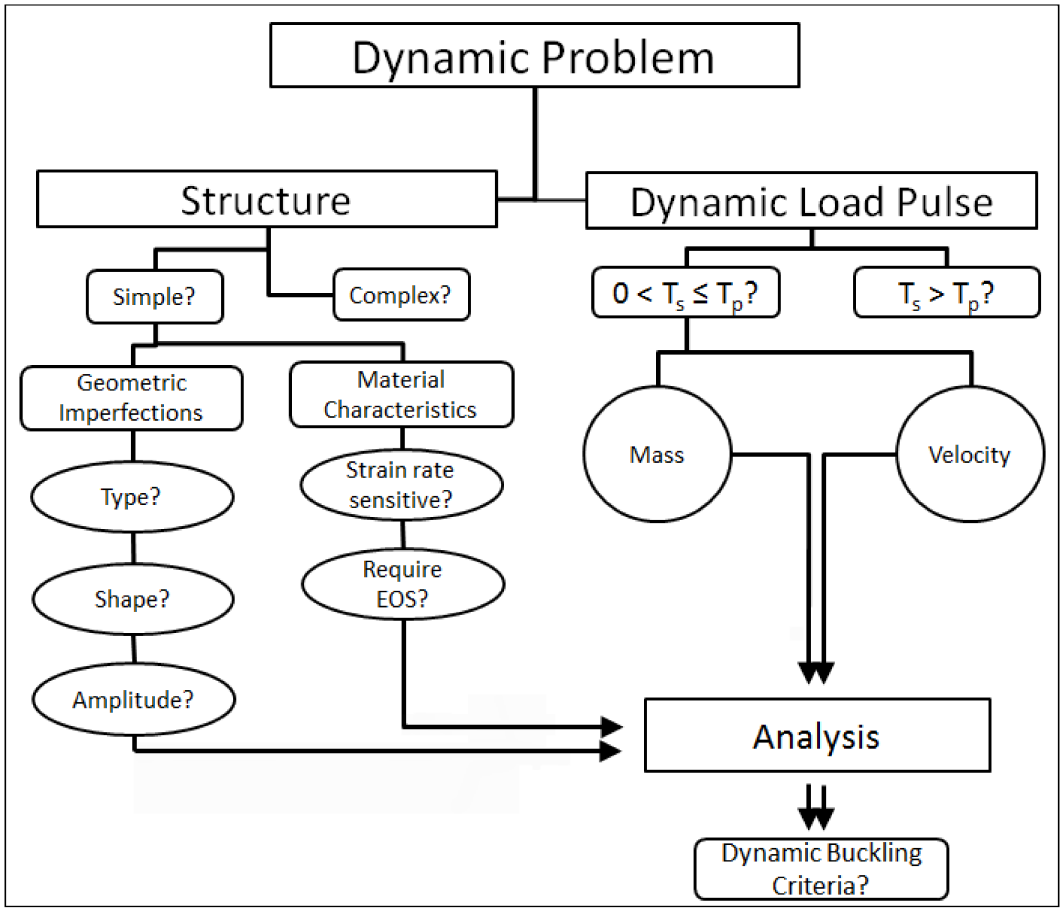

Figure 57 Decision flow chart for the analysis of dynamic stability problems sensitive to stress wave propagation and strain rate material characteristics.

5.6 Recommendations for Future Works

Many topics related to dynamic pulse buckling problems are presented herein. Additional research in this area is required to further explore several aspects of the problem, including:

- Multiple wave type interaction (shear, flexural and longitudinal) and their combined influence on dynamic pulse buckling behaviour.
- High strain rate structural response (including spallation) using material EOS.
- Use of solid elements to evaluate through thickness stress propagation characteristics in plated structures.
- Establishment of the limit of structural complexity that can still be considered simple enough to be governed by stress wave propagation characteristics.
- Benchmarking a simple pulse buckling problem analysis using implicit analysis methods to determine appropriate implicit time step size and control parameters.

BIBLIOGRAPHY

[1] Abrahamson, G.R. and Goodier, J. N. 1966. "Dynamic flexural buckling of rods within an axial plastic compressive wave." Journal of Applied Mechanics, 33(2): 241-247.

[2] Abramovich, H., Weller, T. and Yaffe, R. 1989. "Application of a modified donell technique for the determination of critical loads of imperfect plates." Computers and Structures, 37(4): 463-469.

[3] Abramovich, W. and Jones, N. 1997. "Transition from initial global bending to progressive buckling of tubes loaded statically and dynamically." International Journal of Impact Engineering, 19(5-6): 415-437.

[4] Abramovich, H. and Grunwald, A. 1995. "Stability of axially impacted composite plates." Composite Structures, 32: 151-158.

[5] Anghileri, M., Castelletti, L.M.L, and Tirelli, M. 2005. "Fluid-structure interaction of water filled tanks during the impact with the ground." International Journal of Impact Engineering, v 31: 235-254.

[6] Anwen, W. and Tian W. 2007. "Mechanism of buckling development in elastic bars subjected to axial impact." International Journal of Impact Engineering, 34: 232-252.

[7] Anwen, W. and Tian W. 2002. "Twin-characteristic-parameter solution for dynamic buckling of columns under elastic compression wave." International Journal of Solids and Structures, 39: 861-877.

[8] Anwen, W. and Tian, W. 2006. "Development mechanism of local plastic buckling in bars subjected to axial impact." International Journal of Solids and Structures, 43: 4578-4594.

[9] Anwen, W. and Tian, W. 2003. "Characteristic-value analysis for plastic dynamic buckling of columns under elastoplastic compression waves." International Journal of Non-Linear Mechanics, 38: 615-628.

[10] Ari-Gur, J., Weller, T. and Singer, J. 1982. "Experimental and theoretical studies of columns under axial impact." International Journal of Solids Structures, 18(7): 619-641.

[11] Ari-Gur, J. and Simonetta, S.R. 1997. "Dynamic pulse buckling of rectangular composite plates." Composites Part B: Engineering, 28(3): 301-308.

[12] *ASM Handbook.*2000. “Mechanical Testing and Evaluation.” ASM International. Materials Park, Ohio.

[13] Bich, H.D. *et al.*. 2013. “Nonlinear static and dynamic buckling analysis of imperfect eccentrically stiffened functionally graded circular cylindrical thing shells under axial compression.” International Journal of Mechanical Sciences, 74: 190-200.

[14] Bodner, S.R and Symonds, P.S. 1962. “Experimental and theoretical Investigation of the plastic deformation of cantilever beams subjected to impulsive loading.” Journal of Applied Mechanics, 29(4): 719-728.

[15] Budiansky, B. and Hutchinson, J.W. 1964. *Dynamic buckling of imperfection-sensitive structures.* Ft. Belvoir Defense Technical Information Center.

[16] Cheong, H.K., Hoa, H., and Cui, S. 2000. “Experimental investigation of dynamic post-buckling characteristics of rectangular plates under fluid-solid slamming.” Engineering Structures, 22: 947-960.

[17] Cole, R.H.. 1948. *Underwater Explosions*. Princeton University Press. Princeton, New Jersey.

[18] Corona, E., Lee, L.H., and Kyriakides, S. 2006. “Yield anisotropy effects on buckling of circular tubes under bending.” International Journal of Solids and Structures, 43: 7099-7118.

[19] Cowper, G.R. and Symonds, P.S. 1958. “Strain hardening and strain rate effects in the impact loading of cantilever beams.” Brown University, Applied Mathematic Report.

[20] Davidson, J.F. 1953. “Buckling of struts under dynamic loading.” Journal of Mechanics and Physics of Solids, 2: 54-66.

[21] Disimile, P.J, Davis, J. and Toy, N. 2011. “Mitigation of shock waves within a liquid filled tank.” International Journal of Impact Engineering, 38: 61-72.

[22] Ellinas, C.P. and Croll, J.G.A. 1986. “Elastic-plastic buckling design of cylindrical shells subject to combined axial compression and pressure loading.” International Journal of Solids and Structures, 22(9): 1007-1017.

[23] Farshad, Mehdi. 1994. *Stability of Structures*. Elsevier Science B.V. Amsterdam. Developments in Civil Engineering, v 43.

[24] Florence, A.L. and Goodier, J.N. 1968. “Dynamic plastic buckling of cylindrical shells in sustained axial compressive flow.” Journal of Applied Mechanics, 35(1): 80-86.

[25] Fowles, G.R. 1973. “Experimental technique and instrumentation, dynamic response of materials to intense impulse loading, P.C. Chou and A.K. Hopkins, Edition.” Air Force Materials Laboratory, Wright-Patterson Air Force Base.

[26] Graves Smith, T.R. 1972. “The post-buckled behavior of a thin-walled box beam in pure bending.” International Journal of Mechanical Science, 14: 711-722.

[27] Graves Smith, T.R. 1970. “The local buckling of box girders under bending stresses.” International Journal of Mechanical science, 11: 403-412.

[28] Hamdan, F.H. 1999. “Near-field fluid-structure interaction using Lagrangian fluid finite elements.” Journal of Computers and Structures, 71: 123-141.

[29] Hayashi, T. and Sano, Y. 1972. “Dynamic buckling of elastic bars (1st report, the case of low velocity impact).” The Japan Society of Mechanical Engineers, 15(88): 1167-1175.

[30] Hayashi, T. and Sano, Y. 1972. “Dynamic buckling of elastic bars (2nd report, the case of high velocity impact).” The Japan Society of Mechanical Engineers, 15(88): 1176-1184.

[31] Hoo Fatt, M.S. and Pothula, S.G. 2010. “Dynamic pulse buckling of composite shells subject to external blast.” Composite Structures, 92: 1716-1727.

[32] Hutchinson, J.W and Budiansky, B. 1966. “Dynamic buckling estimates.” AIAA Journal, 4(3): 525-530.

[33] Johnson, G.R. and Cook, W.H. 1983. “A constitutive model and data for metals subjected to large strains, high strain rates and high temperatures.” Proceedings of the 7th International Symposium on Ballisitics, The Hague, The Netherlands.

[34] Karagiozova, D. and Jones, N. 2000. “Dynamic elastic–plastic buckling of circular cylindrical shells under axial impact.” International Journal of Solids and Structures, 37: 2005-2034.

[35] Karagiozova, D. and Jones, N. 2001. “Influence of stress waves on the dynamic progressive and dynamic plastic buckling of cylindrical shells.” International Journal of Solids and Structures, 38: 6723-6749.

[36] Karagiozova, D. 2002. “Dynamic buckling of elastic–plastic buckling square tubes under axial impact-I: stress wave propagation phenomenon.” International Journal of Solids and Structures, 30: 143-166.

[37] Karagiozova, D. and Jones, N. 2002. “On dynamic buckling phenomena in axially laded elastic-plastic cylindrical shells.” International Journal of Non-Linear Mechanics, 37: 1223-1238.

[38] Karagiozova, D. and Alves, M. 2004. “Transition from progressive buckling to global bending of circular shells under axial impact – Part I: Experimental and numerical observations.” International Journal of Solids and Structures, 41: 1565-1580.

[39] Karagiozova, D. and Alves, M. 2004. “Transition from progressive buckling to global bending of circular shells under axial impact – Part II: Theoretical analysis.” International Journal of Solids and Structures, 41: 1581-1604.

[40] Karagiozova, D. and Jones, N. 2008. “On the mechanics of the global bending collapse of circular tubes under dynamic axial load – Dynamic buckling transition.” International Journal of Impact Engineering, 35: 397-424.

[41] Kenny, S., Pegg, N. and Taheri, F. 2000. “Dynamic elastic buckling of a slender beam with geometric imperfections subject to an axial impulse.” Finite Elements in Analysis and Design, 35: 227-246.

[42] Kolsky, H. 1949. “An investigation of the mechanical properties of materials at very high rates of loading”. Proceedings of the Physical Society, 62:375-457.

[43] Koning, C. and Taub, J. 1933. “Impact buckling of thin bars in the elastic range Hinged at both ends.” National Advisory Committee for Aeronautics. Report No. 748.

[44] Kotelko, M. and Mania, R.J. 2012. “Quasi-static and dynamic axial crushing of TWCF open-section members.” Thin Walled Structures, 61: 115-120.

[45] Kounadis, A.N., Gantes, C., and Simitses, G. 1997. “Nonlinear dynamic buckling of multi-DOF structural dissipative systems under impact loading.” International Journal of Impact Engineering, 19(1): 63-80.

[46] Kubiak, Tomasz. 2013. *Static and Dynamic Buckling of Thin-Walled Plate Structures.* Springer International Publishing. Switzerland.

[47] Lepik, Ulo. 2001. “Dynamic buckling of elastic-plastic beams including effects of axial stress waves.” International Journal of Impact Engineering, 25: 537-552.

[48] Less, H. and Abramovich, H. 2012. “Dynamic buckling of a laminated composite stringer-stiffened cylindrical panel.” Composites Part B: Engineering, 43: 2348-2358.

[49] Lindberg, H.E. and Florence, A.L. 1987. *Dynamic Pulse Buckling – Theory and Experiment*. Martinus Nijhoff Publishers. Dordrecht.

[50] Lindholm, U.S. and Chan, K.S. 1986. *Constitutive Modeling for Isotropic Materials*. Southwest Research Institute. NASA Scientific and Technical Information Branch. CR 182132.

[51] Lloyd's Register. 2014. *Rules and Regulations for the Classification of Naval Ships*.

[52] Livermore Software Technology Corporation. LS-Dyna User Manual. 2012. Version 971 R6.1.0.

[53] Lu, G.Y., Han, Z.J., Lei, J.P., and Zhang, S.Y. 2009. "A study on the impact response of liquid-filled cylindrical shells." Thin-Walled Structures, 47: 1557-1566.

[54] Manevich, A. and Kolakowski, Z. 1996. "Influence of local postbuckling behanvilur on bending of thin-walled beams." Thin-Walled Structures, 25(3): 219-230.

[55] Mania, R.J. 2011. "Dynamic buckling of thin-walled viscoplastic columns." Thin-Walled Structures, 49: 581-588.

[56] Marsh, S.P. 1980. *LASL Shock Hugoniot Data*. University of California Press. London, England.

[57] Meyers, M.A. 1994. *Dynamic Behavior of Materials*. John Wiley & Sons. New York, New York.

[58] Michel, G., Limam, A and Jullien J.F. 2000. "Buckling of cylindrical shells under static and dynamic shear loading." Engineering Structures, 22: 535-543.

[59] Mittal, V., Chakraborty, T., and Matsagar, V. 2014. "Dynamic analysis of liquid storage tank under blast using coupled Euler-Lagrangian formulation." Journal of Thin-Walled Structures, 84: 91-111.

[60] Mittelstedt, C. 2009. "Explicit local buckling analysis of stiffened composite plates accounting for periodic boundary conditions and stiffener-plate interaction." Composite Structures, 91: 249-265.

[61] Murase, K. and Jones, N. 1993. *The variation of modes in the dynamic axial plastic buckling of circular tubes*. Plasticity and Impact Mechanics. Wiley Eastern Limited.

[62] Patel, S.N., Datta, P.K., and Sheikh, A.H. 2007. “Dynamic instability analysis of stiffened shell panels subjected to partial edge loading along the edges.” International Journal of Mechanical Sciences, 49: 1309-1324.

[63] Patel, S.N., Datta, P.K., and Sheikh, A.H. 2006. “Buckling and dynamic instability analysis of stiffened shell panels.” Thin-Walled Structures, 44: 321-333.

[64] Pevzner, P., Abramovich, H. and Weller, T. 2008. “Calculation of the collapse load of an axially compressed laminated composite stringer-stiffened curved panel-An engineering approach.” Composite Structures, 83: 341-353.

[65] Pedron, C. and Combescure, A. 1995. “Dynamic buckling of stiffened cylindrical shells of revolution under a transient lateral pressure shock wave.” Thin-Walled Structures, 23: 85-105.

[66] Petry, D. and Falbusch G. “Dynamic buckling of thin isotropic plates subjected to in-plane impact”. Thin Walled Structures, 38(3): 267-283.

[67] Putelat, T. and Triantafyllidis, N. 2013. “Dynamic stability of externally pressurized elastic rings subjected to high rates of loading.” International Journal of Solids and Structures, 51(1): 1-12.

[68] Ramesh, K.T. 2008. “High Strain Rate and Impact Experiments.” Springer Handbook of Experimental Solid Mechanics, D: 929-960.

[69] Rankine, W.J. 1870. “On the thermodynamic theory of waves of finite longitudinal disturbance.” Philosophical Transactions of the Royal Society of London, 160: 277-288.

[70] Ravinger, J. 1992. “Dynamic post-buckling behaviour of plate girders.” Journal of Construction Steel Research, 21: 175-194.

[71] Rees, D. 2006. *Basic Engineering Plasticity: An Introduction with Engineering and Manufacturing Applications.* Elsevier Limited. Burlington, MA.

[72] Rusinek, A., R. Zaera and J.R. Klepaczko. 2007. “Constitutive relations in 3-D for a wide range of strain rates and temperatures – Application to mild steels.” International Journal of Solids and Structures, 44: 5611-5634.

[73] Sofiyev, A.H. and Aksogan, O. 2004. “Buckling of a conical thing shell with variable thickness under a dynamic loading.” Journal of Sound and Vibration, 270: 903-915.

[74] Sosa, E.M., Godoy, L.A., and Croll, J.G.A. 2005. “Computation of lower-bound elastic buckling loads using general-purpose finite element codes.” Computers and Structures, 84: 1934-1945.

[75] Sridharan, S. and Zeggane, M. 2001. “Stiffened plates and cylindrical shells under interactive buckling.” Finite Elements in Analysis and Design, 38: 155-178.

[76] Su, X.Y, Yu, T.X. and Reid, T.S. 1995. “Inertia-sensitive impact energy-absorbing structures part I: Effects of inertia and elasticity”. International Journal of Impact Engineering, 16: 651-672.

[77] Su, X.Y, Yu, T.X. and Reid, T.S. 1995. “Inertia-sensitive impact energy-absorbing structures part II: Effects Strain rate.” International Journal of Impact Engineering, 16: 651-672.

[78] Tam, L.L., and Calladine, C.R. 1991. “Inertia and strain-rate effects in a simple plate-structure under impact loading.” International Journal of Impact Engineering, 11: 349-377.

[79] Taylor, G.I. 1948. “The use of flat-ended projectiles for determining dynamic yield strength, part I: theoretic considerations.” Proceedings of the Royal Society of London A: Mathematical, Physical and Engineering Sciences, 194: 289-299.

[80] Wah, T. 1970. “Dynamic buckling of thin circular rings.” International Journal of Mechanical Science, 12: 143-155.

[81] Webb, D.C, Kormi, K. and Al-Hassani, S.T.S. 2001. “The influence of inertia and strain-rate on large deformation of plate-structures under impact loading.” Computers and Structures, 79: 1781-1797.

[82] Wei, Z.G. and Batra, R.C. 2006. “Dynamic buckling of thin thermoviscoplastic cylindrical shell under radial impulsive loading.” Thin-Walled Structures, 44: 1109-1117.

[83] Wei, Z.G., Yu, J.L. and Batra, R.C. 2005. “Dynamic buckling of thin cylindrical shells under axial impact.” International Journal of Impact Engineering, 32: 575-592.

[84] Weller, T., Abramovich, H. and Yaffe, R. 1989. “Dynamic buckling of beams and plates subjected to axial impact.” Computers and Structures, 32(3/4): 835-851.

[85] Xu, X., Ma, J., Lim, C.W., and Chu, H. 2009. “Dynamic local and global buckling of cylindrical shells under axial impact.” Engineering Structures, 31: 1132-1140.

[86] Yaffe, R. and Abramovich, H. 2003. “Dynamic buckling of cylindrical stringer stiffened shells.” Computers and Structures, 81: 1031-1039.